Alma Mater Studiorum – Università di Bologna

School of Science
Department of Physics and Astronomy
Master Degree Programme in Astrophysics and Cosmology

Testing a specific implementation of the Alcock-Paczyński test on the Magneticum simulations

Graduation Thesis

Presented by:
Giuseppe Nazareno Di Gesu

Supervisor:
Chiar.mo Prof. Federico Marulli

Academic year 2023-2024
Graduation date I

Abstract

In cosmology, accurately determining the parameters of a given model is essential for properly inferring the evolution of the universe and explaining its observable characteristics. The ΛCDM (Λ-cold dark matter) model, widely considered in cosmology, predicts the existence of three fundamental components: matter (comprising both dark and baryonic matter), radiation, and the cosmological constant (Λ). Each of these components contributes to the total density of the universe. To quantify these contributions, we usually use density parameters.

In this thesis, our aim has been to test the efficiency of a particular method for determining the matter density parameter, called the Alcock-Paczyński (AP) test. We took advantage of the geometric anisotropies inherent in the two-point correlation function of different simulated cosmic tracers, which emerged from the assumption of a wrong cosmology when calculating the comoving distances. We employed a particular method to conduct the AP test while modeling the anisotropic distortions involving a Boltzmann solver.

Contents

Introduction

Modern cosmology, which is the study of the largest degrees of freedom of the universe, began with a remarkable paper published by Albert Einstein in 1917 [24]. From its formulation up until today, cosmology has undergone a rapid evolution, culminating in the development of the so-called standard cosmological model, which is supported by the main observational evidence available today [7][37].

In the context of this model, we know that the universe has three main components: matter, radiation, and the cosmological constant. These components, particularly their densities, are associated with the so-called cosmological parameters. Only through a precise determination of these parameters is it possible to understand the global evolution of the universe and explain its characteristics, such as its expansion and large-scale structure.

In this thesis work, we studied the efficiency of a particular method for estimating the matter density parameter, Ω_M, known as the Alcock-Paczyński (AP) test [9]. This method was initially tested with the correlation function measured on simulated catalogues of galaxies, active galactic nuclei (AGN), and galaxy clusters, provided by a large hydrodynamic cosmological simulation, called *Magneticum* [22]. The method is based on the assumption of homogeneity and isotropy of the universe on large scales, i.e. the cosmological principle. We searched for the so-called geometric distortions in the two-point correlation function, which measures the excess or deficit probability of finding two objects separated by a certain comoving distance compared to a random distribution. For this type of analysis, it is convenient to decompose the distances into perpendicular and parallel components to the line of sight; thus, we measured a bidimensional correlation function. In the case of perfect isotropy, the iso-correlation curve of the bidimensional function should have a circular form. However, assuming an incorrect cosmological model deforms the distances differently along the two directions, introducing geometric distortions. In real observations, the bidimensional correlation function is also affected by dynamic distortions due to the peculiar velocities of objects, which are not accounted for in distance measurements. By modeling these distortions,

it is possible to obtain constraints on the dynamics and geometry of the Universe. The main advantage of this method is the fact that it is only dependent on the assumption of isotropy of the correlation function. This assumption is directly linked to the cosmological principle, which underlies all the equation systems of modern cosmology.

In this thesis work, we applied the AP test to different catalogues extracted from the *Magneticum* simulation, using the same method utilized in [44]. We studied how the method's efficiency in discriminating the correct value of Ω_M depends on the type of tracer used, the redshift of the observation, and the modelling of dynamic distortions.

In the first chapter, the main notions of the standard cosmological model will be introduced to describe the dynamics of the universe and its characterizing parameters. The second chapter will briefly discuss the theory that explains the origin and subsequent evolution of cosmic structures. It will also introduce the concept of clustering, which describes the spatial properties of structures due to gravitational interaction. From there, we will transition to the definition of the two-point correlation function. The third chapter will be dedicated to introducing the vast theme of numerical simulations. It will also describe the principal characteristics of the catalogs utilized and the *Magneticum* simulation. In the fourth chapter, the different types of distortions that can modify the form of the bidimensional correlation function will be discussed. Then, the procedures leading to the AP test will be shown, with a focus on two approaches to performing the method. In the fifth chapter, it will be shown in detail how the AP test has been implemented numerically to analyze the catalogues described in the third chapter. In the sixth chapter, the results of our analysis will be shown. The final chapter will discuss the main results and present future perspectives regarding the method used.

Chapter 1

From the FLRW metric to the Friedmann models

The scope of this chapter is to provide a general overview of cosmology, a physical theory that was long considered a philosophical speculation. The object of cosmology is the study of the universe as a whole. It deals with describing the origin and evolution of the universe, focusing on the analysis of cosmic structures. We will describe the properties, laws, and important phenomena inherent to a four-dimensional universe, with a special focus on the parameters that define a cosmological model.
For the demonstrations and the calculus of the main results we refer to the textbook *Gravitation and Cosmology: Principles and Applications of the General Theory of Relativity* of Steven Weinberg [58].

1.1 Principles of cosmology

In physics, it is common to introduce principles to understand certain observables. These principles often leverage symmetry to simplify the analysis by reducing the number of degrees of freedom to be considered. Cosmology is no exception, and its first principle is the so-called

Cosmological principle (CP): "In the Universe, there are no preferred positions or directions. The Universe, on large scales, is to be considered homogeneous and isotropic".

Einstein introduced this principle to establish a relativistic theoretical foun-

dation for cosmology. The CP may also be taken as a working assumption upon which explicit models of the universe are built and verified *a posteriori*.

1.1.1 Friedman-Lemaître-Robertson-Walker metric

The first step towards constructing a cosmological model involves establishing a metric for the Universe to measure distances between two distinct points in space-time (events). The objective is to utilize the most general metric that embodies the CP. The distance ds between two points is described by:

$$ds^2 = g_{\alpha\beta}dx^\alpha dx^\beta = g_{00}dt^2 + 2g_{0i}dx^i dt + g_{ij}dx^i dx^j \quad , \tag{1.1}$$

where the first term represents the time part, the second the mixed term, and the third the spatial part. The metric is defined by the components of $g_{\alpha\beta}$ of the corresponding metric tensor that describes the geometry of space-time. If space is to be homogeneous and isotropic according to the CP, it must be possible to define a proper time such that, the three-dimensional metric can be expressed as:

$$dl^2 = g_{ij}dx^i dx^j \quad , \tag{1.2}$$

at every point in time. In a scenario where there are no preferred positions or directions, the mixed terms should be null, implying that the components g_{0i} of the metric must be zeros. Consequently, the general form of the metric will be:

$$ds^2 = -dt^2 + g_{ij}dx^i dxj = -dt^2 + dl^2 \quad . \tag{1.3}$$

Now we want a general form for the spatial term dl^2, which does not necessarily represent only a flat space. The conventional sphere, also called the 2-sphere, is a homogeneous and isotropic 2d space with finite volume and no boundaries. The analogous for the 3d space is called 3-sphere, from its equation one can obtain the correspondent expression for dl:

$$\textit{Unit 3-sphere: } dl^2 = \frac{dr^2}{1-r^2} + r^2(d\theta^2 + \sin^2\theta d\phi^2) \quad , \tag{1.4}$$

where $r \in [0, 1]$. The metric of a larger sphere is simply obtained by multiplying

the components of the metric tensor by a positive constant a^2. That is

$$\textit{3-sphere: } dl^2 = a^2 \left[\frac{dr^2}{1-r^2} + r^2(d\theta^2 + \sin^2\theta d\phi^2) \right] \quad . \tag{1.5}$$

The quantity a is called the radius.

One way to visualize the conventional 2-sphere is by drawing two equal discs (the northern and southern hemispheres) glued by their common boundary (the equator: a circle). Similarly, one way to visualize a 3-sphere is to imagine two equal balls (the northern and southern hemispheres) glued by their common boundary (the equator: a 2-sphere), Figure 1.1. The 3-sphere is a homogeneous isotropic space with constant *positive* curvature. A homogeneous isotropic space with *zero* curvature is, of course, Euclidean space. There is also a homogeneous isotropic space with constant *negative* curvature: a three-dimensional hyperboloid. Repeating similar steps as above gives:

$$\textit{3-hyperboloid: } dl^2 = a^2 \left[\frac{dr^2}{1+r^2} + r^2(d\theta^2 + \sin^2\theta d\phi^2) \right] \quad . \tag{1.6}$$

The metric

$$\textit{3d homogeneous space: } dl^2 = a^2 \left[\frac{dr^2}{1-kr^2} + r^2(d\theta^2 + \sin^2\theta d\phi^2) \right] \quad . \tag{1.7}$$

where k can take the value 1 (sphere), -1 (hyperboloid), or 0 (Euclidean space), can be shown to be the most general homogeneous isotropic 3d metric. Knowing this we can now define a metric that embodies the CP, the FLRW (Friedman-Lemaître-Robertson-Walker):

$$ds^2 = -dt^2 + a(t)^2 \left[\frac{dr^2}{1-kr^2} + r^2(d\theta^2 + \sin^2\theta d\phi^2) \right] \equiv -dt^2 + a(t)^2 d\sigma^2 \quad , \tag{1.8}$$

where the origin $r = 0$ is totally arbitrary, t is the proper time of so-called comoving observer moving along with the homogeneous and isotropic cosmic fluid (the idealized representation of galaxies) at constant r, θ, and ϕ. We shall also call

$$\begin{aligned} \{t, r, \theta, \phi\} &\quad \text{comoving coordinates} \\ a(t) &\quad \text{(cosmic) scale factor} \\ k = 0, \pm 1 &\quad \text{curvature constant.} \end{aligned} \tag{1.9}$$

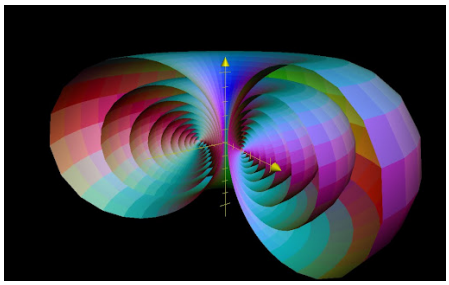

Figure 1.1: A 3-sphere is obtained by gluing two balls by the boundary (a 2-sphere).

Observations indicate that the distance between galaxies increases over time, while their typical size remains constant. This suggests that the Universe is expanding, with distant galaxies moving away from us at increasing speeds. Using the differential geometric language, the universe can be seen as four-dimensional manifold whose three-manifold spatial foliation (submanifold family) is homogeneous and isotropy. Localized sources predominantly influence local lengths whereas the distance between sources increases due to the expanding scale factor.

1.1.2 The Hubble-Lemaître law

In cosmology, it is necessary to define another kind of distance besides the proper distance: the comoving distance. Let us consider two objects aligned along the line of sight of the observer, such that $d\theta = d\Phi = 0$. The physical spatial distance between the two, considering the spatial hypersurface with $dt = 0$, is called proper distance $d_{pr}(t)$ and it is given by

$$d_{pr} = \int_0^r \frac{a(t)dr'}{\sqrt{1 - kr'^2}} \quad , \tag{1.10}$$

where t is the time measured by comoving clocks. Since a is not proportional to r we can write

$$d_{pr} = a(t)F(r) \quad , \tag{1.11}$$

where $F(r)$ is a function of the radius that describes the spatial part of the FLRW metric and it assumes different values for the different values of k. As one can see d_{pr} is a quantity that depends also on time. It is defined comoving distance the d_{pr} computed at t_0 ($t_0 \equiv 0$)

$$d_C = d_{pr}(t_0) = a(t_0)F(r) = a_0F(r) \quad , \tag{1.12}$$

where we usually put by definition $a_0 = 1$. The relation between proper distance and comoving distance is given by

$$d_{pr} = d_C \frac{a(t)}{a_0} \quad . \tag{1.13}$$

Now we can derivate the Eq. 1.11 as a function of time to find the radial velocity at a given point:

$$v_R = \frac{d(d_{pr})}{dt} = \frac{d}{dt}[a(t)F(r)] = \frac{da(t)}{dt}F(r) + a(t)\frac{dF(r)}{dt} = \dot{a}(t)F(r) + a(t)\dot{F}(r) \quad . \tag{1.14}$$

But since $\dot{F} := \frac{dF}{dt} = 0$ and $F(r) = d_{pr}/a(t)$ we have

$$v_R = \frac{\dot{a}(t)}{a(t)} d_{pr} = H(t) d_{pr} \quad . \tag{1.15}$$

This equation is the famous Hubble-Lemaître law where we have defined the Hubble constant:

$$H(t) = \frac{\dot{a}(t)}{a(t)} \quad , \tag{1.16}$$

even if it would be better to call it the Hubble parameter since it depends on time.

1.1.3 Cosmological redshift

The cosmological redshift, z, is defined as follows:

$$z := \frac{\lambda_{obs} - \lambda_{em}}{\lambda_{em}} = \frac{\Delta\lambda}{\lambda} \quad , \tag{1.17}$$

which measures the shift of the emitted spectrum, at the wavelength λ_{em} and at time t_{em}, for a source that moves at a velocity v_R from the observer which sees λ_{obs} at time t_{obs}.

Let us consider the FLRW metric in polar coordinates (1.8) with $d\phi = d\theta = 0$:

$$ds^2 = -dt^2 + a(t)^2 \frac{dr^2}{1 - kr^2} \quad , \tag{1.18}$$

and consider a photon, for which $ds^2 = 0$. Then we can write:

$$\frac{dt^2}{a(t)^2} = \frac{dr^2}{1 - kr^2} \quad , \tag{1.19}$$

and then integrating the square:

$$\int_{t_{em}}^{t_0} \frac{dt}{a(t)} = \int_0^r \frac{dr}{\sqrt{1-kr^2}} := F(r) \quad . \tag{1.20}$$

If from the same source, a second photon is emitted after a time δt_{em}, it will be received by the observer at time $t_0 + \delta t_0$. If the space traveled from the two photons is equal, we have the following:

$$\int_{t_{em}}^{t_0} \frac{dt}{a(t)} = F(r) = \int_{t_{em}+\delta t_{em}}^{t_0+\delta t_0} \frac{dt}{a(t)} \quad , \tag{1.21}$$

and integrating

$$\frac{t_0}{a_0} - \frac{t_e}{a(t)} = \frac{t_0}{a_0} + \frac{\delta t_0}{a_0} - \frac{t_e}{a(t)} - \frac{\delta t_e}{a(t)} \quad , \tag{1.22}$$

$$\frac{\delta t_0}{a_0} = \frac{\delta t_e}{a(t)} \Rightarrow \frac{1}{a_0 \nu_0} = \frac{1}{a(t)\nu_e} \quad , \tag{1.23}$$

where ν_0 and ν_e are the observed and the emitted frequencies. We can therefore obtain:

$$a_0\nu_0 = a(t)\nu_e \Rightarrow \frac{a_0}{\lambda_0} = \frac{a(t)}{\lambda_e} \Rightarrow \frac{\lambda_0}{\lambda_e} = \frac{a_0}{a(t)} \quad , \tag{1.24}$$

so λ_0 is a measure of how much the scale factor changes from its emission until its observation. We have that z is an increasing function going back in time

$$1 + z = \frac{a_0}{a(t)} \quad . \tag{1.25}$$

1.1.4 Friedmann equations

Once we have established the FLRW metric, which describes the four-dimensional geometry of the universe, it is possible to study how the universe evolves on large scales over time and identify the factors that can influence its evolution.

As the base for all relativistic cosmological models, we have the system given by the Einstein equations (with $c = 1$):

$$R_{\mu\nu} - \frac{1}{2} g_{\mu\nu} R = 8\pi G T_{\mu\nu} \quad , \tag{1.26}$$

where $R_{\mu\nu}$ [1] is il Ricci tensor and R the Ricci scalar. This equation states that the geometry of spacetime of the Universe, expressed by the tensor metric $g_{\mu\nu}$, is given by its energetic content, represented by the energy-momentum tensor $T_{\mu\nu}$. On one side we have the spatial part of the equation and on the other the energy part. Once we assume $T_{\mu\nu}$, we can derive $g_{\mu\nu}$. Since in our case we know the form of $T_{\mu\nu}$, we can find the scale factor $a(t)$ and its derivatives. In the Friedmann models, we assume the FLWR metric, from which one can find $R_{\mu\nu}$ e R , and for the energy-momentum tensor we assume the universe is filled with a perfect fluid of matter and energy described by:

$$T_{\mu\nu} = -pg_{\mu\nu} + (p+\rho)\, U_\mu U_\nu \quad , \tag{1.27}$$

where the p is the pressure, ρ the energy density, and U_k the four-velocity.

The system of equations provides 16 equations of which only two are independent (assuming CP), the components with the same index are the following:

$$G_{00} = 8\pi G_{\rm N} T_{00} \quad \Rightarrow \quad 3\left[\left(\frac{\dot{a}}{a}\right)^2 + \frac{k}{a^2}\right] = 8\pi G_{\rm N}\rho \quad , \tag{1.28}$$

$$G_{ii} = 8\pi G_{\rm N} T_{ii} \quad \Rightarrow \quad 3\frac{\ddot{a}}{a} = -4\pi G_{\rm N}(\rho + 3p) \quad . \tag{1.29}$$

The Eqs. (1.28) and (1.29) are called the first and the second Friedmann equations. In the second equation both the pressure and the density are present, while in the first the density and the curvature parameter.

It is interesting to compare the second Friedmann equation (1.29) with what would be predicted by Newtonian gravity. Consider a point-like particle of mass m located on the surface of a sphere with homogeneous density ρ and radius $R = ra$. The radial Newtonian acceleration experienced by this particle would be

$$\ddot{R} = r\ddot{a} = -\frac{G_{\rm N}(4\pi\rho/3)R^3}{R^2} = -\frac{4}{3}\pi G_{\rm N}\rho r a \quad , \tag{1.30}$$

or

$$3\frac{\ddot{a}}{a} = -4\pi G_{\rm N}\rho \quad , \tag{1.31}$$

[1] The indexes μ and ν go from 0 to 3 while the indexes i and j go from 1 to 3.

which coincides with Eq. (1.29) only for $p = 0$. In other words, the pressure does not gravitate according to Newtonian theory but does so according to Einstein's theory.

1.1.5 The cosmological constant

The Friedmann equations stem from the combination of general relativity, the CP, and the assumption of matter distribution resembling a perfect gas. If we look at the second Friedmann equation (1.29), it is clear that a static universe, i.e. with $\ddot{a} = \dot{a} = 0$, could exist only with

$$\rho = -3p \quad . \tag{1.32}$$

When Einstein developed the theory of general relativity, he obtained the Eq. (1.26). However, given the above consideration, he proposed a modification. The introduction of a constant Λ called the cosmological constant, was able to solve the issue of the negative density or pressure

$$R_{\mu\nu} - \frac{1}{2} g_{\mu\nu} R - \Lambda g_{\mu\nu} = 8\pi G T_{\mu\nu} \quad . \tag{1.33}$$

Einstein's problem was the idea of an expanding Universe (this was before the effective discovery by Hubble); he believed that the Universe should be static, and for this reason, he changed his equation.

Although we have advanced beyond Einstein's original ideas, let us develop the Eq. (1.33) to explore the effects of Λ. Specifically, we can define:

- the effective pressure

$$\tilde{p} := p - \frac{\Lambda}{8\pi G} = p + p_\Lambda \quad , \tag{1.34}$$

  where it is added a negative contribution to the pressure that depends on the cosmological constant ($p_\Lambda < 0$);

- the effective density

$$\tilde{\rho} := \rho + \frac{\Lambda}{8\pi G} = \rho + \rho_\Lambda \quad , \tag{1.35}$$

  where it is added the same negative contribution to the density.

From these two relations, one can see that $|\Lambda|^{-1/2}$ has the dimension of a length. Now we can rewrite the Eq. (1.33) as follow:

$$R_{\mu\nu} - \frac{1}{2}g_{\mu\nu}R - \Lambda g_{\mu\nu} = 8\pi G\tilde{T}_{\mu\nu} \quad , \tag{1.36}$$

where we have defined:

$$\tilde{T}_{\mu\nu} := T_{\mu\nu} + \frac{\Lambda}{8\pi G}g_{\mu\nu} = -\tilde{p}g_{\mu\nu} + (\tilde{p} + \tilde{\rho})\, U_\mu U_\nu \quad . \tag{1.37}$$

In this form, the Friedmann equations are identical at the case without the cosmological constant, but now they depend on $\tilde{p}$ e $\tilde{\rho}$. These equations have a static solution for

$$\tilde{\rho} = -3\tilde{p} = \frac{3k}{8\pi G a^2} \quad . \tag{1.38}$$

If we assume a Universe with only "dust", that is a Universe in which the matter pressure is equal to zero ($p = 0$), because it is negligible with respect to the radiation pressure, we have

$$\tilde{p} = -\frac{\Lambda}{8\pi G} \quad . \tag{1.39}$$

Now, from Eq.(1.38), we have

$$\tilde{p} = -\frac{k}{8\pi G a^2} \quad , \tag{1.40}$$

from which

$$\tilde{p} = -\frac{k}{8\pi G a^2} = -\frac{\Lambda c^4}{8\pi G} \quad . \tag{1.41}$$

Therefore in Einstein's static Universe:

$$\Lambda = \frac{k}{a^2} \quad , \tag{1.42}$$

from which the density of a perfect fluid is

$$\rho = \tilde{\rho} - \frac{\Lambda}{8\pi G} = \frac{3k}{8\pi G a^2} - \frac{k8}{\pi G a^2} \quad , \tag{1.43}$$

$$\rho = \frac{k}{4\pi G a^2} \quad . \tag{1.44}$$

Since we have $\rho > 0$ always, Eq. (1.44) has to be greater than zero, and that forces us to set $k = 1$. From these considerations, the Universe appears to be spherical. Replacing Eq.(1.42) into (1.44), we find that in Einstein's Universe the value of the cosmological constant is:

$$\Lambda_E = 4\pi G\rho \quad . \tag{1.45}$$

Einstein's Universe is therefore spherical and it is maintained static (but unstable) from a value of the cosmological constant that depends on the matter density. It has a positive curvature and a curvature radius $a_E = \Lambda_E^{-1/2}$.

When Hubble discovered that the Universe was expanding, Einstein believed of had made a big mistake and decided to remove Λ from his equations. But history has shown that the introduction of the cosmological constant is necessary and today it is utilized to formalize the energy of the vacuum [51].
Now let us consider a particular cosmological model based on the cosmological constant, known as the de Sitter model. In this model, the Universe is characterized by being empty ($p = \rho = 0$) and flat ($k = 0$). Thus:

$$\rho = \tilde{\rho} - \frac{\Lambda}{8\pi G} = \frac{3k}{8\pi G a^2} - \frac{k8}{\pi G a^2} \quad . \tag{1.46}$$

Substituting these quantities into the first Friedmann equation for Einstein Universes, we have the following:

$$\dot{a}^2 + k = \frac{8\pi G}{3}\tilde{\rho} a^2 \quad , \tag{1.47}$$

from which

$$\dot{a}^2 = \frac{8\pi G}{3}\frac{\Lambda}{8\pi G}a^2 = \frac{\Lambda}{3}a^2 \quad , \tag{1.48}$$

and then

$$\frac{\mathrm{d}a}{\mathrm{d}t} = a\sqrt{\frac{\Lambda}{3}} \Rightarrow \frac{\mathrm{d}a}{a} = \sqrt{\frac{\Lambda}{3}}\,\mathrm{d}t \quad , \tag{1.49}$$

$$\log a = \sqrt{\frac{\Lambda}{3}}t + A \quad , \tag{1.50}$$

$$a = A \exp\left(\sqrt{\frac{\Lambda}{3}} t\right) \quad . \tag{1.51}$$

The expansion in the de Sitter model is exponential. We thus have the following expression for the Hubble parameter

$$H = \frac{\dot{a}}{a} = \frac{A \exp\left(\sqrt{\frac{\Lambda}{3}} t\right) \sqrt{\frac{\Lambda}{3}}}{A \exp\left(\sqrt{\frac{\Lambda}{3}} t\right)} \Rightarrow H = \sqrt{\frac{\Lambda}{3}} \quad . \tag{1.52}$$

This equation depends only on constants, making it evident that the Hubble parameter in a de Sitter Universe is indeed constant.

This model is also used in the context of the inflationary model, where the expansion is exponential.

1.2 Friedmann models

Now we present the standard cosmological model on which this thesis works. This model is obtained by solving the Friedmann equations. The Belgian priest Georges Lemaître essentially obtained the same results in 1927 [40], when Hubble's discoveries were becoming known to the scientific community. Lemaître is often considered the father of the modern Big Bang theory, although this honor probably should belong to Friedmann.

Firstly, let us consider a perfect fluid with a certain density, ρ, and a certain pressure, p. For now, we do not worry about the specific form of the equation of state relating these two quantities, and we will initially disregard the cosmological constant. We need to solve the Friedmann equations, which we list here for convenience along with the adiabatic condition:

$$\dot{a}^2 + k = \frac{8\pi}{3} G \rho a^2 \quad , \tag{1.53}$$

$$\ddot{a} = -\frac{4\pi}{3} G \left(\rho + 3p\right) a \quad , \tag{1.54}$$

$$d\left(\rho a^3\right) = -3pa^2 da \quad . \tag{1.55}$$

These equations enable us to compute the temporal evolution of $a(t)$, $\rho(t)$ and $p(t)$ if the state equation of the fluid is known.

Now let us consider a specific moment in time t_0, which corresponds to "today". In this case $H_0 = \dot{a}_0$. We can also define

$$\rho_{crit} := \frac{3H^2}{8\pi G} \quad , \tag{1.56}$$

that we will call critical density; at t_0 it will be

$$\rho_{crit,0} := \frac{3H_0^2}{8\pi G} \quad . \tag{1.57}$$

If we now take Eq. (1.53) evaluated today and rewrite it as

$$\dot{a}_0^2 = -k + \frac{8\pi G}{3}\rho_0 \frac{H_0^2}{H_0^2} =$$

$$= \dot{a}_0^2 = -k + \rho_0 \dot{a}_0^2 \frac{H_0^2}{\rho_{crit,0}}, \tag{1.58}$$

we obtain

$$H_0^2 \left(1 - \frac{\rho_0}{\rho_{crit,0}}\right) = -\frac{k}{a_0^2} \quad . \tag{1.59}$$

For different values of k we will have

- for $k = -1 \Rightarrow 1 - \frac{\rho_0}{\rho_{crit,0}} > 0 \Rightarrow \rho_0 < \rho_{crit,0}$;
- for $k = 0 \quad \Rightarrow \quad 1 - \frac{\rho_0}{\rho_{crit,0}} = 0 \quad \Rightarrow \quad \rho_0 = \rho_{crit,0}$;
- for $k = +1 \quad \Rightarrow \quad 1 - \frac{\rho_0}{\rho_{crit,0}} < 0 \quad \Rightarrow \quad \rho_0 > \rho_{crit,0}$.

Now we introduce the so-called density parameter:

$$\Omega := \frac{\rho}{\rho_{crit}} \quad , \tag{1.60}$$

and, obviously, $\Omega_0 := \frac{\rho_0}{\rho_{crit,0}}$. So the above relations became:

- $k = -1 \quad \Rightarrow \quad \Omega_0 < 1$ (hyperbolic universe);
- $k = 0 \quad \Rightarrow \quad \Omega_0 < 1$ (flat universe);
- $k = +1 \quad \Rightarrow \quad \Omega_0 < 1$ (hyperspherical universe).

To determine Ω_0, we need to know $\rho_{crit,0}$ and therefore H_0. The value of H_0 is generally provided, through the inclusion of a dimensionless parameter h, in the following way:

$$H_0 = h \cdot 100 \text{ km s}^{-1}\text{Mpc}^{-1} \quad . \tag{1.61}$$

In the current state of the art, the measured value of H_0 is $\sim 70\text{kms}^{-1}\text{Mpc}^{-1}$, but it is affected by a certain tension ($\sim 4\sigma$) between the value inferred from the cosmic microwave background (CMB) analysis and the one measured in the local Universe [57][19].

Recalling the definition of the critical density, we can obtain its value today, which depends on the type of Universe we live in through the dimensionless constant h:

$$\rho_{\text{crit},0} = 1.9 \times 10^{-29} h^2 \text{ g/cm}^3[17] \quad . \tag{1.62}$$

Therefore, to understand the geometry of the Universe, we need to know its density today. Now let us see what happens if we reintroduce the cosmological constant. In Section 1.42, we saw that Λ can be treated as a fluid with a peculiar equation of state, leading to a modification of Einstein's gravity equation. The Friedmann equations (1.54) and (1.53) will thus require an additional term. We start with the second Friedmann equation (1.54), with the terms ρ and p replaced by $\tilde{p}$ and $\tilde{\rho}$, which becomes:

$$\ddot{a} = -\frac{4\pi G}{3} a \left[\rho + \frac{\Lambda}{8\pi G} + 3\left(p - \frac{\Lambda}{8\pi G}\right)\right] = -\frac{4\pi G}{3} a \left(\rho + 3p - \frac{2\Lambda}{8\pi G}\right) \quad , \tag{1.63}$$

that we can rewrite as

$$\ddot{a} = -\frac{4\pi G}{3} a \left(\rho + 3p\right) + \frac{\Lambda a}{3} \quad . \tag{1.64}$$

The first Friedmann equation also includes an additional term:

$$\dot{a}^2 + k = \frac{8\pi G}{3} a^2 \left(\rho + \frac{\Lambda}{8\pi G}\right) = \frac{8\pi G}{3} \rho a^2 + \frac{\Lambda a^2}{3} \quad , \tag{1.65}$$

that can be rewritten as follows:

$$\dot{a}^2 - \frac{\Lambda a^2}{3} - \frac{8\pi G}{3} \rho a^2 = -k \quad . \tag{1.66}$$

If we compute the last expression at t_0, remembering the definitions $H_0 = (\dot{a}_0/a_0 = \dot{a}_0)$ and $\rho_{crit,0} = 3H_0^2/(8\pi G)$, we find

$$H_0^2 - \frac{\Lambda}{3} - \frac{8\pi G}{3}\rho_0 = H_0^2 - \frac{\Lambda}{3} - \frac{\rho_0}{\rho_{crit,0}}H_0^2 =$$

$$= -kH_0^2\left(1 - \frac{\Lambda}{3H_0^2} - \frac{\rho_0}{\rho_{crit,0}}\right) = -k \quad . \tag{1.67}$$

We now define the total density contribution today given by the cosmological constant:

$$\rho_{0,\Lambda} := \frac{\Lambda}{8\pi G}, \tag{1.68}$$

and the density parameter of the cosmological constant:

$$\Omega_{0,\Lambda} := \frac{\rho_{0,\Lambda}}{\rho_{crit,0}} \quad . \tag{1.69}$$

With the last two expressions, we can write

$$H_0^2\left(1 - \Omega_{0,\Lambda} - \Omega_0\right) = -k \quad , \tag{1.70}$$

and, defining the total density parameter $\Omega_{0,TOT} := \Sigma\Omega_{0,i}$ like the sum of all contributions to the various components of the Universe (here matter and cosmological constant), finally we can write the first Friedmann equation as follows:

$$H_0^2\left(1 - \Omega_{0,TOT}\right) = -k \quad . \tag{1.71}$$

Therefore regardless of the presence of the cosmological constant or other components contributing to the total density of the Universe, we can discriminate between different values of curvature k depending on whether $\Omega_{0,TOT}$ is less than, greater than, or equal to 1.

1.2.1 Models with perfect fluid

We have seen how the Friedmann models are based on the approximation of a perfect fluid, which enters into the equations, as discussed in Section 1.1.4, with

an energy-momentum tensor given by Eq. (1.27). The perfect fluid approximation is realistic for the Universe considered on large scales. To treat the fluid as perfect it suffices that the mean free path of the constituent particles of the fluid is much smaller than the physical scales of interest. This form of the matter-energy tensor is also required for the theory to be compatible with the CP: anisotropic pressures are not allowed. To ivestigate further cosmological solutions, it is necessary to explore the relationship between pressure , p, and energy density, ρ, which requires specifying an equation of state, $p = p(\rho)$. In many cases of physical interest, we assume the general law:

$$p = w\rho \quad , \tag{1.72}$$

where w is a constant constrained inside the interval $0 \leq w < 1$, called the Zel'dovich interval. The reason why the value $w = 1$ is not accepted is the following. Consider the definition of the speed of sound:

$$c_s = \left(\frac{\partial p}{\partial \rho}\right)_S^{1/2} = \sqrt{w} \quad ; \tag{1.73}$$

if $w = 1$, the sound speed would be equal to the speed of light, which is obviously not physically permissible. On the other hand, if $w < 0$, we would have an imaginary sound speed.

In any case, the constant will assume different values depending on the component being considered. In the case of ordinary matter, where from the general relation $p = nk_BT$ assuming all particles are protons, we have

$$p_M = \frac{\rho_M}{m_p} k_B T = \frac{k_B T}{m_p c^2} \rho_M c^2 \quad , \tag{1.74}$$

where ρ_m is the matter density, k_BT is the average thermal energy of the particles, and m_pc^2 is the rest mass energy. However, for a non-relativistic ideal gas $k_BTm_pc^2$, and therefore the contribution to the total pressure of matter can be approximated by

$$p_M \approx 0 \quad . \tag{1.75}$$

This is equivalent to saying that $w = 0$. Matter of this type is called dust. Therefore, it is a good approximation to consider non-relativistic matter as negligible in its contribution to pressure.

In the case of a non-degenerate fluid of ultrarelativistic particles in equilibrium, the equation of state is of the form

$$p_r = \frac{1}{3}\rho_r \quad . \tag{1.76}$$

A fluid with an equation of state of the form given by Eq. (1.76) is usually called a radiative fluid, even though it can describe relativistic particles of any type. From Eq. (1.73), the speed of sound in a dust fluid is $c_s = 0$, while for a radiative fluid $c_s = \frac{1}{\sqrt{3}}$.

Let us now consider w as constant in time, and in particular for ordinary matter $w \approx 0$. Now we consider the adiabatic condition given by Eq. (1.55) and replace the pressure using Eq. (1.72), through a series of computations we can obtain as follows:

$$\rho \propto a^{-3(1+w)} \quad . \tag{1.77}$$

The adiabatic condition describes how the density varies in function of the scale parameter for a certain value of w.

From the above relation and Eq. (1.25), we can obtain the relations of the dust density and the radiation density as a function of the redshift:

$$\rho_M = \rho_{0,M}\left(\frac{a_0}{a}\right)^3 = \rho_{0,M}(1+z)^3 \quad , \tag{1.78}$$

$$\rho_R = \rho_{0,R}\left(\frac{a_0}{a}\right)^4 = \rho_{0,R}(1+z)^4 \quad . \tag{1.79}$$

For what concerns the cosmological constant, $w = -1$ and this enables us to evaluate the contribution of Λ on the total density:

$$\rho_\Lambda = \rho_{0,\Lambda}\left(\frac{a_0}{a}\right)^0 = \rho_{0,\Lambda} \quad . \tag{1.80}$$

We have found how the density contribution changes for the different components of the universe as function of redshift. We can thus estimate the values of the density of different componenets today:

- $\rho_{TOT} \approx \rho_{0,crit} \Rightarrow \Omega_{0,TOT} \approx 1$;

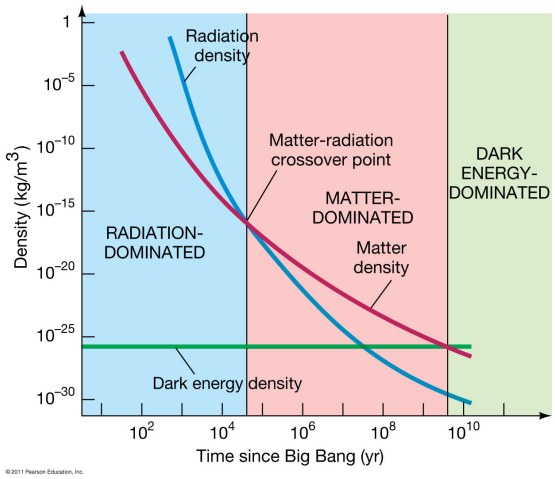

Figure 1.2: Main cosmological eras and trends of the density of universe components. Image taken from the University of Oregon website [48]

- $\rho_{0,R} = 10^{-34}$ g/cm^3 $\Rightarrow \Omega_{0,R} = 10^{-5}$;
- $\rho_{0,M} = 0.3\rho_{0,crit} \Rightarrow \Omega_{0,M} = 0.3$;
- $\rho_{0,\Lambda} = 0.7\rho_{0,crit} \Rightarrow \Omega_{0,\Lambda} \approx 0.7$.

Figure 1.2 shows the density of the different components as function of time. We can divide the Universe's history into different eras defined by the density contribution that dominates over the other. It follows that we can simplify our equations by considering only the dominant contribution in each era.

The passage from one regime to another is defined by some specific values of the redshift in which we have the equivalence between two contributions. Specifically, we have the following:

Matter-radiation equivalence:

$$\rho_{0,M}\,(1+z_{eq})^3 \equiv \rho_{0,R}\,(1+z_{eq})^4$$

$$\Rightarrow 1 + z_{eq} = \frac{\rho_{0,M}}{\rho_{0,R}} \approx 10^4 \Rightarrow z_{eq} \approx 10^4 \quad . \tag{1.81}$$

Matter-Λ equivalence:

$$\rho_{0,\Lambda} \equiv \rho_{0,M}\,(1+z_{eq})^3$$

$$\Rightarrow 1 + z_{eq} = \left(\frac{\rho_{0,\Lambda}}{\rho_{0,M}}\right)^{1/3} \approx 1.7 \Rightarrow z_{eq} \approx 0.7 \quad . \tag{1.82}$$

1.2.2 The Big Bang in a Friedmann Universe

Let us rearrange the first Friedmann equation (1.53) to express it in terms of Ω, which is a more descriptive value of the universe's composition. Considering the expression at t_0 we can write:

$$\dot{a}_0^2 - \frac{8\pi G}{3}\rho_0 = H_0^2 - \frac{8\pi G}{3}\rho_0 = H_0^2\left(1 - \frac{\rho_0}{\rho_{0,crit}}\right) = -k \quad . \tag{1.83}$$

From the above sequence of equalities, we can extract the two following relations

$$\dot{a}^2 - \frac{8\pi G}{3}\rho_0 a^2 = -k \quad , \tag{1.84}$$

$$-k = H_0^2\left(1 - \frac{\rho_0}{\rho_{0,crit}}\right) \quad , \tag{1.85}$$

that we can combine in the following;

$$\dot{a}^2 = H_0^2\left(1 - \frac{\rho_0}{\rho_{0,crit}}\right) + \frac{\rho_0 a^{-3(1+w)}}{\rho_{0,crit}}a^2 H_0^2 \quad , \tag{1.86}$$

where we have replaced the density using Eq. (1.77) in the form

$$\rho = \rho_0 a^{-3(1+w)} \quad . \tag{1.87}$$

Now using the definition of Ω_0 the above equation became:

$$\dot{a}^2 = H_0^2\left[1 - \Omega_0 + \Omega_0 a^{-(1+3w)}\right] \quad , \tag{1.88}$$

or equivalently

$$H^2(t) = \left(\frac{H_0}{a}\right)^2\left[1 - \Omega_0 + \Omega_0 a^{-(1+3w)}\right] \quad . \tag{1.89}$$

Eq. (1.89) gives us the value of the Hubble parameter as a function of time in a universe with only one component. To consider more components we just need to replace Ω_0 with $\sum_i \Omega_{w_i}$. The relation can be given also as a function of the redshift, so in its more general form it becomes:

$$H^2(z) = H_0^2(1+z)^2\left[1 - \sum_i \Omega_{0,w_i} + \sum_i \Omega_{0,w_i}(1+z)^{1+3w_i}\right] \quad . \tag{1.90}$$

Each fluid component has its parameter of state value w_i, and thus its value of the density parameter Ω_{0,w_i}. Sometimes to shorten the Eq. (1.90), it is also written as $H^2(z) = H_0^2 E^2(z)$, where $E^2(z) = (1+z)^2[...]$. Using the known Universe components today, Eq. (1.90) can be written in its extended version as follows:

$$H^2(z) = H_0^2(1+z)^2[(1-\Omega_{0,M}-\Omega_{0,R}-\Omega_{0,\Lambda})+$$

$$+\Omega_{0,M}(1+z)+\Omega_{0,R}(1+z)^2+\Omega_{0,\Lambda}(1+z)^{-2}] \quad , \tag{1.91}$$

where the quantity $(1-\Omega_{0,M}-\Omega_{0,R}-\Omega_{0,\Lambda})$ tells us how much the total energy, $\Omega_{0,tot}$, differs from the value 1, that is $1-\Omega_{0,tot}$ is a measure of the Universe curvature. At $z=0$ usually we can neglect the radiation contribution but we can't do the same at high z (early time, Fig.(1.2)).

Let us consider now the second Friedmann equation:

$$\ddot{a} = -\frac{4\pi}{3} G\,(\rho + 3p)\,a = -\frac{4\pi}{3} G\rho(1+3w)a \quad , \tag{1.92}$$

where we have used the $p = w\rho$. From the definition of c_s, to have $c_s < c$, w must be in the Zel'dovich interval, that is it has to be always true that $(1+3w) > 0$, or equivalently $\dot{a} < 0$.

The quantity $\dot{a}$ enters the equations as a squared term so that it could have either sign. However, observations support $H > 0$, thus the universe is expanding with $\dot{a} < 0$. From the above, we also know that $a(t)$ has to have negative concavity and no flex. All this means that $a(t)$ has to intersect the t, thus it must exist an initial instant in which the Universe began, the so-called Big Bang (Figure 1.3).

Notice that for $\rho \propto a^{-3(1+w)}$ then $\lim_{a \Rightarrow 0} \rho = \infty$. Thus when $a = 0$ the density of the universe is infinite, and with that also the temperature.

The Big Bang cannot be avoided in a model of the Universe based on the Friedmann equations, unless we change the definition of w, or rejecting the assumptions of isotropy and homogeneity. However, the Big Bang should not be considered as a real initial condition, but as a limit of the model, being based on a classic field theory. Indeed, to model the universe below the Planck time $t_p \sim 10^{-43}$sec, the gravitational field is expected to be quantized.

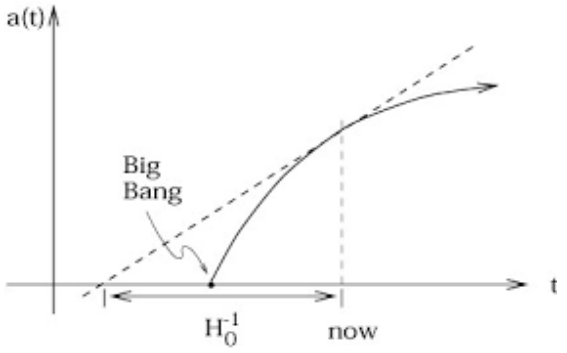

Figure 1.3: Evolution of the scale parameter $a(t)$ in Friedmann models.

1.2.3 Flat Universe

We will now focus on finding solutions to the Friedmann equations starting from the simplest case of a flat universe. This model considers a single-component fluid. In a flat Universe, $\Omega_0 = 1$ so the Eq. (1.88) becomes:

$$\dot{a}^2 = H_0^2 \left[1 - \Omega_0 + \Omega_0 \left(\frac{a_0}{a} \right)^{1+3w} \right] = H_0^2 a^{-(1+3w)} \tag{1.93}$$

$$\Rightarrow \dot{a} = H_0 a^{-\frac{1+3w}{2}} \quad . \tag{1.94}$$

We now integrate the above expression:

$$\frac{\mathrm{d}a}{\mathrm{d}t} = const \cdot a^{-\frac{1+3w}{2}} \Rightarrow a^{\frac{1+3w}{2}} \, \mathrm{d}a = const \, \mathrm{d}t \tag{1.95}$$

from which we obtain

$$a(t) = \left(\frac{t}{t_0} \right)^{\frac{2}{3(1+w)}} \quad . \tag{1.96}$$

For w inside the Zel'dovich interval, the expansion never stops. From Eq. (1.25) the above expression can be inverted to obtain

$$t = t_0 (1+z)^{-\frac{3(1+w)}{2}} \quad . \tag{1.97}$$

It is interesting also to compute how the Hubble parameter changes

$$H(t) = \frac{\dot{a}(t)}{a(t)} = \frac{[2/3(1+w)] t^{[2/3(1+w)]-1} \cdot const}{const \cdot t^{[2/3(1+w)]}} = \frac{2}{3(1+w)} t^{-1} \quad . \tag{1.98}$$

General	$w = 0 (EdS)$	$w = 1/3$
$a(t) = \left(\frac{t}{t_0}\right)^{\frac{2}{3(1+w)}}$	$a(t) \propto t^{2/3}$	$a(t) \propto t^{1/2}$
$t = t_0(1+z)^{-\frac{3(1+w)}{2}}$	$t \propto (1+z)^{-3/2}$	$t \propto (1+z)^{-2}$
$H(t) = \frac{2}{3(1+w)} t^{-1}$	$H(t) = \frac{2}{3t}$	$H(t) = \frac{1}{2t}$
$t_0 = \frac{2}{3(1+w)} \frac{1}{H_0}$	$t_0 = \frac{2}{3H_0}$	$t_0 = \frac{1}{2H_0}$
$q = \frac{1+3w}{2}$	$q = \frac{1}{2}$	$q = \frac{1}{2}$
$\rho = \frac{1}{6\pi G(1+w)^2} \frac{1}{t^2}$	$\rho = \frac{1}{6\pi G} \frac{1}{t^2}$	$\rho = \frac{3}{32\pi G} \frac{1}{t^2}$

Table 1.1: The main relationships in the flat models in three primary cases, that is the general case, pure matter universe, and pure radiation universe.

$H(t)$ is a decreasing function of time, thus the expansion of the Universe slows for $t \Rightarrow \infty$ and increases going towards the Big Bang.
The other fundamental parameter we consider is the deceleration parameter, which provides a dimensionless measure of the second derivative. From its definition and the derivatives calculated based on Eq. (1.96), we have

$$q(t) := -\frac{\ddot{a}(t)a(t)}{\dot{a}^2(t)} = \frac{1+3w}{2} \quad . \tag{1.99}$$

In an Einstein-de Sitter (EdS) universe, when we have only dust ($w = 0$), the expansion decelerates uniformly. Deceleration is a general feature of models derived from the Friedmann equations, but in the case of EdS there is no time dependence in the deceleration.

In Table 1, a summary of the main general results of a flat model is provided along with corresponding relations for two cases of single-component Universes: the case of a pure matter Universe ($w = 0$) and the case of a pure radiation Universe ($w = 1/3$).

A general property of flat models is that the scale parameter grows indefinitely with time, with a constant deceleration parameter. Increasing the value of w and thus increasing the pressure leads to an increase in the deceleration parameter. Conversely, a negative value of w, indicating behavior similar to that of a cosmological constant, corresponds to negative pressure, and results in accelerated expansion. Finally, we note that in these models, the age of the Universe, t_0, is closely linked to the current value of the Hubble parameter:

$$t_0 = \frac{2}{3(1+w)} \frac{1}{H_0} \quad . \tag{1.100}$$

1.2.4 Curved Universes: general proprieties

We will continue to consider a Universe composed of a single-component fluid, but in this case, we have $\Omega_0 \neq 1$. Let us revisit Eq. (1.88):

$$\left(\frac{\dot{a}}{a_0}\right)^2 = H_0^2[(1-\Omega_0) + \Omega_0 a^{-(1+3w)}] \quad . \tag{1.101}$$

There will be a regime in which one of the two terms of Eq. (1.101) dominates over the other and vice versa. This implies that we can find a value a^* such that the two terms are equal:

$$|1-\Omega_0| = \Omega_0 (a^*)^{-(1+3w)}$$

$$\Rightarrow a^* = \left(\frac{|1-\Omega_0|}{\Omega_0}\right)^{-\frac{1}{1+3w}} \quad . \tag{1.102}$$

When $a < a^*$ we have

$$\Omega_0 (a^*)^{-(1+3w)} \gg 1-\Omega_0 \quad , \tag{1.103}$$

and so the second term wins over the first one, so we can write:

$$\dot{a}^2 = H_0^2 \Omega_0 a^{-(1+3w)} \quad , \tag{1.104}$$

that differs from the flat case only for a factor Ω_0. This tells us that the curved Universes act nearly as flat for $a < a^*$. The different relations for the quantity of the Universe will have similar behaviors

$$H(t) = H_0 (1+z)^{\frac{3(1+w)}{2}} \Omega_0 \quad , \tag{1.105}$$

$$t = t_0 (1+z)^{-\frac{3(1+w)}{2}} \Omega_0^{-1/2} \quad . \tag{1.106}$$

In this case, the space is significantly curved only when $a > a^*$, while before this term it acts like a flat universe. Thus it is a good approximation to ignore the curvature term in the early Universe (until $z \sim 10$). On the other hand, at low z the sign of Ω is important, and two different scenarios are possible for open and closed universes.

1.2.5 Open universes

Models with $\Omega < 1$ are called open models. In these models, the scale parameter, $a(t)$, grows indefinitely with time, similar to what occurs EdS models.
From Eq. (1.101) we have that $\dot{a}$ never goes to zero; thus if we assume that the scale function is positive at a certain time t_0, its derivative, $\dot{a}$, is always positive. The second term in (1.101) is negligible for $a \gg a^*$ and thus for these universes we have the following relation:

$$\frac{\mathrm{d}a}{\mathrm{d}t} = \dot{a} = H_0 \left(1 - \Omega_0\right)^{1/2} \quad . \tag{1.107}$$

Thus the growth of a in an open universe is linear with time. We can also derive the following relations:

$$H = \frac{\dot{a}}{a} \propto \frac{1}{t} \quad , \tag{1.108}$$

$$q = -\frac{\ddot{a}a}{\dot{a}^2} \Rightarrow 0 \quad , \tag{1.109}$$

$$\rho = \rho_0 a^{-3(1+z)} \propto \rho_{0,crit} \quad , \tag{1.110}$$

we notice that the expansion is free and not decelerated.

1.2.6 Closed Universes

Models with $\Omega > 1$ are called closed models. In this case, there exists a time at which the first derivative of the scale factor, $\dot{a}$, is zero. From Eq. (1.101) with $\dot{a} = 0$, we find the value of a for which the derivative is null, that is the maximum for the function $a(t)$ is :

$$(1 - \Omega_0) + \Omega_0 \left(\frac{a_0}{a_{\max}}\right)^{1+3w} = 0$$

$$\Rightarrow a_{\max} = a_0 \left(\frac{\Omega_0}{\Omega_0 - 1}\right)^{1/(1+3w)} \quad . \tag{1.111}$$

At this maximum value of the scale factor we have a minimum density:

$$\rho\left(a_{\max}\right) = \rho_0 (a_{\max})^{-3(1+w)} = \rho_0 \left(\frac{\Omega_0 - 1}{\Omega_0}\right)^{\frac{3(1+w)}{1+3w}} \quad . \tag{1.112}$$

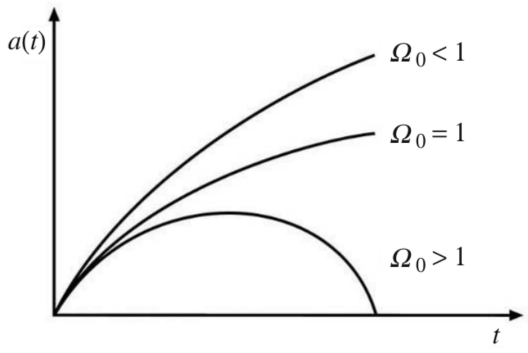

Figure 1.4: Evolution of the scale parameter $a(t)$ for flat universes, open universes and closed universes.

Equation (1.101) is quadratic, so after the maximum the curve is symmetric and decreasing. The close model predicts a second singularity: the universe will close on itself, in a phenomenon called the Big-Crunch. Finally, it is worth noting that in a closed model, quantum gravity theories generally predict a Universe that oscillates between consecutive Big Bangs and Big Crunches.

Figure 1.4 shows the behavior of the scale function a(t) for the three different cases considered: flat Universe, open Universe, and closed Universe.

Chapter 2

Growth of density perturbations

In this chapter, we will introduce the main concepts and specific notions that serve as the theoretical basis for the method used in this thesis work. We will briefly describe the evolutionary process that has led to the formation of gravitational structures from small perturbations in the primordial density field of the Universe. Then we will introduce the concept of clustering, with particular attention to the two-point correlation function.

2.1 Density perturbations

Having described the temporal evolution of the matter density of the Universe (1.77) and of its scale factor (1.96), we can reconstruct the evolutionary history of the dominant components and the expansion of spacetime. In particular, we can identify the time when radiation and matter decoupled, a period when the Universe was much denser and hotter than it is today. It is astonishing to notice the homogeneity and isotropy of the CMB when we consider two opposite directions in the sky. In Fig. 2.1 we can see the famous map of the temperature fluctuations produced by the European Space Agency (ESA) Planck mission (2013) which shows the almost perfect homogeneity of the CMB. The issue arises from the fact that regions so far apart in the CMB present nearly the same temperature and other physical properties. Apparently these parts of the Universe never exchanged information, because they are at distances larger than those that can be reached from the Big Bang due to the maximum velocity of the signal, that is c. This is referred to as the horizon problem. For this reason, the standard cosmological model now includes the so-called inflationary theory [28], which was developed specifically to explain this issue. The inflationary theory posits that in

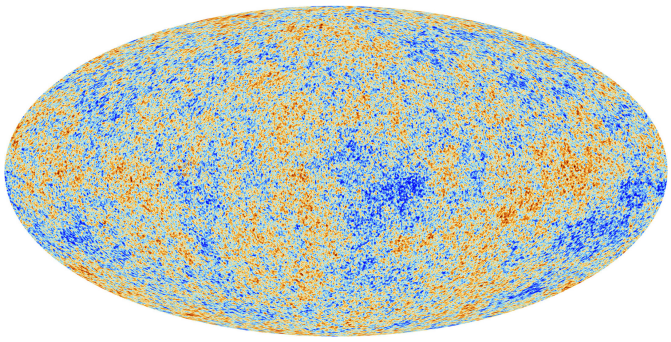

Figure 2.1: The anisotropies of the Cosmic Microwave Background (CMB) as observed by Planck. It shows tiny temperature fluctuations that correspond to regions of slightly different densities, representing the seeds of all future structure: the stars and galaxies of today. Imagine taken by the ESA website [8].

its "initial" phases (until around $10^{-35}s$ after the Big Bang), the dimension of the observable Universe was small enough to enable its parts to enter causal contact, justifying the homogeneity and isotropy we observe today. Then the Universe entered a very fast (almost exponential) expansion phase called inflation, which increased its dimensions by a factor between 10^{25} and 10^{30}. The CMB, which was generated after the inflationary phase, retains the trace of the initial homogeneity despite the cosmological horizons of two distant regions are not overlapping. Specifically, the cosmological horizon, defined as:

$$R_H = a(t) \int_0^t \frac{cdt'}{a(t')} \quad , \tag{2.1}$$

represents the maximum distance a particle can have traveled in the cosmological time t, thus establishing an observational limit.

Gravitational structures, such as galaxies and galaxy clusters, originate from the initial inhomogeneities that were generated at the end of the inflationary phase. In fact, despite the validity of the CP on the largest scales, the CMB is not perfectly isotropic and presents small temperature perturbations. They correspond to similarly small disomogeneities in the matter density field, on the order of $\Delta\bar{\rho} \sim 10^{-5}$, where $\bar{\rho}$ is the average density of the Universe. Under proper conditions, these fluctuations in the density field can grow in various ways through gravitational instability, and interact with each other to generate the collapsed structures surrounding us.

2.2 Jeans theory

Let us now explore how it is possible to analytically treat the growth of density perturbations. A simplistic description of this phenomenon is based on the collapse of a spherical gas cloud in Newtonian mechanics, where its kinetic and gravitational potential energies are related using the virial theorem. By balancing these two terms, it is possible to obtain a threshold dimension for the instability of the structure, known as Jeans instability. The condition of equilibrium is given by the expression:

$$\frac{1}{2}Mv^2 = \frac{G_N M^2}{R} \sim G_N M \rho R^2 \quad , \tag{2.2}$$

where M is the mass of the structure, ρ is the density, R is the cloud radius, G_N is the gravitational constant, and v is the velocity, which is linked to the temperature. From Eq. (2.2), we can compute the critical radius for instability, R_J:

$$R_J = v(2G_N\rho)^{-\frac{1}{2}} \quad . \tag{2.3}$$

The gravitational force causes the clouds to collapse with dimensions greater than R_J. In the more complex cases where we consider the entire Universe, we need to extend the Jeans theory and consider a uniform medium in which small density perturbations, $d\rho$, give rise to pressure waves. The relation between pressure and density can be written as follows:

$$dP = c_s^2 d\rho \quad , \tag{2.4}$$

where c_s is the sound speed in the medium considered. To describe the general approach of Jeans theory, we will use the simple case of a static Universe. The line of thought remains the same for non-static cases but requires the necessary adjustments. First, we consider the system of equations that can handle an unperturbed initial state. This system is described by the continuity equation, the Euler equation of fluid dynamics, the Poisson equation for gravity, and an equation of state for the pressure, P, as a function of density, ρ, and entropy, (S). If we assume only adiabatic transformations ($S = const$), we can neglect the dependency

of P on the entropy. The full set of equations is the following:

$$\begin{cases} \frac{\partial \rho}{\partial t} + \nabla \cdot (\rho \mathbf{v}) = 0; \\ \frac{\partial \mathbf{v}}{\partial t} + (\mathbf{v} \cdot \nabla)\mathbf{v} = -\frac{\nabla P}{\rho} - \nabla \Phi; \\ \nabla^2 \Phi = 4\pi G_N \rho; \\ P = P(\rho, S) = P(\rho), \end{cases} \tag{2.5}$$

where in this case Φ is the classical Newtonian potential. Next, we introduce a linear perturbation, at first order, to the unperturbed solutions (also called background solutions):

$$\begin{cases} \rho = \rho_b + \delta\rho; \\ P = P_b + \delta P; \\ \Phi = \Phi_b + \delta\Phi; \\ \mathbf{v} = \delta\mathbf{v}. \end{cases} \tag{2.6}$$

These expressions are then inserted into our system (2.5). The goal is to find the perturbed solutions in Fourier space, which take the form of plane waves, and from these, obtain a dispersion relation. In our case, we will have:

$$\omega^2 = k^2 c_s^2 - 4\pi G_N \rho_b \quad . \tag{2.7}$$

The waves generated from the density perturbations are identified by the wave number k, and they are characterized by a limited (oscillating) amplitude for $\omega^2 > 0$ or an exponential progression for $\omega^2 < 0$. As in the case of a gas cloud, the critical value for instability is given by the limit case $\omega^2 = 0$. It is possible to find the Jeans wave number and the Jeans wavelength, analogous to the critical radius determined above as follows:

$$k_J = \sqrt{\frac{4\pi G_N \rho_b}{c_s^2}} \Rightarrow \lambda_J = \frac{2\pi}{k_J} = \sqrt{\frac{\pi c_s^2}{G_N \rho_b}} \quad . \tag{2.8}$$

As before, perturbations with wavelengths greater than λ_J will collapse and grow exponentially.

In the case of an expanding Universe, it is also possible to describe the growth, or the dissipation, of the density perturbations for the different components of the cosmic fluid analytically in linear order. However, there are some important

differences in the approach worth noticing. First of all, it is necessary to take into consideration the inhibitor effect of the expansion of the Universe on the development of the fluctuations. We will summarize the main results for the instability evolution, introducing a variable named density contrast:

$$\delta = \frac{\rho - \bar{\rho}}{\bar{\rho}} \quad , \tag{2.9}$$

where the density ρ is a function of space and time, and $\bar{\rho}$ is the average density of the background. We can distinguish two main scenarios:

- outside the cosmological horizon, R_H, the matter does not interact directly thus we can neglect the equation of fluid dynamics. It is accurate to consider only the Friedmann equations (1.28), (1.29). The perturbation will behave like a closed Universe, overdense and embedded in a flat background Universe. Equaling the Hubble parameters obtained from the respective Friedmann equations of the two Universes, we can write the following expression for the density contrast

$$\delta = \frac{3}{8\pi G_N \bar{\rho} a^2} \quad . \tag{2.10}$$

  From Eqs. (1.77) and (2.10) we can write:

$$\delta \sim a^{(1+3w)} \quad . \tag{2.11}$$

  Since the constant w depends on the dominant component of the Universe at each epoch, we will distinguish the Universe before and after the matter-radiation equivalence ($\rho_M = \rho_R$). Using Eq. (1.96) for $a(t)$, we have that before the equivalence, when the radiation is the dominant part, $w = 1/3$ and $\delta_R \sim t^{1/2}$. On the other hand, in the epoch in which matter is the dominant part, $w = 0$ and $\delta_M \sim a \sim t^{2/3}$. In both cases, the perturbations will grow.

- Inside the cosmological horizon, it is necessary to approach the problem in a different way. Specifically, we have to consider the Eq. (2.5) in comoving coordinates. The main consequence is that, before the equivalence, in a relativistic fluid the speed of sound is $c/\sqrt{3}$. Therefore we obtain a Jeans length greater than R_H that corresponds to having no growth of the perturbations:

the pressure travels too fast to permit the collapse of the fluctuations. Similarly, before the equivalence, the fast expansion of the Universe restricts also the growth of dark matter perturbations. After the equivalence, when matter became dominant, the development of dark matter perturbations with wavelengths greater than λ_J follows a trend similar to that found outside the cosmological horizon. The baryons, however, remain coupled to the radiation due to electromagnetic interactions (Thompson scattering) until the decoupling epoch. After decoupling, the baryon perturbations find the potential wells created by dark matter and, influenced by gravitational attraction, begin to grow in a similar manner ($\delta_{bar} \simeq \delta_{DM}$).

The dark matter is observable only through gravitational effects. It represents the main component (nearly 85%) of the matter density of the Universe and, as we have seen, provides the structures inside which the large-scale baryonic matter evolves until today.

In the context of determining how dark matter influences baryonic structures, we need to introduce two different models: one based on the assumption of hot dark matter (HDM) and another on cold dark matter (CDM). The mass of the dark matter particles determines when they decouple from the radiation. HDM is composed of less massive particles that remain relativistic after decoupling, while CDM consists of more massive particles that become non-relativistic before decoupling. Starting from the definition of the Jeans wavelength we can introduce a corresponding Jeans mass beyond which the perturbations can grow:

$$\lambda \sim \frac{v}{\sqrt{\rho}} \Rightarrow M_J \sim \rho \lambda_J^3 \sim \frac{\rho v^3}{\rho^{3/2}} \quad . \tag{2.12}$$

Different velocities result in different Jeans masses; with dissipative phenomena for dark matter, this determines a critical mass above which collapse can occur. If the perturbation has a corresponding Jeans mass below this critical mass, the density wave will be canceled. During the dark matter decoupling and radiation-matter equivalence, we observe the maximum value for the Jeans mass. In the model with HDM, this value corresponds to around $10^{16} M_\odot$ while in the model with CDM corresponds to $10^{5-6} M_\odot$. These values tell us how today structures have formed, and the assumption of one model rather than the other completely changes the history of large-scale perturbations. In the case of HDM, only the most massive density perturbations can collapse, which then fragment to form smaller structures; this dark matter halo formation process is called top-down. On the

other hand, with CDM, the collapse of small fluctuations is also possible, so we expect that large structures are formed by the association of smaller structures, in a bottom-up process.

2.3 Correlation function

We have examined in the above section how and under what conditions primordial density fluctuations can grow and evolve. Now, we consider how we can extract cosmological information from the statistical properties of the large-scale density perturbations. Matter clustering refers to the statistical spatial properties of structures, that gather in groups of various sizes. This phenomenon can be studied from various perspectives. In particular, we are interested in analyzing the clustering through the two-point correlation function, 2PCF.

Let us again consider the density contrast defined in Eq. (2.9). According to Bayes theorem, the probability of having a density perturbation δ_1 in a comoving volume dV_1, at a certain comoving distance r from another perturbation δ_2 in a volume dV_2, is

$$dP_{12} \equiv dP(1|2) = dP(1)dP(2|1) \quad . \tag{2.13}$$

If the density distribution was completely random, that is the objects were distribuited homogeneously, we would have

$$dP_{12} = \bar{\rho}^2 dV_1 dV_2 \quad . \tag{2.14}$$

Since the perturbations grow due to gravitational interactions that drive their dynamics, it is necessary to introduce a factor that accounts for how the distribution deviates from a random one. This can be parameterized by a 2PCF, $\xi(r)$, which modifies the above probability as follows:

$$dP_{12} = \bar{\rho}^2 dV_1 dV_2 [1 + \xi(r)] \quad . \tag{2.15}$$

The terms in Eq. (2.15) can be linked to the Bayes theorem as follows:

$$\bar{\rho} dV_1 = dP(1) \quad , \tag{2.16}$$

$$\bar{\rho}[1 + \xi(r)]dV_2 = dP(2|1) \quad . \tag{2.17}$$

Thus, by definition, $\xi(r)$ is equal to 0 when the distribution is random at each r, so that we can regain Eq. (2.14).

Therefore, the correlation function of the density field represents the probability excess or deficiency, compared to a random distribution, of finding two perturbations at a certain distance. An explicit definition of $\xi(r)$ is the following:

$$\xi(r) = \frac{\langle \rho(x)\rho(x+r)\rangle - \bar{\rho}^2}{\bar{\rho}^2}$$

$$= \frac{\langle [\rho(x) - \bar{\rho}][\rho(x+r) - \bar{\rho}\rangle}{\bar{\rho}^2}$$

$$= \langle \delta(x)\delta(x+r)\rangle \quad , \tag{2.18}$$

where the operator $\langle\rangle$ indicates the spatial average on all the considered volume. We can notice also how the correlation function is proportional to δ^2.

2.3.1 Tracers of the density field

Until now, we have considered the correlation function of the continuous density field of matter, a quantity that is not easy to observe directly. It is therefore necessary to use some assumptions that enable us to utilize astrophysical objects as tracers for the total density distribution of matter. We have seen in the previous section how the baryon density perturbations grow differently from those of dark matter. After decoupling with radiation, baryonic matter collapses into the potential wells already formed by dark matter. The formation of structures, like galaxies, happens inside these potential wells not only because of gravity but also due to various astrophysical processes (such as, e.g., radiative cooling, collisional cooling, etc.). Thus observable astrophysical objects do not directly trace the continuous density distribution of matter; nevertheless, a link exists between them.

In general, the density contrast, δ_{obj}, of any class of object is a function of the total density contrast, δM:

$$\delta_{obj} = f(\delta_M) \quad . \tag{2.19}$$

The function f, which links the two density contrasts, must account for all the astrophysical processes that lead to the formation of structures starting from the

initial density perturbations and can depend on any physical characteristic of the objects. In the first approximation, we can assume that f is a linear function of the matter density field, and introduce the bias factor b as follows:

$$\delta_{obj} = b\delta_M \quad , \tag{2.20}$$

where b provides the level of clustering of a given class of objects. In particular, when $b > 1$, the objects are more clustered than the underlying matter distribution. It can be derived the following relation:

$$b = \sqrt{\frac{\xi_{obj}}{\xi_M}} \quad . \tag{2.21}$$

On intermediate scales, around $10 - 50$ Mpc h^{-1}, the 2PCF can be described by a power law of the following kind:

$$\xi(r) = \left(\frac{r}{R_0}\right)^{-\gamma} \quad , \tag{2.22}$$

where R_0 is the scale radius, also called the correlation length, at which $\xi(R_0) = 1$. The values of R_0 and of the slope γ vary depending on the properties of the selected class of objects and the redshift [18]. In Figs.2.2 and 2.3 we can see how the slope γ, while showing evolution with redshift, is substantially constant with the stellar mass of the galaxies and the absolute magnitude, $\gamma \approx 1.8$ [46]. On the other hand, the correlation length shows a clear dependency on the stellar mass and the absolute magnitude, which increases also with the redshift.

2.3.2 Correlation function estimator

To estimate the 2PCF of a discrete distribution of tracers, we shall compare the number of object pairs with the number of pairs in a random catalogue with the same selection effects as in the tracer catalogue. The simplest estimator of the 2PCF is the so-called Peebles-Hauser estimator, also called the natural estimator [49]:

$$\xi(r) = \frac{N_{RR}}{N_{DD}} \frac{\mathrm{DD}(r)}{\mathrm{RR}(r)} - 1 \quad , \tag{2.23}$$

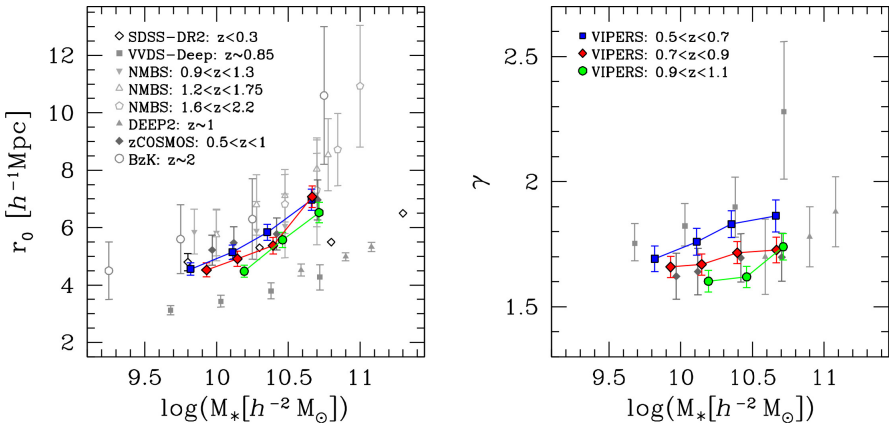

Figure 2.2: The clustering parameters of the Vimos Public Extragalactic Redshift Survey (VIPERS) galaxy catalogue. The blue points are galaxies measured in the redshift interval $[0.5, 0.7]$, the red points in the interval $[0.7, 0.9]$, and the green points in the interval $[0.9, 1.1]$. Figure taken from [46].

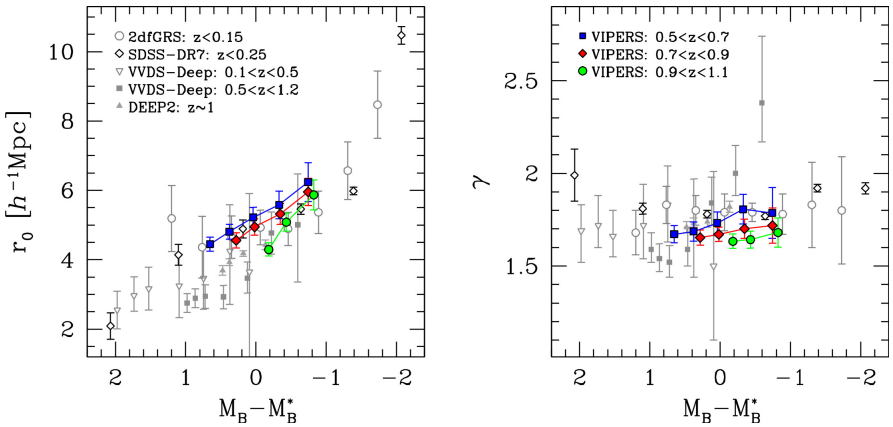

Figure 2.3: Similar results to those reported in Fig. 2.2, but as a function of the B-band absolute magnitude. Figure taken from [46].

where $\mathrm{DD}(r)$ is the number of object pairs at a comoving distance r, $\mathrm{RR}(r)$ is the number of pairs of the random catalogue, and $\frac{N_{DD}}{N_{RR}}$ is the fraction between the number of couples of the two catalogues.

This estimator is particularly sensible to fluctuation given the discrete nature of the distributions ([35], [38]) and thus it does not provide an optimal choice for measuring the 2PCF. It is indeed more efficient to use e.g. the estimator proposed by Landy-Szalay [39] (LS estimator), which also includes the cross-pairs $\mathrm{DR}(r)$ between the tracer and random catalogues:

$$\xi_{LS}(r) = 1 + \frac{N_{RR}\mathrm{DD}(r)}{N_{DD}\mathrm{RR}(r)} - 2\frac{N_{RR}\mathrm{DR}(r)}{N_{DR}\mathrm{RR}(r)} \quad . \tag{2.24}$$

This estimator is less affected by the fluctuations due to the discrete nature of the catalogues, which introduce only second-order terms. Its variance is almost completely Poissonian, at small scales relative to the volume of the catalogue, and thus depends only on the square root of the number of pairs in the separation bins, $\sqrt{\mathrm{DD}(r)}$. In our thesis work, we exclusively used the LS estimator for the two-point correlation function, using a fast `C++` algorithm, which will be described in Chapter 5.

Chapter 3

The Magneticum cosmological simulation

The primary goal of numerical simulations is to solve problems that cannot be addressed analytically. For dynamical simulations, where we study a system of gravitationally interacting particles, the process involves discretizing the density field that determines the gravitational potential and computing the forces acting on each mass element at discrete time intervals. The finer the discretization of the density field and the time intervals, the more accurate the simulation. However, increasing the mass resolution to represent the actual density field better, or improving the temporal resolution, impacts the computational time significantly.

In this chapter, we will introduce the fundamentals of numerical simulations in the Newtonian regime and explore the different approaches used to implement equations for gravity in dynamical simulations and hydrodynamics in hydrodynamic simulations. Following this introduction, we will describe the *Magneticum* cosmological hydrodynamic simulation and the main characteristics of the catalogues extracted from it. These are the catalogues on which the AP test has been performed in this thesis work.

3.1 N-body simulations

By modelling the gravitational potential generated by a discrete distribution of simulated particles, it is possible to update the position and velocity of each particle at each time interval while measuring the total force acting on it. This operation can be performed in different ways, depending on the desired resolution and computing time.

In this section, we will briefly analyse the motion equations of a generic cosmological simulation, and then describe the principal methods used to implement a code for N-body simulations.

3.1.1 Equations of motion

In Newtonian dynamics, the motion of a particle of unitary mass is given by

$$\ddot{\mathbf{r}} = -\nabla\Phi \quad , \tag{3.1}$$

where $\mathbf{r}$ is the particle position, $\ddot{\mathbf{r}}$ its acceleration and Φ is the gravitational potential given by the Poisson equation:

$$\nabla^2\Phi = 4\pi G\rho(t,\mathbf{r}) \quad , \tag{3.2}$$

where $\rho(t,\mathbf{r})$ is the matter density that generates the gravitational field. Generalizing for a possible expanding space and using for convenience the comoving coordinates, $\mathbf{x}$, the equations that describe the position and velocity at each point become:

$$\begin{cases} \ddot{\mathbf{x}} + 2\frac{\dot{a}\dot{\mathbf{x}}}{a} = -\frac{\nabla\Phi}{a^2}; \\ \nabla^2\Phi = 4\pi[\rho(t,\mathbf{x}) - \overline{\rho}] = \frac{3H_0\Omega_0\delta}{2a}; \end{cases} \tag{3.3}$$

where a is the scale factor and H_0 is the Hubble constant defined in Chapter 1, while $\overline{\rho}$ is the average density.

These equations must be integrated for each particle at each time interval, with the positions and velocities at a general time t_1 that become the initial conditions for the integration to a time $t_2 > t_1$.

3.1.2 Primary implementations for N-body simulations

Particle-particle

The most direct way to implement a code that integrates Eq. (3.3) is called the particle-particle (PP) method. This involves computing the force acting on each particle at each time interval, Δt, as the sum of every contribution from all other particles. At each time interval, all the force contributions are summed for all the $N(N-1)/2$ particle pairs, and the motion equations are integrated to compute the new velocities and positions for each particle. When the time counter is updated, all the forces are reset to zero, and the previous process is iterated.

It is necessary to note that the gravitational force at a small distance tends to infinity, and this can create numerical problems. Therefore, avoiding interaction on small scales is opportune because they require a very high temporal resolution to be accurately represented. Thus a softening parameter, ϵ, is introduced in the computation of the acting force between a pair of particles at a distance r. The force takes the following form:

$$F(r) \sim \frac{1}{(r^2 + \epsilon^2)} \quad . \tag{3.4}$$

The main problem with the PP method is the fact that at each time step, it is necessary to compute $N(N-1)/2 \sim N^2$ forces. This makes the computing time proportional to the square of the particle number. The PP approach is generally applied only to the systems with a small number of particles.

Particle-mesh

Suppose we introduce a spatial grid in which each cell mediates the density field of the contained particles. In that case, it is possible to reduce the needed time to compute the gravitational potential generated by each particle. Using a grid means mediating the density locally and thus the gravitational potential.

This method called particle-mesh (PM), is generally implemented by moving into the Fourier space. The approach significantly reduces the computational time, which, in the first approximation, becomes proportional to $N + M^3 \log M^3 \ll N^2$, where N is the number of simulated particles and M the number of nodes in the grid.

Even though the PM method is advantageous in terms of computational time compared to the PP method, it leads to a significant loss of resolution due to the averaging of the gravitational potential over the cells, especially at small scales.

Particle-particle-particle-mesh

A third approach in this type of analysis is represented by the hybrid method called particle-particle-particle-mesh (P^3M) introduced by Hockney in the 1971 [31]. If we define the critic radius r_c, the acting force on every particle can be broken down as follows:

$$F = F_{r<r_c} + F_{r>r_c}, \tag{3.5}$$

in which $F_{r<r_c}$ represents the contribution to the total force given by the particles near the particle considered. This contribution is computed with the PP method, which ensures a good resolution at a short range. If we define N_{r_c} as the

number of particles contained in the sphere of radius r_c, the contribution to the computational time of this part of the method is proportional to $NN_{r_c} < N^2$.

On the other hand, $F_{r>r_c}$ represents the contribution to the force caused by particles far away, which is modelled as an average density field. Thus, at these scales a grid is used, and a PM method. As we have seen in the previous section, this approach significantly saves time but results in less accuracy in representing the long-distance force. The computational time for this contribution is the same as observed for the PM method.

We now make two considerations on the P^3M. The first is the fact that we need to define a critical distance r_c which identifies the scale within the PP method can be used. Choosing a critical distance that is too large results in the method resembling a pure PP approach, thereby increasing the calculational time. Using a critical distance that is too short instead makes the method similar to a pure PM approach, worsening the resolution. Furthermore, it is not trivial having $F_{short}(r_c) = F_{long}(r_c)$. Hockey and Eastwood [23] have shown how it is possible to make the force (and its derivates) continuous at r_c through adequate filtering.

The second consideration is about the gravitational attraction between particles. As clustering increases, so does the number of pairs within the critical radius. Consequently, at each time step, the computational time grows, making the P^3M method less efficient over time.

In a purely cosmological context, another problem arises. For distances within the critical radius, the P^3M operates exactly like the PP method, thus the softening parameter, ϵ, is used to limit the interactions on very small scales. The latter could cause significant deflections in the particles' motions, making it difficult to track their dynamics accurately. We can think of the ϵ parameter as a physical dimension of the particles, below which gravitational interactions do not occur. In cosmological simulations, the particles do not represent specific physical entities (such as galaxies), but just mass elements. Determining an appropriate value for ϵ is not straightforward; therefore, it is necessary to set a value for ϵ based on the stability of the utilized codes.

Hierarchical tree

We introduce here the numerical method called hierarchical tree (HT), as in the PM^3 method, also in this case, the acting forces on each particle are computed in different ways depending on the distance: the force generated by close particles is computed by direct sum, like in the PP method, while for the long interactions are computed in this case using the multipole expansion of the potential.

At each time step, a hierarchical tree of pseudo-particles is defined. The simulated volume is divided into cells, each of which is iteratively subdivided into sub-cells, until each cell contains at most one particle.

The interaction between a given particle and a group of distant particles can be approximated by considering the interaction between the particle and a pseudo-particle located at the center of mass of the group. The potential of this pseudo-particle can be computed as the sum of his multipole expansion, truncated at a certain order. For each pseudo-particle, we compute the ratio between its size and its distance from the considered particle. If this value is less than a certain fixed parameter θ, the internal structure of the pseudo-particle is negligible, and a multipole expansion can approximate its potential. In the other case, if the ratio is greater than θ, we must consider a sub-cell and repeat the operation.

In this way, the dependency of the computational time on the number of particles decreases from N^2 of the PP method to $N\log N$.

3.2 Hydrodynamic simulations

So far we have described methods that enable us to simulate a physical system in which the only force is gravity. This can be sufficient if we want to study the dynamic of a non-collisional system, like the interactions of galaxies and clusters of galaxies on large scales. Every information on the hydrodynamic state of the simulation particles is neglected.

To add hydrodynamics, we need to consider the physics of baryonic gas in addition to gravity. This involves associating each particle with its state functions. If $\mathbf{v}$ is the velocity of every fluid element, P the pressure, and ρ the density, we need to add and integrate the Euler equation into the motion equation at each time step:

$$\frac{\partial \mathbf{v}}{\partial t} + (\mathbf{v} \times \nabla)\mathbf{v} = -\frac{\nabla P}{\rho} - \nabla \Phi \quad , \tag{3.6}$$

together with the continuity equation, that assuming homogeneity and isotropy ($\nabla P = \nabla \rho = 0$) becomes:

$$\frac{\partial \rho}{\partial t} + \left(\rho + \frac{P}{c^2}\right) \nabla \mathbf{v} = 0 \quad . \tag{3.7}$$

Finally, we need the state equation:

$$P = P(\rho, S) \quad . \tag{3.8}$$

The above equations must be solved at each time step, along with the gravity equations. There are at least two approaches to incorporating gas physics into N-body simulations.

Eulerian approch

For this approach, we consider a grid of points to solve the equations of the fluid in question. Hydrodynamic interactions are short-range, so integrating the equations within each cell requires only the boundary conditions from the adjacent grid points. The spatial resolution of this type of code can be enhanced by either refining the grid or using a dynamic grid that automatically adjusts to different density zones. In cosmology, it is crucial to improve the grid resolution as well as the mass resolution of dark matter particles [10]. This approach is particularly efficient in describing shock and discontinuity and can also be adapted to include other phenomena, as for example the magnetohydrodynamics [55].

This method thus utilizes a grid that mediates the hydrodynamic properties of the fluid. It aligns well with previous approaches that use a grid (such as PM) to handle the gravitational potential.

Lagrangian approch

An alternative approach, called Lagrangian, is the one that uses the so-called smooth particle hydrodynamics (SPH). The characteristics of the thermodynamic fluid, like pressure and temperature, can be found at each point by appropriately mediating the simulation particles. We use the word "smoothed" because we transition from a discrete distribution of particles to a fluid with continuous properties through coarse-graining. For this reason, the method is not indicated to treat shocks and discontinuity. The approach pairs well with methods that model the gravitational potential directly, such as the PP method. It is important to note that we require a particular level of accuracy in selecting spatial and mass resolutions, especially in the case of self-gravitating fluids [12].

3.2.1 Astrophysical phenomena

In hydrodynamic simulations, whether Eulerian or Lagrangian, it is possible to consider additional gas physics phenomena beyond those previously discussed. These phenomena often involve mechanisms that act on scales smaller than the

simulation resolution and require a so-called sub-grid analysis to be implemented. The main phenomena to include in an astrophysical simulation are the following.

- **Star formation and feedback.** Star formation is a key element in distinguishing among the types of objects that populate the simulation. However, tracking individual gas clouds that lead to star formation phenomena requires high mass resolution. Thus, it is necessary to model the star formation mechanism through prior assumptions. A similar approach is valid for the accretion mechanisms of black holes, which involve regions not resolved either spatially or in terms of mass.

  Additionally, feedback mechanisms, such as those resulting from supernova explosions or AGN activity, originate in regions that are not spatially resolved. These mechanisms must be implemented using analytical or semi-analytical models.

- **Chemical evolution.** Chemical evolution has significant local and global effects, such as on the radiative cooling rate and consequently on star formation. However, because chemical enrichment results from complex processes on small scales, it is necessary to assume an enrichment model.

- **Radiative transfer.** Radiative transfer is a non-local effect and thus it is generally spatially resolved. However, introducing a model for the origin of the radiation field is complicated because it usually comes from unresolved luminous sources. Typically, two types of radiation fields are implemented in simulations: a homogeneous field (such as the CMB) or a field generated by some objects within the simulation.

3.3 Magneticum

In this thesis work, we have performed the AP test using different catalogues extracted from a large hydrodynamic cosmological simulation, called *Magneticum* [22]. The simulation is based on the `P-GADGET3` code [53] that implements the dynamics through a hybrid method between the HT and PM, with the addition of the fluid hydrodynamic with the SPH. The simulation covers a large comoving volume, with periodic boundary conditions, initially filled with an equal number of particles of baryonic matter and CDM. Particle masses satisfy the following

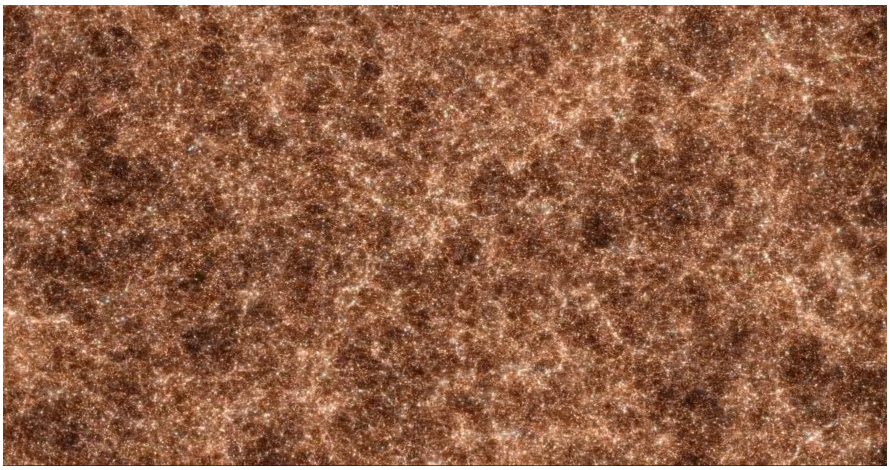

Figure 3.1: The picture shows a visualization of `BOX1` from the *Magneticum Pathfinder* simulation set. The view spans a total size of 1300 Mpc h^{-1}. The gas filling the space between the galaxies is visualized (color-coded according to its temperature from cold/brown to hot/light blue) along with the galaxies and stars forming in the simulation (colored in white).

Volume $[(\mathrm{M\ p\ c})^3 h^{-3}]$	N_{particle}	$m_b\,[M_\odot h^{-1}]$	$m_{dm}\,[M_\odot h^{-1}]$
896^3	2×1526^3	1.3×10^{10}	$2,6 \times 10^9$

Table 3.1: In the table are reported the main information about the `BOX1` of the *Magneticum* simulation.

relation:

$$\frac{m_b}{m_{dm}} = \frac{\Omega_b}{\Omega_{dm}} \quad . \tag{3.9}$$

In this way, are taken into account the different abundance of the two components. There are different realizations of the *Magneticum* simulation, with different mass resolutions and volumes. For this thesis work, we have utilized the catalogues extracted at different redshifts from the realization called `BOX1`. The considered redshifts are $[0.20, 0.52, 0.72, 1.00, 1.50, 2.00]$. In Fig. 3.1 we can see a snapshot at $z \sim 0.2$ of the *Magneticum* simulation. The volume and the mass resolution of $BOX1$ are reported in Table 3.1, while additional details on the simulation can be found in [45].

The cosmological model of the simulation is the ΛCDM with matter density parameter $\Omega_M = 0.272$, baryonic density $\Omega_b = 0.0456$, $\Omega_\Lambda = 1 - \Omega_M$ and $H_0 = 70.4 \quad \mathrm{km\ s^{-1} Mpc^{-1}}$ [36]. This set of cosmological parameters characterized what we will call the "true cosmology" in the AP test.

Radiative cooling, continuous reheating from an ultraviolet background and stellar formation with the associated feedback processes (based on a not-resolved

multiphase model of the interstellar medium) are implemented in the *Magneticum* simulation through analytic prescriptions.

The radiative cooling rate is obtained following the same approach presented in [59], where both the CMB and an ultraviolet and X-ray background from galaxies and quasars are considered [29]. The contribution to the radiative cooling of the tracked elements is pre-computed using the code `CLOUDY` [26], an algorithm for computing photoionization in an optically thin gas in photoionization equilibrium.

In the multiphase model for star formation, the interstellar medium is treated as a two-phase medium where the clouds of cold gas are formed by cooling and are embedded in a hot gas, assuming pressure equilibrium [54]. Groups of baryonic mass elements that are sufficiently massive have an associated rate of star formation. Consequently, star particles are formed with a mass distribution that follows the initial mass function model by Chabrier [15]. It is also assumed that the 10% of the more massive stars explode as a type II supernova. The energy released (10^{51} erg) is assumed to form galactic winds, with mass loss proportional to the star formation rate.

The simulation also includes a treatment for the growth of black holes and *AGN* feedback, also implemented with sub-resolution models. The black holes are sink particles of initial mass 10 $M_{\odot}$, hosted in the more massive object. They can grow in mass through gas accretion following the Bondi-Hoyle-Lyttleton approximation [14] [13] [32]:

$$\dot{M}_{BH} \sim \frac{4\pi G_N^2 M_{BH}^2 \rho}{(c_s^2 + v^2)^{3/2}}, \tag{3.10}$$

where ρ and c_s are the density and the sound speed of the interstellar medium around the black hole, while v is the black hole's speed with respect to the surrounding gas. The self-gravitating haloes of CDm are identified with an algorithm called friends-of-friends (`FOF`) [33], [50]. This algorithm identifies virialized groups of at least 32 CDM particles, separated by a distance less than 0.16 $\bar{l}$, where $\bar{l}$ is the average separation between the particles [21]. At this point, it is possible to identify overdense and self-gravitating sub-structures within each CDM halo. The identification of such structures is implemented through a modified version of the `SUBFIND` algorithm, which also considers the baryonic matter particles [21]. Both these steps are performed at each time snapshot of the simulation.

Once the dark matter halo and the sub-structures they contain are identified, each structure is associated with physical properties derived from the fluid dynamics of the baryonic mass particles that compose it. Based on these properties,

it is possible to determine the type of object each structure represents, whether it be a galaxy, an AGN, or a cluster of galaxies.

Structures with a sufficient stellar formation rate are associated with particle stars and identified as galaxies. Each galaxy is assigned a stellar mass, a star formation rate, and an absolute magnitude in different bands, in addition to their velocity and position. This allows for the sub-sampling of the galactic population to analyse the characteristics of specific classes of objects.

The AGNs are a particular sub-sample of galaxies. The more massive galaxies (total stellar mass of roughly $10^{10}\ M_{\odot}h^{-1}$) host a black hole with an initial mass of $10^{5}\ M_{\odot}H^{-1}$, that can grow through gas accretion or merging. From the accretion rate (normalized to the Eddington accretion rate), the emitted bolometric luminosity is computed as follows:

$$L_{bol} = 0.1\dot{M}_{BH}c^2 \quad . \tag{3.11}$$

For a more complete description of the *AGN* sample in the *Magneticum* simulation see [30].

Mass elements of both dark and baryonic matter contained in the virialized halo, identified through the use of the `FOF` algorithm, are recognized as galaxy clusters. The cluster positions are computed from the central particle positions of the identified group, while the cluster velocities are the average velocities of the systems. Moreover, for each cluster, measurements of the mass and temperature within a certain virial radius R_{500} are available. This radius is defined as the scale at which the density is 500 times greater than the critical density of the universe. Finally, an estimation of the X-ray luminosity given by the bremsstrahlung emission is also provided for each cluster.

The potential advantage of performing the AP test on a catalogue of galaxy clusters is the greater ease with which it is possible to model the dynamical distortions.

Table 3.2 reports the main characteristics of the used catalogues. Specifically for each tracer, the number of objects of the catalogues at different redshifts are reported. For galaxies, the average value of the stellar mass ($\overline{M}_{\odot}$), the absolute magnitude in the G band ($\overline{G}$), and the star formation rate ($\overline{\mathrm{SFR}}$) are reported. For the AGN the average values of the black hole mass ($\overline{M}_{BH}$), of the bolometric luminosity ($\overline{L}_{bol}$), and of the accretion rate normalized to the Eddington accretion

	Galaxies			
	$N_{obj}\,[10^6]$	$\overline{M}_{\odot}\,[10^{10}M_{\odot}h^{-1}]$	$\overline{G}$	$\overline{\mathrm{SFR}}\,[M_{\odot}h^{-1}yr^{-1}]$
$z = 0.20$	3.24	8.9	-21.48	16.24
$z = 0.52$	2.87	7.6	-21.19	21.72
$z = 0.72$	2.60	6.8	-21.04	25.78
$z = 1.00$	2.18	5.7	-20.87	32.77
$z = 1.50$	1.64	4.4	-20.57	42.35
$z = 2.00$	1.12	3.3	-20.27	48.33
	AGNs			
	$N_{obj}\,[10^5]$	$\overline{M}_{BH}\,[10^8M_{\odot}h^{-1}]$	$\overline{L}_{\mathrm{bol}}\,[10^{45}\mathrm{ergs}^{-1}]$	$\overline{f}$
$z = 0.20$	9.5	6.0	0.59	0.03
$z = 0.52$	6.9	6.7	1.13	0.05
$z = 0.72$	5.6	6.9	1.26	0.06
$z = 1.00$	3.6	8.2	2.80	0.10
$z = 1.50$	2.0	8.9	9.26	0.21
$z = 2.00$	0.9	8.1	16.34	0.25
	Galaxy clusters			
	$N_{obj}\,[10^5]$	$\overline{M}_{500}\,[10^{12}M_{\odot}h^{-1}]$	$\overline{T}_{500}[\mathrm{Kev}]$	$\overline{L}_{500}\,[10^{42}\mathrm{ergs}^{-1}]$
$z = 0.20$	5.3	8.3	0.239	6.11
$z = 0.52$	4.8	7.2	0.240	7.76
$z = 0.72$	4.3	6.5	0.227	9.52
$z = 1.00$	3.5	5.5	0.226	10.80
$z = 1.50$	2.4	4.4	0.203	13.14
$z = 2.00$	1.4	3.4	0.170	14.33

Table 3.2: The average characteristics of the analysed catalogues, for the different tracers and redshifts.

rate are reported. The last reported parameter is defined as follows:

$$f \equiv \overline{M}_{BH}/\overline{M}_{edd}, \tag{3.12}$$

where $\overline{M}_{BH}$ is the average mass accretion rate of the black hole and $\overline{M}_{edd}$ is the Eddington rate at which the emitted luminosity produces enough radiation pressure to balance the gravitational attraction, thereby halting stop the accretion onto the black hole. Finally, for the galaxy clusters the average value of mass, temperature, and luminosity in the X-ray band at virial radius ($\overline{M}_{500}, \overline{T}_{500}, \overline{L}_{500}$) are reported.

Chapter 4

The Alcock-Paczyński test

Until now, we have discussed the 2PCF as dependent solely on the distance between two objects, without considering the directions with respect to the line of sight along which they are separated. The most direct measurement of the galaxy density field comes from galaxy redshift surveys, where both the angular positions and redshifts (a measure of radial distance) are recorded. This provides a 3D position for each galaxy, enabling the measurement of their three-dimensional statistics, such as the 2PCF. What we have just said for galaxies is also valid for other generic astrophysical tracers.

However, interpreting the 2PCF measured from redshift surveys presents several challenges. First, as noted in Section 2.3.1, there is the issue of bias: the clustering of tracers differs from that of matter. Second, tracer redshifts include not only the cosmological redshift, which depends on their distance, but also a Doppler shift due to their peculiar velocities. A tracer's redshift would indicate its distance accurately only if the tracer was stationary relative to the expanding background space. Since instead tracers are not stationary, their peculiar velocities affect the observed redshift through the Doppler effect. Consequently, an accurate redshift measurement does not directly translate into an unambiguous measurement of radial distance. Additionally, tracer velocities are correlated with matter density, leading to modifications in galaxy statistics known as *redshift-space distortions* (RSDs). A third significant issue is the impact of incorrect assumptions about the cosmological model used to compute distances, the so-called *geometric distortions*. Through the AP test, we will explore how this issue can be leveraged as a resource to infer constraints on cosmological parameters.

To study these effects, it is more effective to use the bidimensional form of the 2PCF, breaking $\xi(r)$ down into components along the directions perpendicular

and parallel to the line of sight. We therefore introduce $\xi_{2D}(r_\perp, r_{||})$, where $r_\perp$ and $r_{||}$ are, respectively, the separations of two objects perpendicular and parallel to the line of sight.

Given the CP, there are no preferred directions in the measurement of $\xi(r)$, so the signal must be isotropic. Based on this principle and in the absence of distortions, the bidimensional correlation function can be simply written as:

$$\xi_{2D}(r_\perp, r_{||}) = \xi\left(\sqrt{r_\perp^2 + r_{||}^2}\right) \quad . \tag{4.1}$$

4.1 Distortion of the bidimensional 2PCF

4.1.1 The redshift-space distortions

The Hubble-Lemaître law, Eq. (1.15), describes a linear relationship between the speed of recession of astronomical objects (and consequently their redshift) and their positions. However, as previously mentioned, the proper motions of these objects generate a Doppler effect that is added to the cosmological redshift as follows:

$$z_{obs} = z_H + \frac{v_{||}}{c}(1 + z_H) \quad , \tag{4.2}$$

where z_H is the redshift contribution from the Hubble flow, with an additional term accounting for the object's velocity along the line of sight.

One possible way to address RSD is to start from the continuity equation for matter at late times ($z \lesssim 10$), assuming small distortions in the true positions of objects and operating in the linear regime. Through a series of steps and assumptions [20], it is possible to derive an expression for RSD in terms of density contrast as follows:

$$\delta_{g,RSD}(\mathbf{k}) = [b + f\mu_k^2]\delta(\mathbf{k}) \quad . \tag{4.3}$$

In Eq. 4.3, μ_k is defined as $\hat{\mathbf{e}}_z \cdot \hat{\mathbf{k}}$, i.e. the cosine of the angle between the line of sight and the wavevector $\hat{\mathbf{k}}$ of the Fourier transform of the density contrast. This equation also introduces the growth factor of density fluctuations, f, and the tracer bias, b. Firstly, since $f\mu_k^2 \geq 0$, the apparent overdensity in redshift space is larger than in real space, where it would be simply $b \cdot \delta_m(\mathbf{k})$. This can be noticed from the left side of Fig. (4.1): if equal-density contours are squashed, then the galaxies are moved close together and hence their density is increased

around an overdensity. The opposite happens around underdensities. Both effects act to increase the apparent galaxy density contrast. The second notable feature of Eq. (4.3) is that only perturbations with wavevectors parallel to the line of sight are enhanced. A perturbation with **k** perpendicular to the line of sight, maintaining a constant density along the line of sight, experiences no RSD. The physical explanation of this effect is simply given by the fact that the objects are falling towards the overdense region. The objects closest to us are moving toward the center of the overdense region and hence away from us, so they appear farther from us than they actually are. Similarly, objects on the "other side" of the perturbation are moving towards us, so they appear closer to us than actually are. The overall effect is to induce an apparent anisotropy in an otherwise circular overdensity, also referred to as the Kaiser effect [34].

As we move to smaller, nonlinear scales, the nature of the RSD changes. The velocity is dominated by the object's random motion within matter overdensities. This introduces a significant Doppler effect along the line of sight that perturbs the measurement in a random manner, similar to the impact of uncertainties in the measurement of the cosmological redshift. These effects are also called "fingers of God" and on the right side of Fig. (4.1) we can see how they modify the bidimensional 2PCF.

Both of these effects, on large and small scales, more intensely affect smaller objects like galaxies, which exhibit stronger proper motions and more intense coherent motions larger structures. In principle, it is possible to model and remove the cosmological redshift contamination produced by the velocity along the line of sight of the considered objects (we will return to this in the next chapter). In Fig. (4.2), we can see how the RSDs affect the image of the galaxies' distribution, with the "fingers of God" effect particularly visible on the left side of the figure. From now on, we will refer to *redshift space* $(s_\perp, s_{||})$ as the space in which the measured redshifts are used to compute comoving distances and thus where the 2PCF shows the RSD. Conversely, we will refer to *real space* $(r_\perp, r_{||})$ as the space in which the true comoving distances are used.

4.1.2 Geometric distortions

Once we have corrected for the RSD, we could expect the bidimensional 2PCF to be perfectly circular in real space. However, this is only true if the cosmological parameters used to measure distances are correct. Otherwise, geometric distortions occur, modifying the shape of the isocorrelation curves in both real

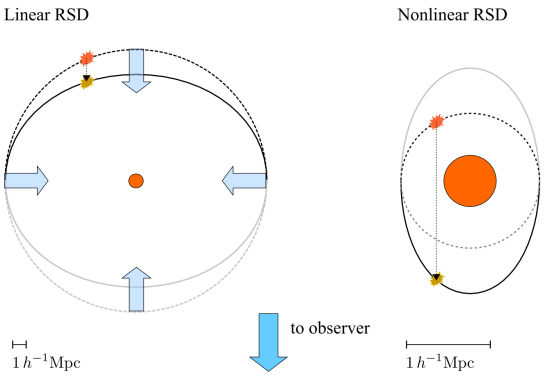

Figure 4.1: RSD, in the linear/large-scale (left) and nonlinear/small-scale variants (right), both considering the case of central overdensity denoted by the filled circle. The observer is assumed to be far away below the figure so that the line of sight direction $\hat{\mathbf{n}}$ is vertical. In each case, a contour of constant density (dashed lines), which is circular in real space, is distorted in redshift space (solid lines) so that it looks asymmetric. Wide arrows indicate the direction of the velocity flow, while arrows with dashed lines indicate the displacement due to the line-of-sight velocity. In the nonlinear case, as the absolute scales are smaller, a point on the "far side" (top) of the overdensity is mapped onto a point on the opposite side. Imagine taken from Chapter 11 of [20].

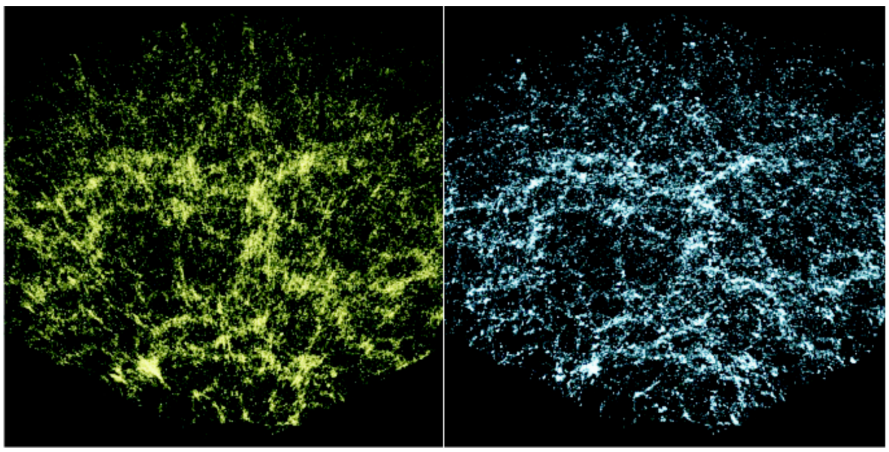

Figure 4.2: Galaxies distribution from the Sloan Digital Sky Survey into the redshift space on the left side and in the real space on the right side. Image taken from [56].

and redshift space.

Suppose we have successfully modeled and completely removed the RSD, and we want to measure the distance between two objects in the plane $(r_\perp, r_{||})$. To measure their separation, we should start from two different observables: the difference in redshift, Δz, of the two objects for the separation along the line of sight, and the angular separation, $\Delta\Theta$, for the perpendicular component to the line of sight. We can then transform these observables into the separations we are interested in and obtain the following:

$$r_{||} = \frac{c}{H(z)}\Delta z, \quad r_\perp = (1+z)D_A(z)\Delta\Theta \quad , \tag{4.4}$$

where D_A is the angular diameter distance defined as:

$$D_A(z) = \frac{1}{1+z}\int_0^z \frac{dz'}{H(z')} \quad . \tag{4.5}$$

We can immediately notice how the two components of the distance depend differently on the Hubble constant (and consequently on the assumed cosmological model). Modifying the cosmological model introduces different distortions in the lengths along the two directions. In particular, given two cosmological models marked by subscripts 1 and 2, we have the following:

$$r_{||1} = \frac{H_2(z)}{H_1(z)} r_{||2} \quad , \tag{4.6}$$

and

$$r_{\perp 1} = \frac{D_{A,1}(z)}{D_{A,2}(z)} r_{\perp 2} \quad . \tag{4.7}$$

All this also happens in redshift space, where these distortions are added to the previously seen RSD. These distortions are also called Alcock-Paczyński (AP) distortions and are directly connected to the geometry of the universe, enabling us to perform a test for the determination of cosmological parameters.

4.2 The Alcock-Paczyński test on the bidimentional 2PCF

Let us suppose we are working in real space. The isotropy of the spacetime ensures that the isocorrelation curves are perfectly circular if we have assumed

the correct cosmology. As mentioned earlier, there is no reason to assume a different probability of finding two objects separated by a distance r along the line of sight compared to two objects separated by r perpendicular to the line of sight. However, if we assume incorrect cosmological parameters to measure the distances, we introduce the previously discussed geometric distortions. The space is deformed differently along the two directions, causing the 2PCF to no longer be circular.

The isocorrelation curve can be thought of as a standard circle, similar to how Baryonic Acoustic Oscillations (BAO) and supernovae are considered standard rulers and candles, respectively. This serves as a test to determine cosmological parameters. With the AP test, it is possible to identify the correct set of cosmological parameters, as these will be the only ones that eliminate the geometric distortions. Any other choice will modify $r_{||}$ and $r_{\perp}$ when transforming from Δz and $\Delta\Theta$ in a different way from one another.

The test can also be applied in redshift space, where it is a bit more complex. The AP test can be performed on the bidimensional 2PCF by measuring the 2PCF using different cosmologies and identifying the one that does not exhibit (or exhibits to a lesser extent) the geometrical distortions.

So far, to describe the geometrical distortions, we have only considered the different dependency on $H(z)$ in $r_{||}$ and $r_{\perp}$. Now, let us assume a flat universe where $\Omega_{0,tot} = 1$. Neglecting the radiation contribution and assuming $w_\Lambda = -1$, we can write $H(z)$, making its dependency on $\Omega_{0,M}$ more explicit, as follows:

$$H(z) = H_0(1+z)[\Omega_{0,M}(1+z) + (1-\Omega_{0,M})(1+z)^{-2}]^{1/2} \quad . \tag{4.8}$$

Thus, in this case, assuming a wrong value of the matter density parameter (assuming $\Omega_\Lambda = 1 - \Omega_{0,M}$) introduces geometric distortions. We can therefore measure the distances and the isocorrelation curves as a function of the only parameter $\Omega_{0,M}$ and observe when the distortions are null.

It is interesting to note that the effect of geometric distortions depends not only on the assumed cosmological model but also on the observed redshift. In particular, an increase in geometric distortions is observed at higher redshifts [41]. However, at high redshifts, dynamical distortions also become more significant, making geometric distortions more visible around $z \sim 1$ [11].

In this thesis work, we have performed the AP test on catalogues produced from the Magneticum cosmological hydrodynamic simulations to assess its efficiency. In a simulation, the cosmological parameters are fixed and known, so the

test should ideally identify the parameters with which the simulation was constructed. Therefore, the results provide an estimation of the effectiveness of the test and/or the method chosen to implement it.

4.3 The Alcock-Paczyńsky test implementation

There are at least two possible methods to implement the AP test on the 2PCF of an observed (or simulated) catalougue. In the following sections, we describe them in detail, illustrating their main advantages and weaknesses.

4.3.1 The *standard* method

A commonly used method for performing the AP test involves measuring the 2PCF using a single assumed cosmology to convert redshifts into comoving distances. Analytic models of the 2PCF, including RSD, are then generated for various test cosmologies. Each model also incorporates the geometric distortions specific to its test cosmology with respect to the assumed cosmology. The modelled correlation function aligns with the measured one at the assumed cosmology only when the test cosmology matches the true cosmology, correctly accounting for the geometric distortions.

The main issue with this method is that it requires assuming an accurate model, meaning it has to describe the non-linearities, tracer bias and RSD sufficiently accurately. Indeed to construct such a model, it is necessary to compute a correlation function from the Fourier transform of the non-linear dark matter correlation function, and assume a model for the bias, which must account for the specific tracers considered. Moreover, an accurate modelling of RSD is crucial not to introduce biases. On the other hand, the most significant advantage of this approach is that it only requires measuring the correlation function and the covariance matrix at the assumed cosmology. This fact allows a considerable saving of computational time compared to other methods. In Fig. (4.3) we have summarized what was said through an explanatory graph.

4.3.2 The *alternative* method

An alternative method, first introduced in [44] and also utilized in [27] and [25], is as follows. We measure the correlation function of a catalogue of objects for a set of different cosmologies and then produce a model for each test cosmology. In

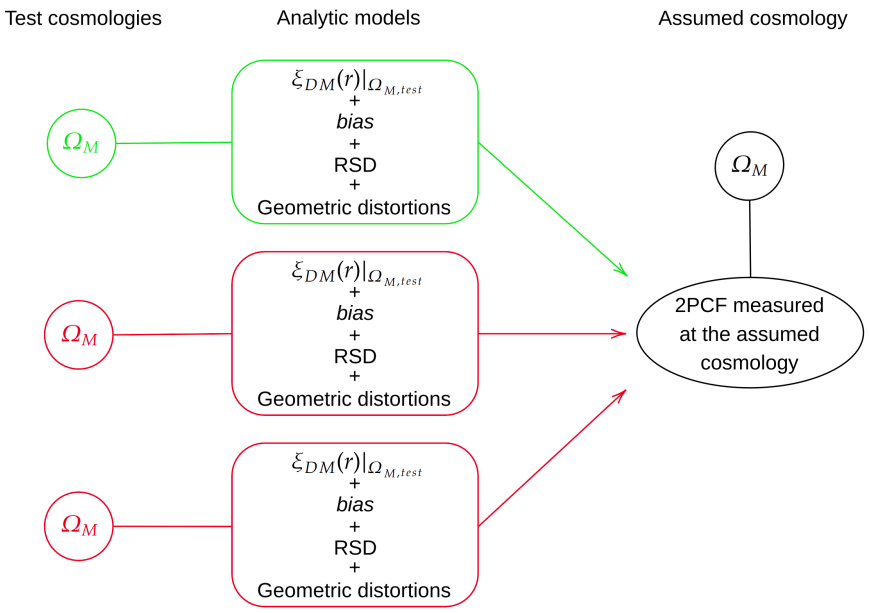

Figure 4.3: Schematic representation of the standard method to implement the AP test.

these models, we include the RSD but not the geometric distortions. The models are constructed starting from the Fourier transform of the dark matter 2PCF and assuming a linear bias. To model the RSDs, we used a semi-analytic approach, fitting the measure to minimize the differences between the model and the measured 2PCF. Three parameters were allowed to vary freely, one of which is the bias. The details of this fitting process will be discussed in the next chapter. The agreement between the measurement and the model is better when the geometric distortions of the bidimensional 2PCF are low, which occurs when the cosmological parameters of the test cosmology are close to the real ones. In fact, since in this approach the model does not include the geometric distortions, only when considering the correct cosmology do we achieve consistency with the measured correlation function—when, by definition, the geometric distortions are null. For all other cosmologies, the best-fit model does not accurately describe the data, as the data have non-zero geometric distortions.

This method does not require an accurate modelling of 2PCF, as is needed in the standard method. Moreover, the model construction can start from the deprojected procedure [47] or the correlation function of dark matter with the bias left as a free parameter of the fit. In the case of testing the method with a simulated catalogue, it is also possible to start simply from the correlation function measured in real space without assuming a bias.

On the other hand, the principal problem of this method is the computational

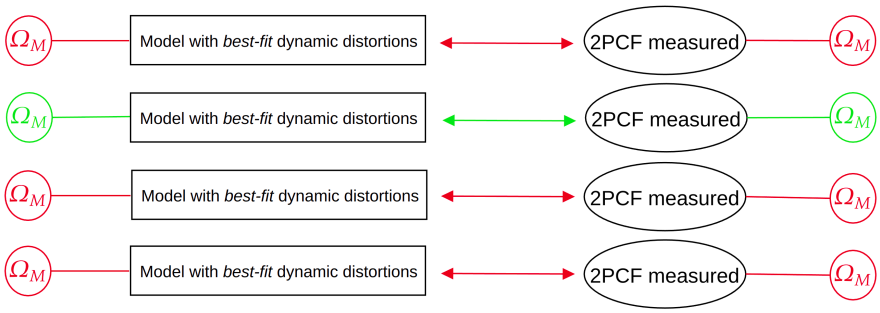

Figure 4.4: Schematic representation of the alternative method to implement the AP test.

time, as it requires measuring the 2PCF for each test cosmology. In Fig. (4.4), we have summarized the main steps of the method similarly to what we have done for the standard method.

The main goal of this thesis work, is to validate this alternative method with simulations. In particular, for the models, we started from the correlation function of dark matter (obtained using a Boltzmann solver) and left the bias as a free parameter of the fit. We chose this approach because it can be also applied to a real catalogue and is simpler to implement compared to the deprojected method. A detailed description of the code implemented to perform the AP test in this work is provided in the next chapter.

Chapter 5

The algorithms

In this chapter, we will provide a detailed explanation of how the AP test has been implemented. As previously mentioned, this thesis work is based on the method proposed in [44] and on the thesis works inspired by it, [25] and [27]. We chose to compute the 2PCF for each test cosmology and then create a model that does not account for the geometric distortions described in Section 4.1.2. This approach requires some precautions, particularly during the construction of random catalogues needed for the computation of ξ_{2D} using the LS estimator defined in Section 2.3.2.

The code used for the AP test implementation extensively utilizes the *free software* libraries `CosmoBolognaLib` [1]. These libraries offer a comprehensive set, of continuously updated `C++/Phyton` tools, serving as a robust framework for cosmological research. The primary goal of the `CosmoBolognaLib` is to create a unified workspace for addressing various computational cosmological problems, from handling large data catalogues to measuring and modelling second-order and higher-order statistics of the density field. For a detailed explanation of the main classes and methods in the library, refer to [43].

5.1 Outline of the algorithms

The method used in this work to perform the AP test can be broken down into several key steps, which will be analyzed in the following sections.

The analysis begins with the acquisition of the simulated object's comoving positions, which have to be converted into angular coordinates, R.A. (right ascensions) and Dec. (declinations), along with the redshifts. The redshifts can either be the cosmological ones or they can include the contribution from the object's

proper motion (in redshift space). As described in Chapter 4.1.1, in the former case we are in real space, while in the latter we are in redshift space. The real space analysis is only possible with simulations. We consider it here for testing purpose. The redshift space analysis instead get closer to what we can achieve with real data. The primary focus of this analysis will be on varying only the value of Ω_M in order to reveal geometric distortions. This parameter has the most significant impact on the observed effects. However, future analyses could be extended to include other cosmological parameters.

The following steps are the sequential operations performed, varying the matter density parameter for each test cosmology:

- Transformation of the angular coordinates back to comoving coordinates;
- Construction of the random catalogue;
- Pair counting and estimation of the 2PCF and associated covariance matrix;
- Best-fit of the 2PCF redshift-space model parameters;
- Computation of a metric function to quantify the model accuracy.

Specifically, for each test cosmology, we measure the 2PCF and obtain the best-fit model parameters by maximizing a likelihood function $\mathcal{L}$, defined as follows:

$$\mathcal{L}(\beta, \sigma_{12}; \Omega_M) \propto \exp\left\{ -\frac{\left[\xi_{\text{measured}}(\Omega_M) - \xi_{\text{model}}(\beta, \sigma_{12}; \Omega_M)\right]^2}{\delta\xi^2_{\text{measured}}} \right\} \quad , \tag{5.1}$$

where β and σ_{12} are the model parameters considered in this work. To maximize the likelihood function, we simply minimize its exponent, which is equivalent to minimizing the following function:

$$\chi^2(\beta, \sigma_{12}; \Omega_M) = \frac{\left[\xi_{\text{measured}}(\Omega_M) - \xi_{\text{model}}(\beta, \sigma_{12}; \Omega_M)\right]^2}{\delta\xi^2_{\text{measured}}} \quad . \tag{5.2}$$

The best-fit parameters characterize the model that best describes the measured 2PCF for each test cosmology, despite any geometric distortions present. Now, we define a function as follows:

$$F(\Omega_M) \equiv min\Big\{\chi^2(\beta, \sigma_{12})\Big\}_{\Omega_M, test} = \chi^2(b, \beta, \sigma_{12})_{\text{best-fit}}\Big|_{\Omega_M, test} \quad , \tag{5.3}$$

This function represents the set of all chi-squared minima at different test cosmologies. If each minimum corresponds to the best model (i.e., the one with the best-fit parameters) at a given test cosmology, then the minimum of $F(\Omega_M)$ represents the model that most accurately describes the measured 2PCF across all cosmologies. Since the models account only for the dynamical distortions, the minimum of $F(\Omega_M)$ identifies the test cosmology in which the geometric distortions in the measurement of the bidimensional 2PCF are null.

Now, let us return to the initial stages of our method to gain a clearer understanding of each step in the algorithm.

5.2 Transformation of the angular coordinates back to comoving coordinates

To measure the correlation function $\xi(r_\perp, r_{||})$, it is necessary to count the pairs of objects in the catalogue asa function of comoving distances from each other. When we convert the angular coordinates of each object into comoving coordinates, assuming a test cosmology geometric distortions can be introduced if the test cosmology differs from the true one:

$$(\text{R.A.}, \text{Dec}, z) \longrightarrow (X, Y, Z) \quad . \tag{5.4}$$

Specifically, each object's redshift is converted into a comoving distance, d_C, according to the test cosmology. Then the so-called pseudo-equatorial coordinates (d_C, R.A., Dec) are converted into Cartesian coordinates:

$$\begin{cases} X = d_C \cos(\text{Dec}) \cos(\text{R.A.}) \\ Y = d_C \cos(\text{Dec}) \sin(\text{R.A.}) \\ Z = d_C \sin(\text{Dec}) \quad . \end{cases} \tag{5.5}$$

Assuming an incorrect cosmology distorts all distances and, consequently, the shape of the catalogue. It is important to note that these distortions must be taken into account when constructing the random catalogue.

5.3 Construction of the random catalogue

To measure the 2PCF at each test cosmology, we need to construct a random catalogue that matches the geometry of the catalogue. The measurement of the 2PCF is more accurate with a larger N_{ran}/N_{obj} ratio, where N_{ran} is the number of objects in the random catalogue and N_{obj} the number of objects in the analised catalogue. However, given that the computational time for the AP test considered in this work is primarily dominated by the time needed for pair counting, we have chosen to use random catalogues with $N_{ran} = 3 \times N_{obj}$.

As previously mentioned, modifying the test cosmology changes the shape of the catalogue. Therefore, it is necessary to deform the random catalogue in the same way. This is achieved using a specific function of the `CosmoBolognaLib`. A random catalogue constructed assuming the real cosmology, and thus cubic in this case, becomes warped when assuming a wrong test cosmology for coordinate transformation. To ensure that the geometric distortions are consistent in both the real and random catalogues the same coordinate transformations are performed on the random catalogue.

This step is crucial for the correct computation of the 2PCF. Indeed, if the geometric selection of the random is not accurate the mixed term of the Landy-Szalay estimator introduces a spurious effect that alters the form of the 2PCF.

5.4 Pair counting and estimation of the 2PCF and associated covariance matrix

Once we have constructed both the catalogue and its associated random catalogue in comoving coordinates, in a specific test cosmology, we can proceed by measuring the pair counts. As discussed in Section 2.3.2, we have chosen the LS estimator for measuring 2PCF. This estimator requires the computation of $DD(r)$, $RR(r)$, and $DR(r)$ pairs, where $DD(r)$ represents the pairs of objects from the simulated catalogue, $RR(r)$ is the pairs from the random catalogue, and $DR(r)$ represents the mixed pairs. This operation is the most time-consuming part of the entire process: the computational time for the simplest possible algorithm that counts pairs in a given catalogue of objects is proportional to N^2, where N is the number of objects in the catalogue. However, as discussed in Ch.3, there are various

methods to reduce the time needed to count object pairs [1].

In particular, the method used for pair computation in this work is called `CHAIN_MESH`, which can significantly reduce computational time under certain conditions. Specifically, the catalogue is divided into a grid of arbitrary fineness, with the indexes of the objects in each cell recorded. A maximum distance, r_{max}, is chosen within which pairs are counted. For each object in a cell C_i, only the objects in cells C_j such that $d(C_i, C_j) \lesssim r_{max}$, where $d(C_i, C_j)$ is the distance between the two cells, are considered. This method excludes all objects separated by distances greater than the maximum separation considered, thereby significantly reducing the computation time required [2]. Similarly, a minimum distance, r_{min}, can be defined to exclude all objects contained in cells where $d(C_i, C_j) \lesssim r_{min}$. This exclusion further reduces computation time.

In this thesis, the maximum separation between objects is set to 50 Mpc h^{-1}, and the minimum separation is set to 3 Mpc h^{-1}. These limits help us to reduce the computational time, and to avoid those scales where the correlation function is difficult to model due to the strong influence of the fingers of God effect, or due to large measurement uncertainties caused by cosmic variance. Once all pairs are identified, the 2PCF can be computed using the LS estimator (Eq. 2.24).

5.4.1 Error on the 2PCF measure

The errors on the 2PCF are assumed to be Poissonian, thus the propagated errors on the LS estimator can be computed as follows:

$$\delta\xi = \sqrt{\left(N_1 \frac{\sqrt{\mathrm{DD}}}{\mathrm{RR}}\right)^2 + \left(N_2 \frac{\sqrt{\mathrm{DR}}}{\mathrm{RR}}\right)^2 + \left(\frac{N_1 \mathrm{DD} - N_2 \mathrm{DR}}{\mathrm{RR}^{1.5}}\right)^2} \quad , \tag{5.6}$$

where

$$N_1 = \frac{n_R(n_R - 1)}{n_D(n_D - 1)} \quad , \quad N_2 = \frac{n_R(n_R - 1)}{n_R n_D} \quad . \tag{5.7}$$

DD, RR and DR are the un-normalised numbers of data-data, random-random and data-random pairs, respectively. n_D and n_R are the total number of data and random objects.

[1] The problem of pair counting for measuring the 2PCF is numerically identical to calculating the mutual gravitational attraction of a set of objects.

[2] This approach is used in the `CosmoBolognaLib` libraries into function `count_pairs` of the class `TwoPointCorrelation`.

5.5 Best-fit of the 2PCF redshift-space model parameters

The next step is to compute a model for the 2PCF of the tracers starting from the dark matter 2PCF, ξ_{DM}, and including the tracer bias and dynamic distortions. In this analysis, ξ_{DM} is obtained by applying the Fourier inverse transform to the matter power spectrum, which is provided by the code `CAMB` (Code for Anisotropies in the Microwave Background [2]) which can be used within the `CosmoBolognaLib`.

5.5.1 Dynamic distortions modelling

In this work we will use the so-called dispersion model to describe the dynamic distortions parameters, β and σ_{12}. At sufficiently large scales, where the influence of the fingers of God effect is negligible, the correlation function can be expressed as a function of the first three even multiples, as follows [47]:

$$\xi_{lin}(s_\perp, s_{||}) = \xi_0(s)P_0(\mu) + \xi_2(s)P_2(\mu) + \xi_4(s)P_4(\mu) \quad , \tag{5.8}$$

where $P_i(\mu)$ are the Legendre polynomials of order i, and $s \equiv \sqrt{s_\perp^2 + s_{||}^2}$ and $\mu \equiv \frac{s_{||}}{s}$.

Specifically, the multipoles of ξ are given by:

$$\xi_0(s) = \left(1 + \frac{2}{3}\beta + \frac{1}{5}\beta^2\right) b^2 \xi_{DM}(r) \quad , \tag{5.9}$$

$$\xi_2(s) = \left(\frac{4}{5}\beta + \frac{4}{7}\beta^2\right) \left[b^2\xi_{DM}(r) - b^2\overline{\xi}_{DM}(r)\right] \quad , \tag{5.10}$$

$$\xi_4(s) = \frac{8}{35}\beta^2 \left[b^2\xi_{DM}(r) + \frac{5}{2}b^2\overline{\xi}_{DM}(r) - \frac{7}{2}\overline{\overline{\xi}}_{DM}(r)\right] \quad , \tag{5.11}$$

where

$$\overline{\xi}_{DM}(r) \equiv \frac{3}{r^3}\int_0^r \xi_{DM}(r')r'^2 dr' \quad , \tag{5.12}$$

$$\overline{\overline{\xi}}_{DM}(r) \equiv \frac{5}{r^5}\int_0^r \xi_{DM}(r')r'^4 dr' \quad . \tag{5.13}$$

The parameter β is defined as:

$$\beta = \frac{f(z)}{b(z)} \quad , \tag{5.14}$$

where b is the linear bias of the tracers and $f(z)$ is the linear growth rate.

At small scales, specifically when r is less than about 5 Mpc h^{-1} for galaxies [45], it is necessary to account for the fingers of God effect in the model construction. The model in Eq. (5.8) can be convolved with the velocity distribution of the objects, $f(v)$, as follows:

$$\xi(s_\perp, s_{||}) = \int_{-\infty}^{\infty} f(v)\xi_{lin}\left[s_\perp, s_{||} - \frac{v(1+z)}{H(z)}\right] dv \quad . \tag{5.15}$$

In this thesis work, we considered the following velocity distribution function:

$$f(v) = \frac{1}{\sigma_{12}\sqrt{2}} \exp\left(-\frac{\sqrt{2}|v|}{\sigma_{12}}\right) \quad . \tag{5.16}$$

The parameter σ_{12} represents the random velocity dispersion of the object pairs, which causes the fingers of God effect.

5.5.2 Another perspective in the construction of the model: the deprojection procedure

As discussed, we use the theoretical dark matter correlation function to construct the model for the tracer 2PCF. There are in fact two other possible approaches. One is to use the tracer 2PCF measured directly in real space, at the real cosmology. This is feasible only when analysing simulated catalogues, where the peculiar velocities of the objects and their bias are known a prior.

On the other hand, in real observations, dynamical distortions always affect the data, but it is still possible to measure the correlation function in real space using the so-called *deprojection procedure*. The approach involves a two-step projection procedure. First, the observed redshift-space bidimensional correlation function (the only one available in real observations) is projected along $s_{||}$:

$$w_\perp(r_\perp) = 2\int_0^\infty ds'\xi(s_\perp, s'_{||}) = 2\int_{r_\perp}^\infty \frac{y\xi(y)dy}{\sqrt{y^2 - r_\perp^2}} \quad . \tag{5.17}$$

Then, the real-space correlation function can be estimated from the Abel integral [52]:

$$\xi(r) = -\frac{1}{r_\perp}\int_r^\infty dr'_\perp \frac{dw_{r_\perp}/dr'_\perp}{\sqrt{{r'_\perp}^2 - r^2}} dr'_\perp \quad . \tag{5.18}$$

It is important to note that in this way, we obtain the tracers' correlation function directly, without having to introduce an additional dependency on the bias in the model.

5.5.3 Modelling the dynamic distortions

Once the model for the 2PCF is constructed, we can explore the parameter space to find the best-fit values for b, β, and σ_{12} for a given test cosmology. We do this by minimizing the following chi-squared function:

$$\chi^2(b,\beta,\sigma_{12};\Omega_M) = \sum_{s_\perp,s_{||}} \frac{[\xi(s_\perp,s_{||}) - \xi_{model}(s_\perp,s_{||};b,\beta,\sigma_{12})]^2}{(\delta\xi)^2}\bigg|_{\Omega_M} \quad , \tag{5.19}$$

where $\delta\xi$ is the error on the measured correlation function, computed as described in Section 5.4. From the minimum of the χ^2 function, we obtain the values $(b,\beta,\sigma_{12})_{\text{best-fit}}$, which are the best parameters to describe the dynamical distortions of the 2PCF at a given test cosmology.

In real space, by definition, there are no dynamical distortions. This can be obtained by setting in the dispersion model $\beta = 0$ and avoiding the convolution given by Eq. (5.15). Constructing a model in real space following this approach is equivalent to having $\xi_{model}(r_\perp, r_{||}) = b^2\xi_{DM}(\sqrt{r_\perp^2 + r_{||}^2})$.

5.6 Computation of a metric function to quantify the model accuracy

After obtaining the best-fit parameters, we can investigate in which test cosmology the effect of geometric distortions is weaker. The cosmology with the smallest value of χ^2, with β and σ_{12} fixed at their best-fit values, is the one that best matches the measured data.

It is important to note that the function χ^2 used in this method is not a standard χ^2 function because both the measured and modeled 2PCF depend on

the test cosmologies. Therefore, it is not possible to associate a confidence region to the Ω_M constraints by simply considering differences in the reduced χ^2 values.

Instead, to complete the analysis, we search for the minimum of the following function:

$$F_{red}(\Omega_M) = \frac{\chi^2(b, \beta, \sigma_{12})_{\text{best-fit}}\Big|_{\Omega_M, test}}{N_p} \quad , \tag{5.20}$$

where N_p is the number of bins in the chosen fitting range. Using Eq. (5.3) or Eq. (5.20) as a metric for model accuracy yields the same results. We opted for the latter due to its more intuitive scale.

Despite potential inaccuracies in modeling the dynamical distortions and the partial degeneracy between dynamic and geometric distortions, it is still possible to identify the correct value of Ω_M, as we will show in the next Chapter.

Chapter 6

The results

In this final chapter, we present the main results obtained in this thesis work. These results are derived by performing the AP test on the simulated catalogues described in Chapter 3, using the algorithms outlined in Chapter 5. As we will show, the precision of the method depends on the number of objects contained in the catalogues. We remind the reader that the true value of the Ω_M parameter, that is the Ω_M value of the *Magneticum* simulation from which the catalogues were extracted, is $\Omega_M = 0.272$. Therefore, we expect to find the minimum of the $F_{red}(\Omega_M)$ function corresponding to this value.

6.1 Galaxy catalogues

The AP test was firstly applied to galaxy catalogues from `BOX1` of the *Magneticum* simulation, both in real space and redshift space. The Ω_M values considered for the test are $[0.1, 0.15, 0.2, 0.22, 0.24, 0.26, 0.272, 0.3, 0.35, 0.4, 0.5, 0.6, 0.7, 0.90]$. The 2PCFs are measured in the range [3, 50] Mpc h^{-1}. Excluding scales below 3 Mpc h^{-1} reduces the influence of the fingers of God, which are approximately accounted for in the model through the parameter σ_{12}.

We will present the results in real space first, followed by those in redshift space.

6.1.1 Real space

In real space, by definition, there are no dynamic distortions, and at the true cosmology the isocorrelation curves of the bidimensional 2PCF are circles.

Figures 6.1 and 6.2 show the isocorrelation curves obtained from the bidimensional 2PCF and the respective models at various redshifts, with the true

cosmology case ($\Omega_M = 0.272$) shown in the central columns. For comparison, the other columns show the results at the extremes of the test cosmology interval considered ($\Omega_M = 0.1$ and $\Omega_M = 0.9$). The geometric distortions are noticeable and, as discussed in 4, they increase with redshift. We observe both a stretching along the line of sight for low Ω_M values and a shrinking along the line of sight for high Ω_M values.

In Fig. 6.3, we report the functions $F_{red}(\Omega_M)$ at various redshifts, which quantify the comparison between the measured 2PCFs and their respective models. The narrower the $F_{red}(\Omega_M)$ curve, the more accurately Ω_M can be identified. A narrow curve signifies that, even for values close to the Ω_M corresponding to the minimum, the agreement between the measurement and the model is still bad, thereby making the geometric distortions more apparent. A more quantitative approach could be achieved by estimating the uncertainties in the measurement of the minimum of the function. In the future, this could be accomplished by determining the confidence region through the scatter among different independent measurements of the same type, but obtained from different mock catalogues. The functions $F_{red}(\Omega_M)$ show the expected form, with a minimum that becomes clearer at higher redshifts due to the increased geometric distortions. The values of Ω_M corresponding to the minimum of the $F_{red}(\Omega_M)$ curves are reported in Table 6.1.

The measurements at different redshifts have been considered independent and combined by summing the individual $F_{red}(\Omega_M)$ values to obtain a more accurate estimate of Ω_M. Figure 6.4 shows this sum. This approach enhances the identification of the true Ω_M, as the curve becomes narrower. Therefore, we conclude that, despite having only a small number of independent catalogues, the accuracy of the test improves when applied to multiple catalogues, even at different redshifts.

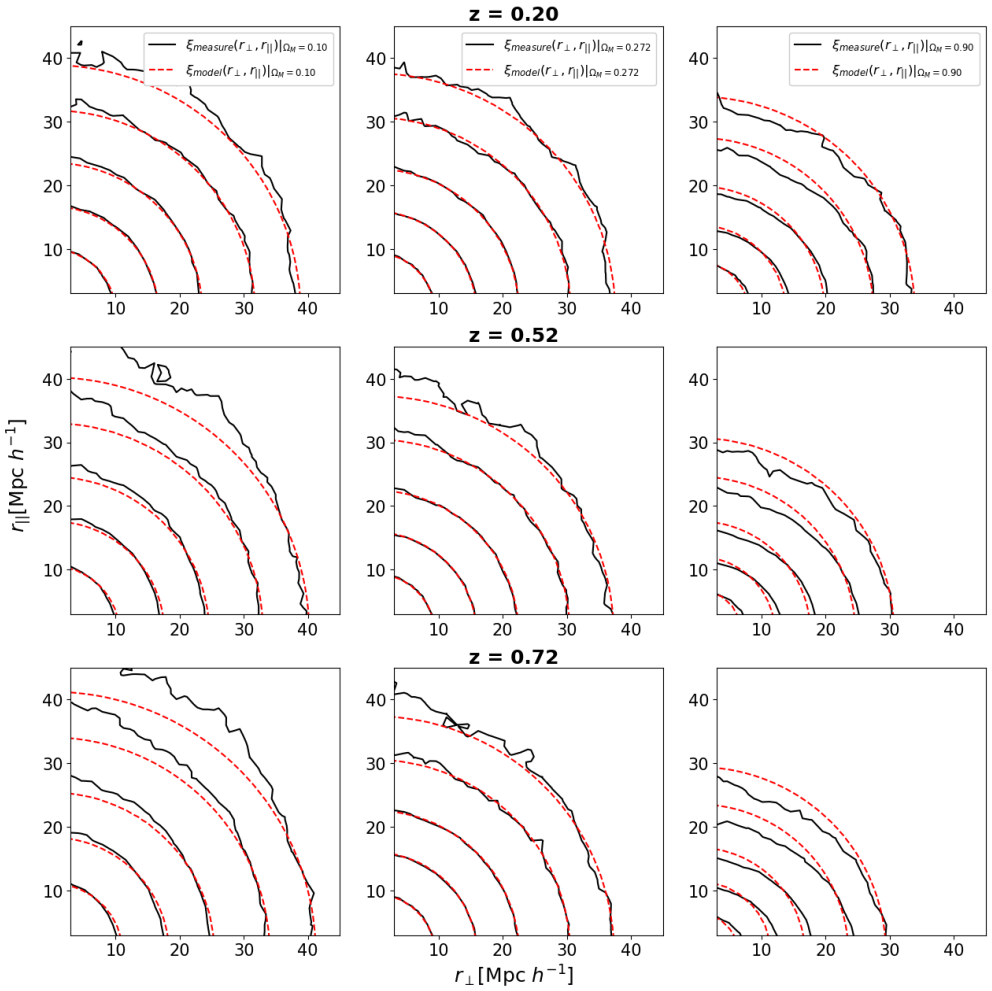

Figure 6.1: Isocorrelation contours at levels $\xi(r_\perp, r_{||}) = [0.03, 0.05, 0.1, 0.2, 0.5]$ for the galaxy catalogues in real space. The continuous black line represents the isocorrelation contours of the measured 2PCF at different test cosmologies: $\Omega_M = 0.10$ in the left column, $\Omega_M = 0.272$ in the central column, and $\Omega_M = 0.90$ in the right column. The dashed red line shows the isocorrelation contours of the 2PCF obtained from the models. The upper panels present the analysis for the galaxy catalogue at $z = 0.20$, the central panels at $z = 0.52$, and the lower panels at $z = 0.72$.

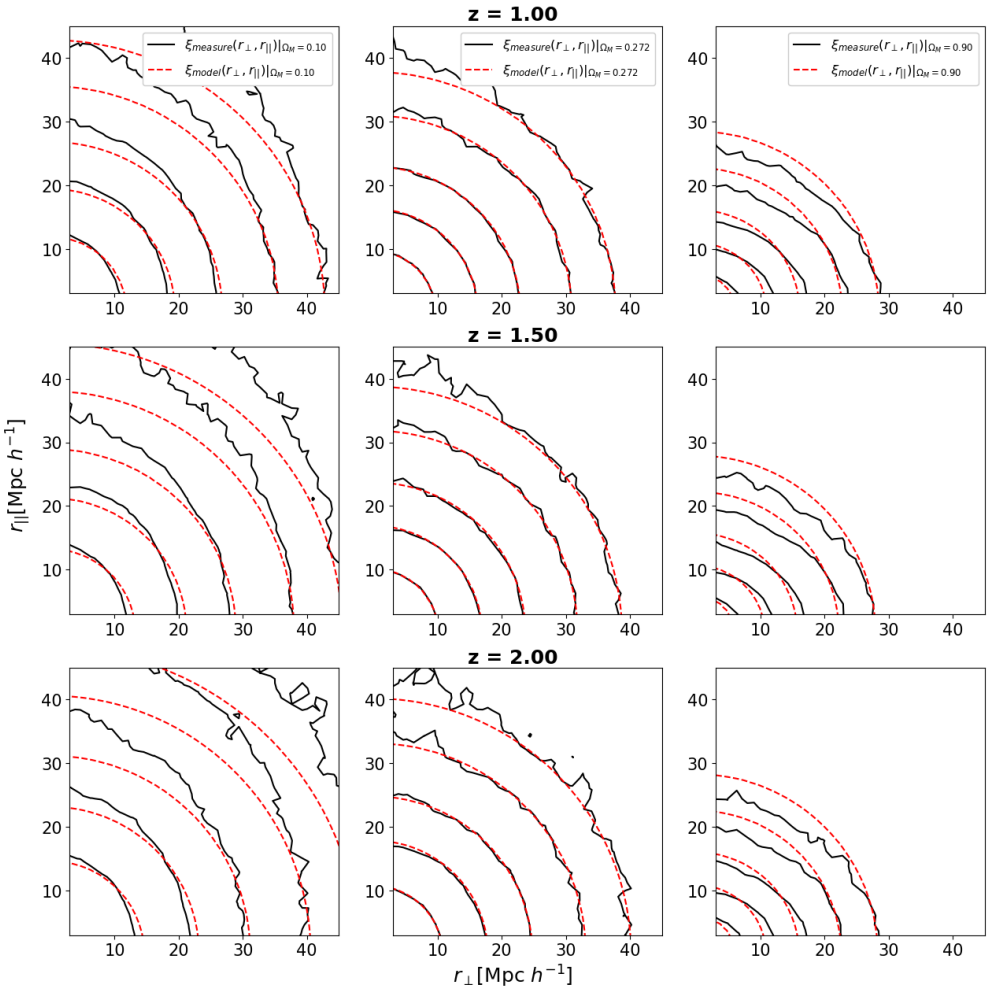

Figure 6.2: Isocorrelation contours at levels $\xi(r_\perp, r_{||}) = [0.03, 0.05, 0.1, 0.2, 0.5]$ for the galaxy catalogues in real space. The continuous black line represents the isocorrelation contours of the measured 2PCF at different test cosmologies: $\Omega_M = 0.10$ in the left column, $\Omega_M = 0.272$ in the central column, and $\Omega_M = 0.90$ in the right column. The dashed red line shows the isocorrelation contours of the 2PCF obtained from the models. The upper panels present the analysis for the galaxy catalogue at $z = 1.00$, the central panels at $z = 1.50$, and the lower panels at $z = 2.00$.

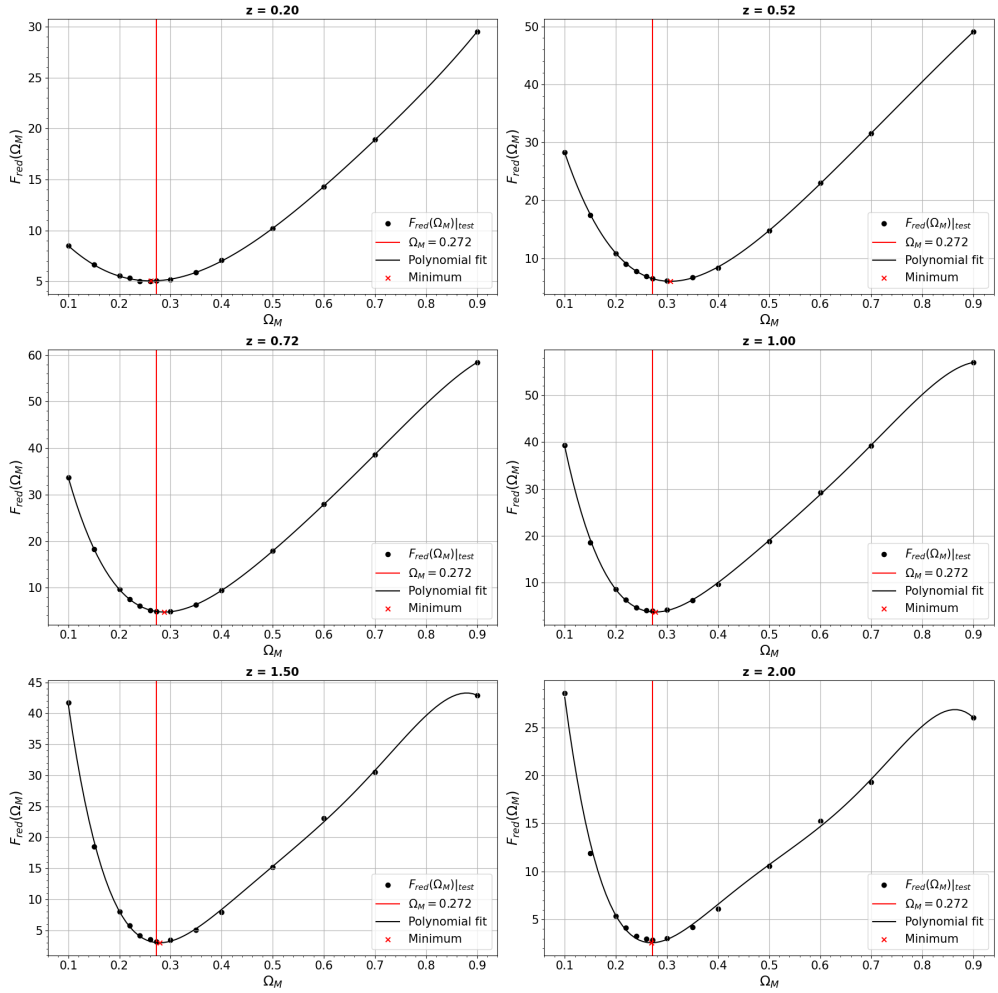

Figure 6.3: The function $F_{red}(\Omega_M)$, defined in Chapter 5, is shown as a function of Ω_M. The points represent the function evaluated at each test cosmology (i.e. at each test Ω_M), while the black line is derived from a polynomial fit of these points. The red vertical line indicates the true Ω_M of the *Magneticum*simulation. The red crosses mark the minimum of the polynomial fit. These values for different redshifts are reported in Table 6.1. Each subplot represents the same analysis but at different redshifts ($[0.20, 0.52, 0.72, 1.00, 1.50, 2.00]$).

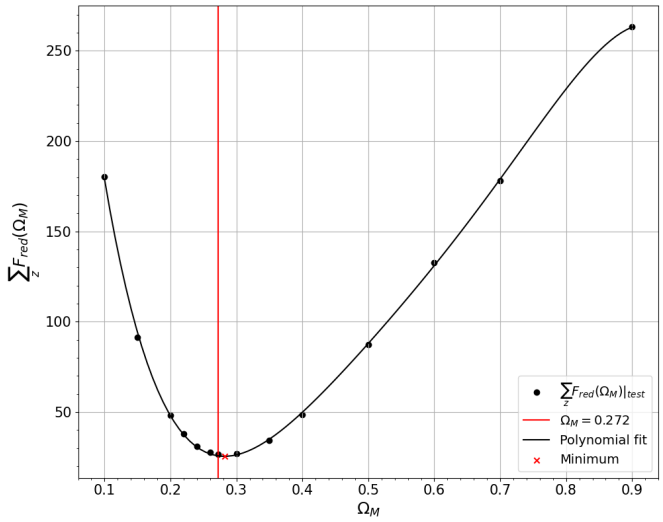

Figure 6.4: The total $F_{red}(\Omega_M)$ obtained by summing all of its values obtained from the galaxy catalogues at different redshifts, for each test cosmology. The symbols of the plot are the same as in Fig. 6.3.

6.1.2 Redshift space

In redshift space, it is necessary to account for dynamical distortions using the method described in Chapter 5. Figures 6.5 and 6.6 show the isocorrelation curves, following the scheme of the previous section. We observe the marginal influence of the fingers of God effect and, at larger scales, the more pronounced Kaiser effect.

In this case, the amplitude of the geometric distortions increases with redshift and is very small at $z = 0.20$. Considering the number of objects and the influence of the dynamical distortions, the best results are obtained at intermediate redshifts. In Fig. 6.7 the $F_{red}(\Omega_M)$ function is shown at different redshifts. As for the real space case, we have considered the six measure of $F_{red}(\Omega_M)$ as independent. We have thus obtained $\sum_z F_{red}(\Omega_M)$ and then plotted in Fig. 6.8.

Table 6.1 reports the values of Ω_M corresponding to the minimum of the $F_{red}(\Omega_M)$ functions. These values represent the cosmology with the least geometric distortions and are thus identified by the test as the true Ω_M parameter. The table includes results for galaxies in both real space and redshift space at different redshifts.

In real space, we observe that higher redshifts, which produce more prominent geometric distortions, lead to a better determination of the true Ω_M value. In redshift space, the best signal is around $z = 1$; for $z > 1$, the effects of dynamical distortions dominate over geometric distortions, making their identification more challenging.

	z	0.20	0.52	0.72	1.00	1.50	2.00	$\sum_z$
Real space	Ω_M	0.261	0.307	0.288	0.277	0.278	0.270	0.282
Redshift space	Ω_M	0.288	0.264	0.252	0.250	0.234	0.293	0.252

Table 6.1: Values of Ω_M correspondent to the minimum of the polynomial fits of the different $F_{red}(\Omega_M)$ functions analyzed.

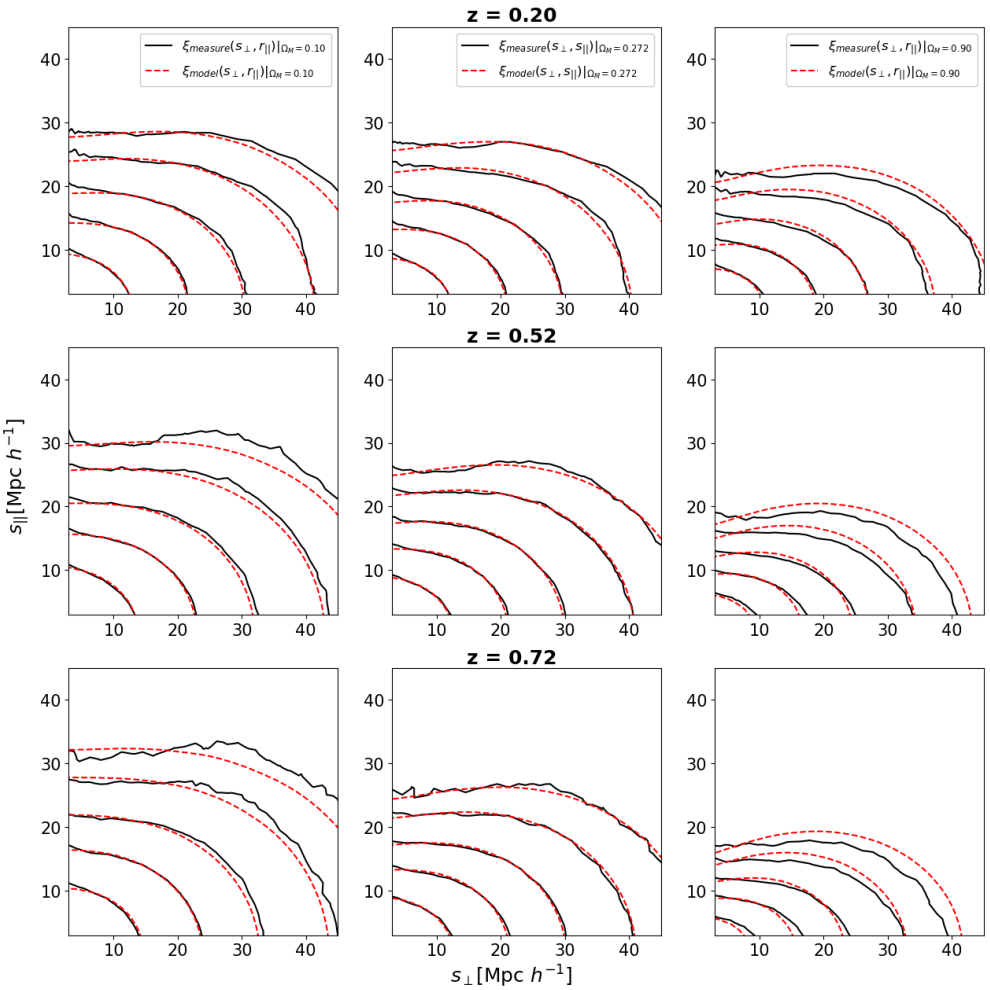

Figure 6.5: Isocorrelation contours at levels $\xi(s_\perp, s_{||}) = [0.03, 0.05, 0.1, 0.2, 0.5]$ for the galaxy catalogues in redshift space. The continuous black line represents the isocorrelation contours of the measured 2PCF at different test cosmologies: $\Omega_M = 0.10$ in the left column, $\Omega_M = 0.272$ in the central column, and $\Omega_M = 0.90$ in the right column. The dashed red line shows the isocorrelation contours of the 2PCF obtained from the models. The upper panels present the analysis for the galaxy catalogue at $z = 0.20$, the central panels at $z = 0.52$, and the lower panels at $z = 0.72$.

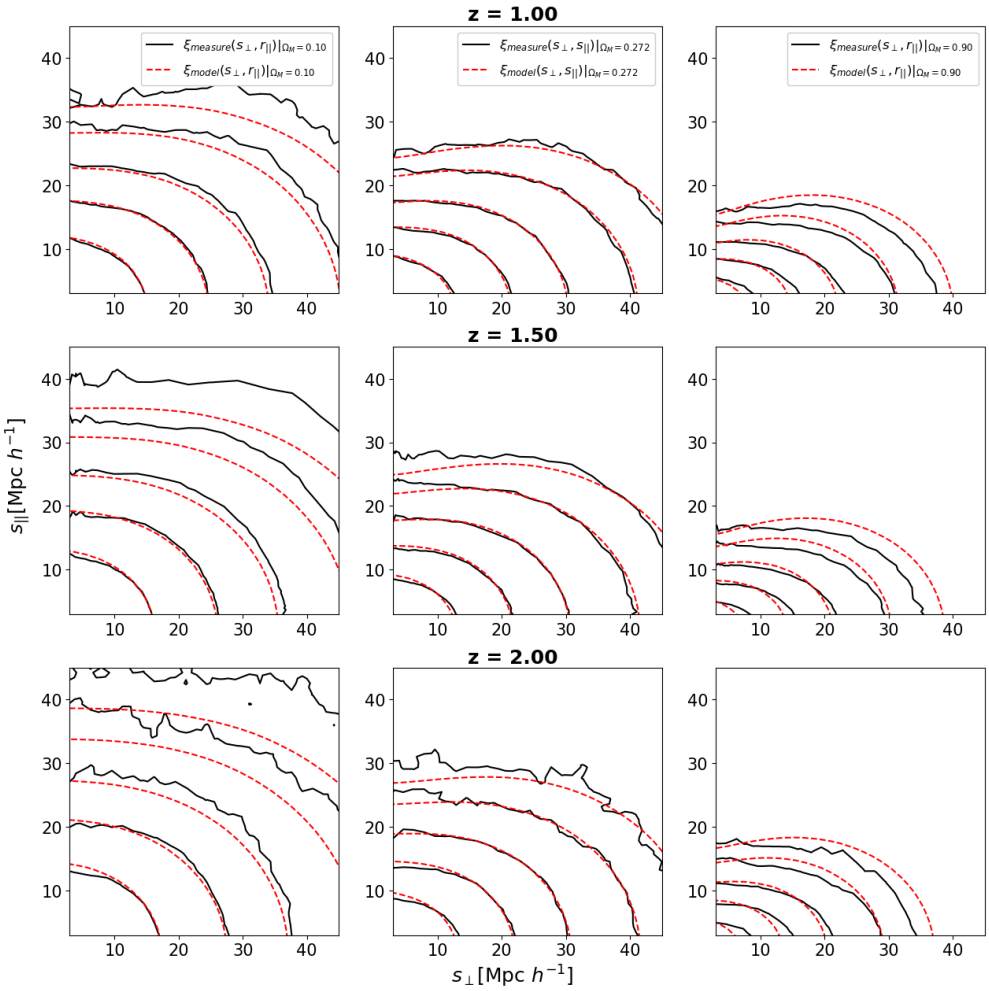

Figure 6.6: Isocorrelation contours at levels $\xi(s_\perp, s_{||}) = [0.03, 0.05, 0.1, 0.2, 0.5]$ for the galaxy catalogues in redshift space. The continuous black line represents the isocorrelation contours of the measured 2PCF at different test cosmologies: $\Omega_M = 0.10$ in the left column, $\Omega_M = 0.272$ in the central column, and $\Omega_M = 0.90$ in the right column. The dashed red line shows the isocorrelation contours of the 2PCF obtained from the models. The upper panels present the analysis for the galaxy catalogue at $z = 1.00$, the central panels at $z = 1.50$, and the lower panels at $z = 2.00$.

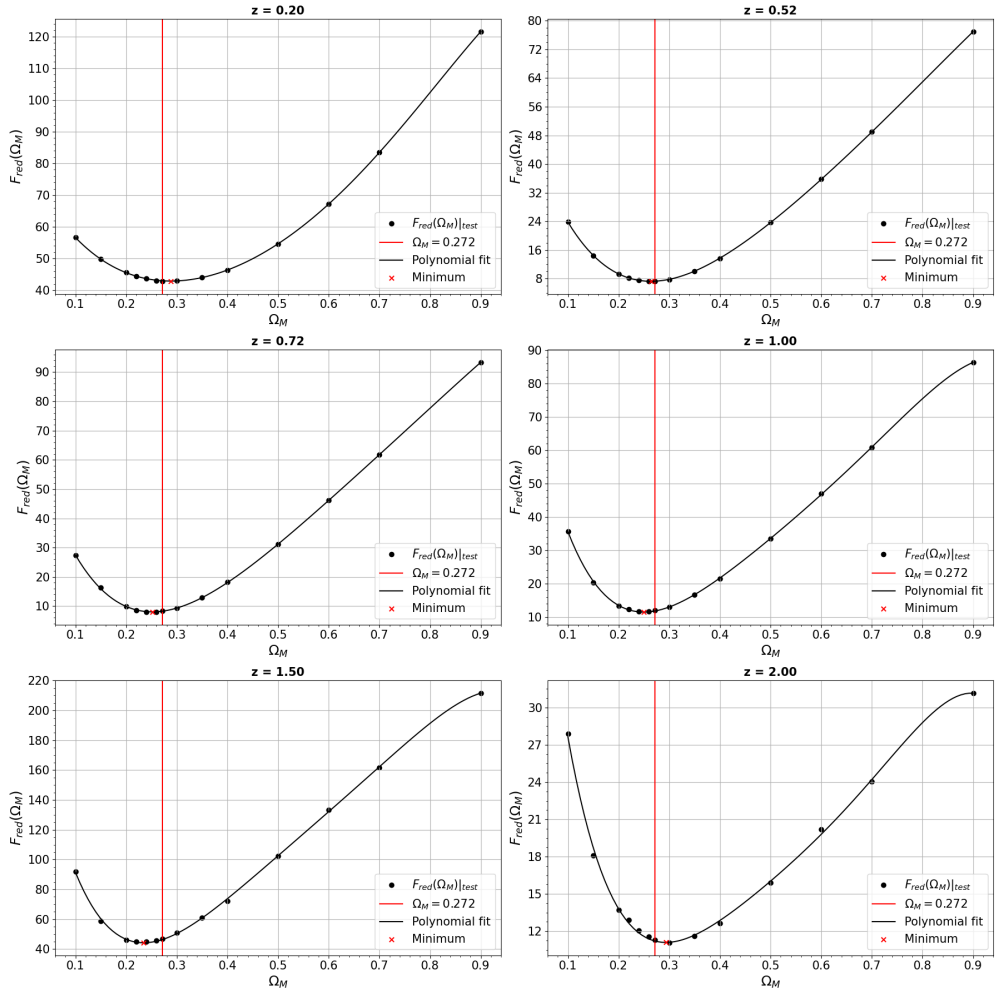

Figure 6.7: The function $F_{red}(\Omega_M)$, defined in Chapter 5, is shown as a function of Ω_M. The points represent the function evaluated at each test cosmology (i.e. at each test Ω_M), while the black line is derived from a polynomial fit of these points. The red vertical line indicates the true Ω_M of the *Magneticum*simulation. The red crosses mark the minimum of the polynomial fit. These values for different redshifts are reported in Table 6.1. Each subplot represents the same analysis but at different redshifts ($[0.20, 0.52, 0.72, 1.00, 1.50, 2.00]$)

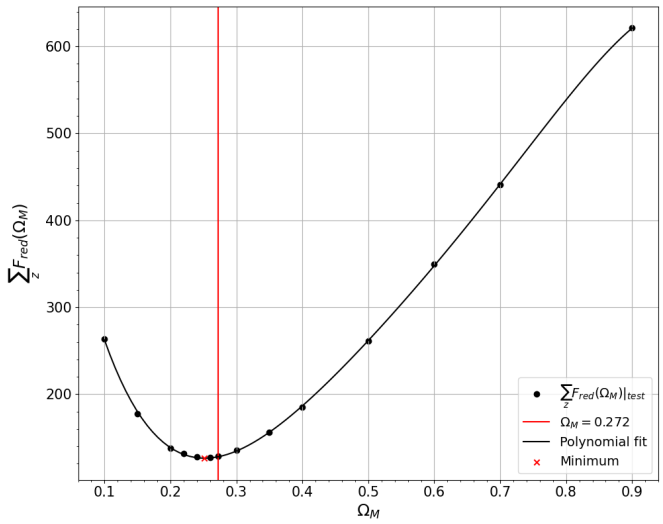

Figure 6.8: The total $F_{red}(\Omega_M)$ obtained by summing all of its values obtained from the galaxy catalogues at different redshifts, for each test cosmology. The symbols of the plot are the same as in Fig. 6.7.

6.2 Cluster catalogues

In this section, we present the results obtained by applying the AP test on the galaxy cluster catalogues extracted from `BOX1` of the *Magneticum* simulation, both in real space and redshift space. The total number of objects in each catalogue is listed in Table 3.2.

6.2.1 Real space

As in the previous section, we present firstly the results obtained in real space. Figures 6.9 and 6.10 show the isocorrelation curves obtained from the measured 2PCF and the model at various redshifts. Figure 6.11 displays the $F_{red}(\Omega_M)$ functions for the different cases.

Similar to the previous cases, the measurements at different redshifts have been combined to improve the identification of the true Ω_M. This approach has also yielded a value close to the true cosmology, as shown in Table 6.2 for real space. The results of these various combinations are presented in Figure 6.12.

We note that the measurements are more affected by errors since clusters are less numerous than galaxies, resulting in less precise constraints on Ω_M. However, the minimums of the function $F_{red}(\Omega_M)$ are correctly positioned, ensuring that the constraints on Ω_M remain accurate.

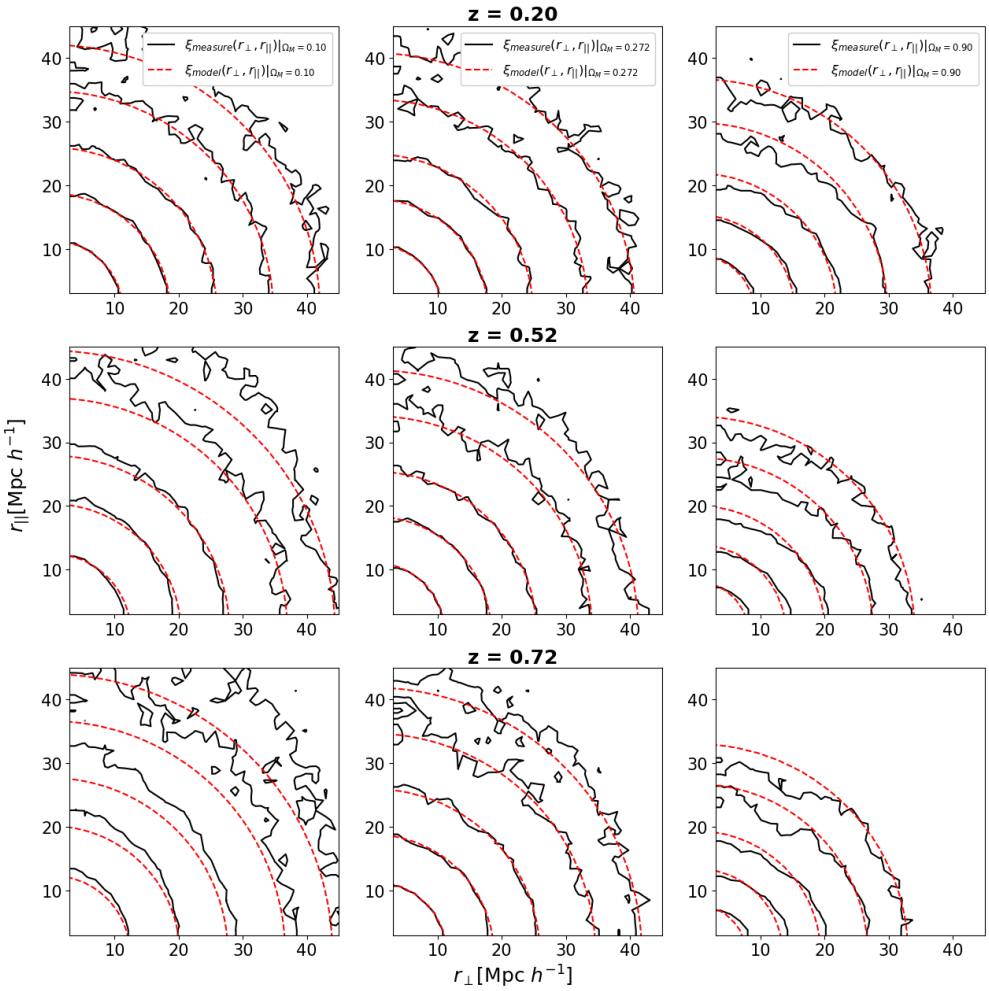

Figure 6.9: Isocorrelation contours at levels $\xi(r_\perp, r_{||}) = [0.03, 0.05, 0.1, 0.2, 0.5]$ for the cluster catalogues in real space. The continuous black line represents the isocorrelation contours of the measured 2PCF at different test cosmologies: $\Omega_M = 0.10$ in the left column, $\Omega_M = 0.272$ in the central column, and $\Omega_M = 0.90$ in the right column. The dashed red line shows the isocorrelation contours of the 2PCF obtained from the models. The upper panels present the analysis for the cluster catalogue at $z = 0.20$, the central panels at $z = 0.52$, and the lower panels at $z = 0.72$.

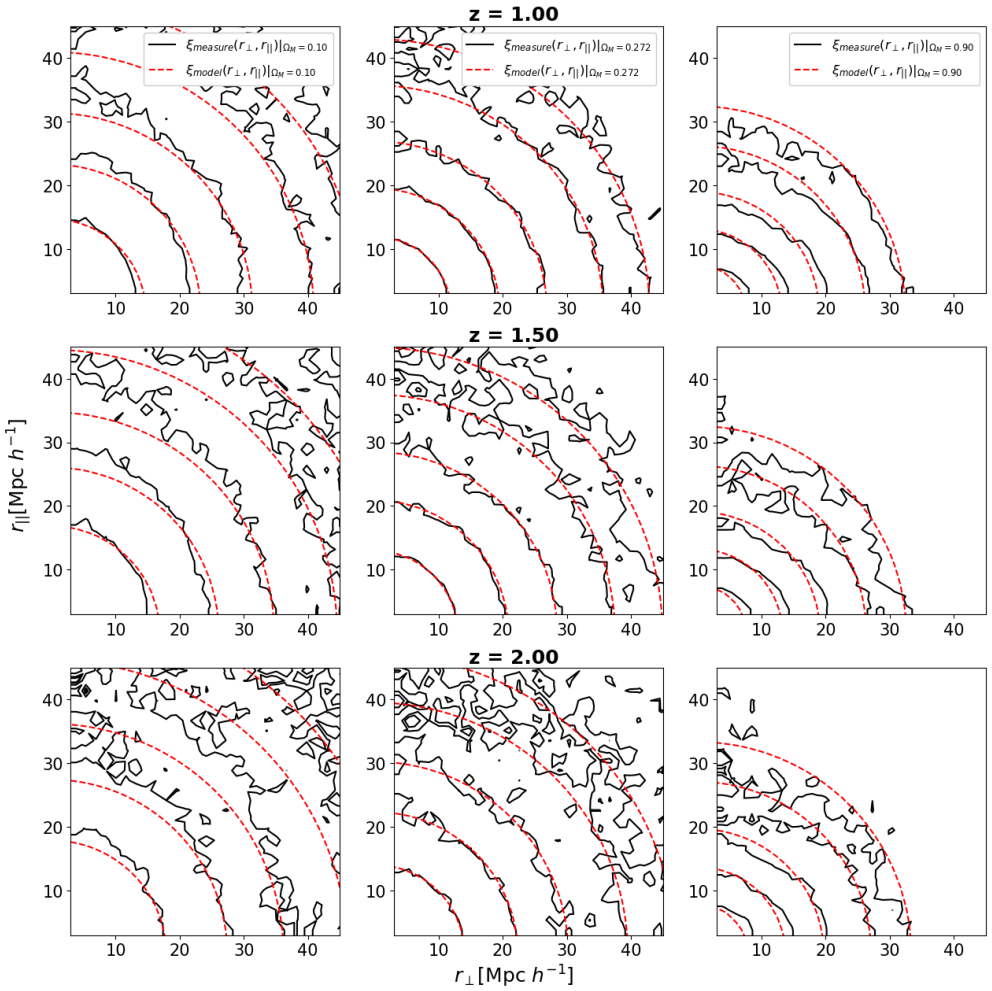

Figure 6.10: Isocorrelation contours at levels $\xi(r_\perp, r_{||}) = [0.03, 0.05, 0.1, 0.2, 0.5]$ for the cluster catalogues in real space. The continuous black line represents the isocorrelation contours of the measured 2PCF at different test cosmologies: $\Omega_M = 0.10$ in the left column, $\Omega_M = 0.272$ in the central column, and $\Omega_M = 0.90$ in the right column. The dashed red line shows the isocorrelation contours of the 2PCF obtained from the models. The upper panels present the analysis for the cluster catalogue at $z = 1.00$, the central panels at $z = 1.50$, and the lower panels at $z = 2.00$.

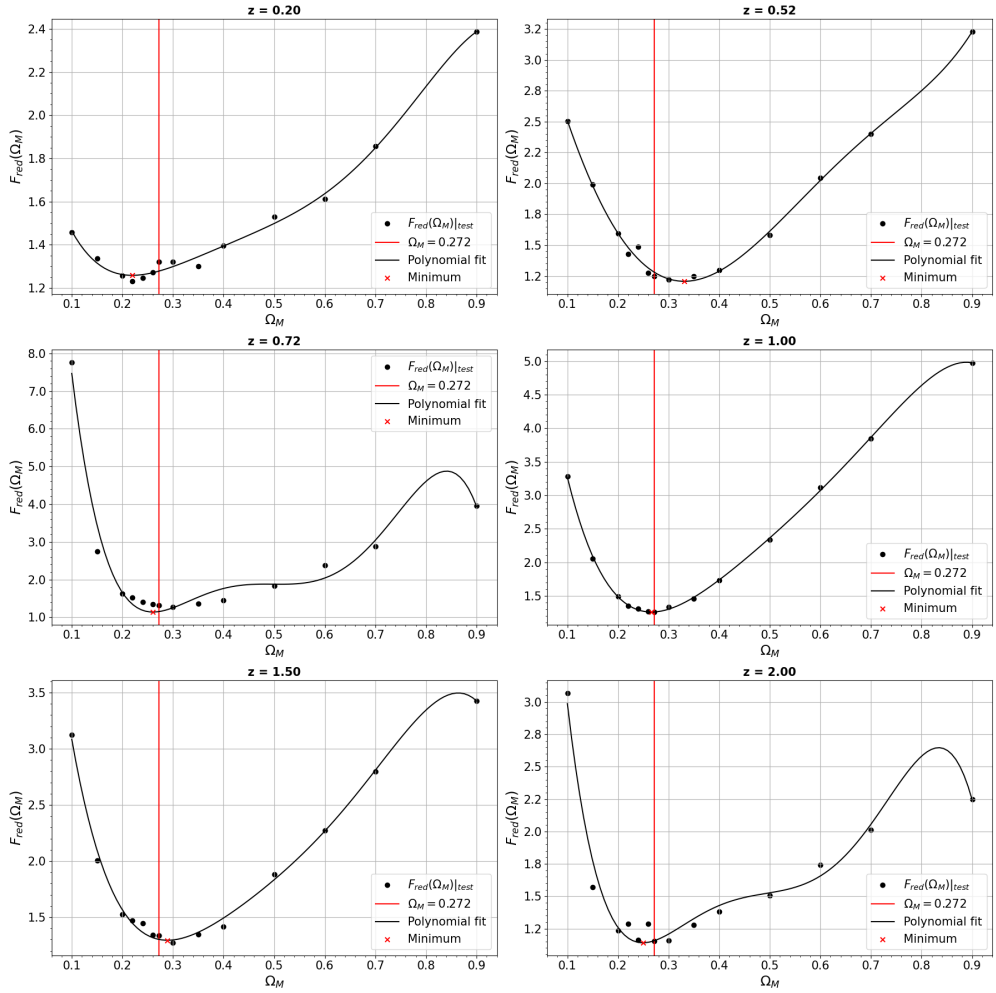

Figure 6.11: The function $F_{red}(\Omega_M)$, defined in Chapter 5, is shown as a function of Ω_M. The points represent the function evaluated at each test cosmology (i.e. at each test Ω_M), while the black line is derived from a polynomial fit of these points. The red vertical line indicates the true Ω_M of the *Magneticum*simulation. The red crosses mark the minimum of the polynomial fit. These values for different redshifts are reported in Table 6.2. Each subplot represents the same analysis but at different redshifts ($[0.20, 0.52, 0.72, 1.00, 1.50, 2.00]$)

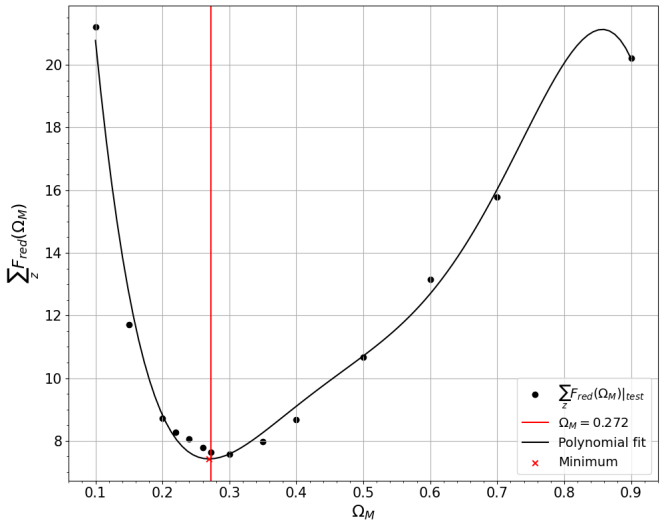

Figure 6.12: The total $F_{red}(\Omega_M)$ obtained by summing all of its values obtained from the cluster catalogues at different redshifts, for each test cosmology. The symbols of the plot are the same as in Fig. 6.11.

6.2.2 Redshift space

Figures 6.13 and 6.14 display the isocorrelation curves in redshift space measured at different redshifts. It is evident that at $z = 0.20$, the geometric distortions are almost negligible. Figure 6.15 shows the $F_{red}(\Omega_M)$ function for each redshift. Additionally, Figure 6.16 presents the combined $F_{red}(\Omega_M)$ functions across different redshifts in redshift space.

Table 6.2 lists the identified Ω_M values for both real space and redshift space, indicating which values introduce the least geometric distortions in the bidimensional 2PCF functions measured for the cluster catalogues. The column labeled $\sum_z$ shows the Ω_M measurement obtained by combining the $F_{red}(\Omega_M)$ functions all different redshifts.

	z	0.20	0.52	0.72	1.00	1.50	2.00	$\sum_z$
Real space	Ω_M	0.219	0.331	0.260	0.266	0.289	0.249	0.270
Redshift space	Ω_M	0.244	0.241	0.225	0.234	0.266	0.245	0.239

Table 6.2: Values of Ω_M correspondent to the minimum of the polynomial fits of the different $F_{red}(\Omega_M)$ functions analyzed.

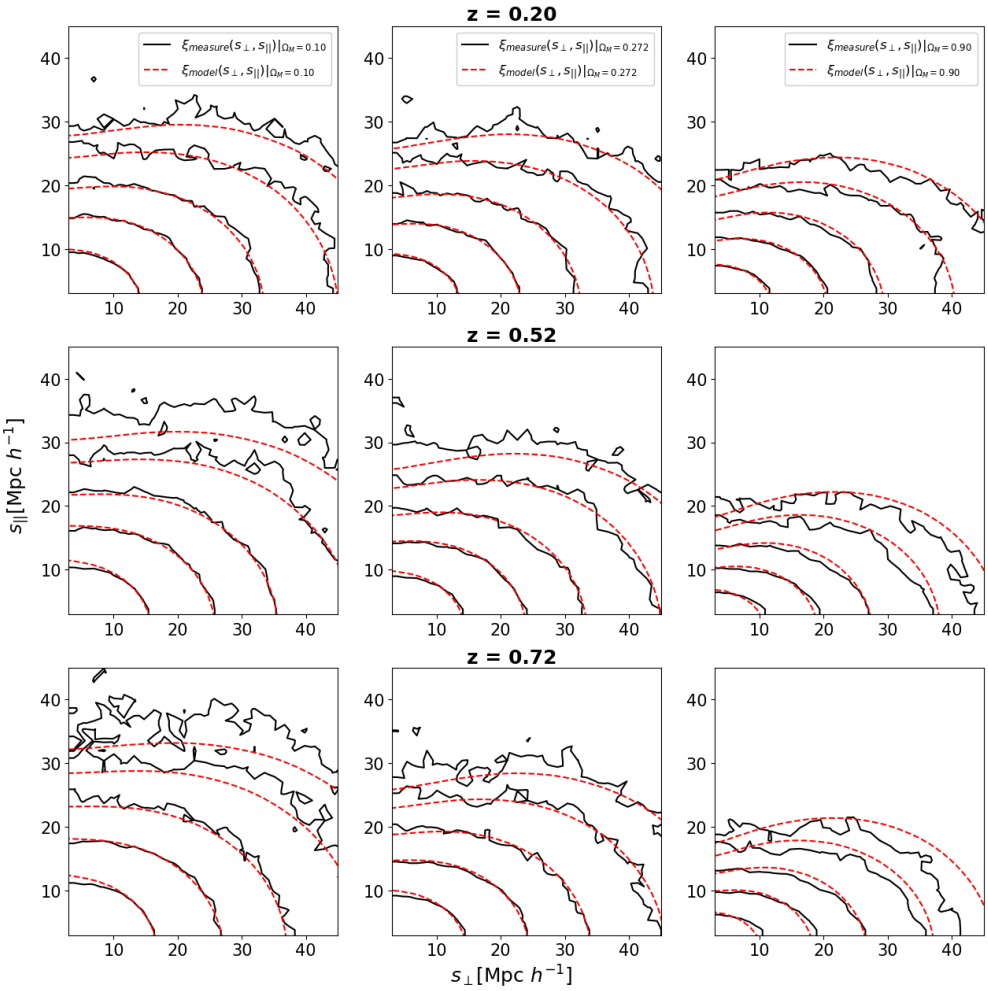

Figure 6.13: Isocorrelation contours at levels $\xi(s_\perp, s_{||}) = [0.03, 0.05, 0.1, 0.2, 0.5]$ for the cluster catalogues in redshift space. The continuous black line represents the isocorrelation contours of the measured 2PCF at different test cosmologies: $\Omega_M = 0.10$ in the left column, $\Omega_M = 0.272$ in the central column, and $\Omega_M = 0.90$ in the right column. The dashed red line shows the isocorrelation contours of the 2PCF obtained from the models. The upper panels present the analysis for the cluster catalogue at $z = 0.20$, the central panels at $z = 0.52$, and the lower panels at $z = 0.72$.

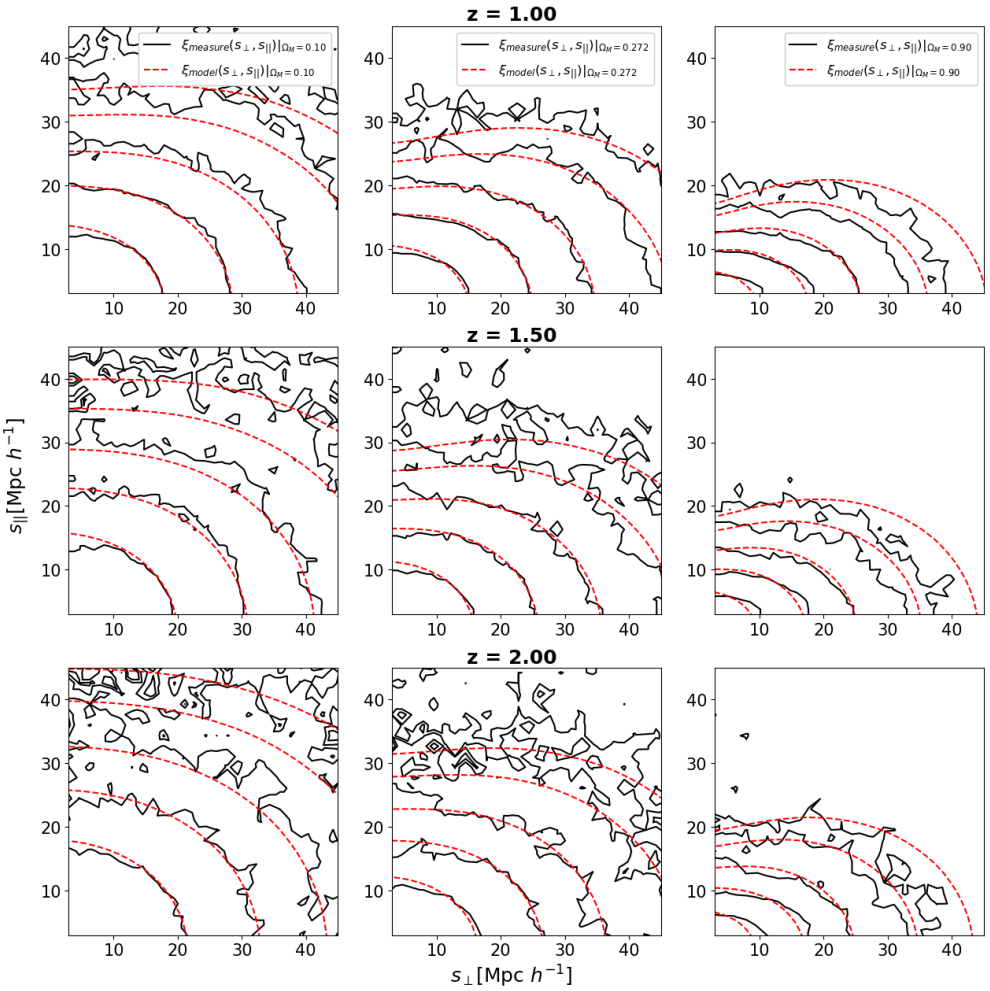

Figure 6.14: Isocorrelation contours at levels $\xi(s_\perp, s_{||}) = [0.03, 0.05, 0.1, 0.2, 0.5]$ for the cluster catalogues in redshift space. The continuous black line represents the isocorrelation contours of the measured 2PCF at different test cosmologies: $\Omega_M = 0.10$ in the left column, $\Omega_M = 0.272$ in the central column, and $\Omega_M = 0.90$ in the right column. The dashed red line shows the isocorrelation contours of the 2PCF obtained from the models. The upper panels present the analysis for the cluster catalogue at $z = 1.00$, the central panels at $z = 1.50$, and the lower panels at $z = 2.00$.

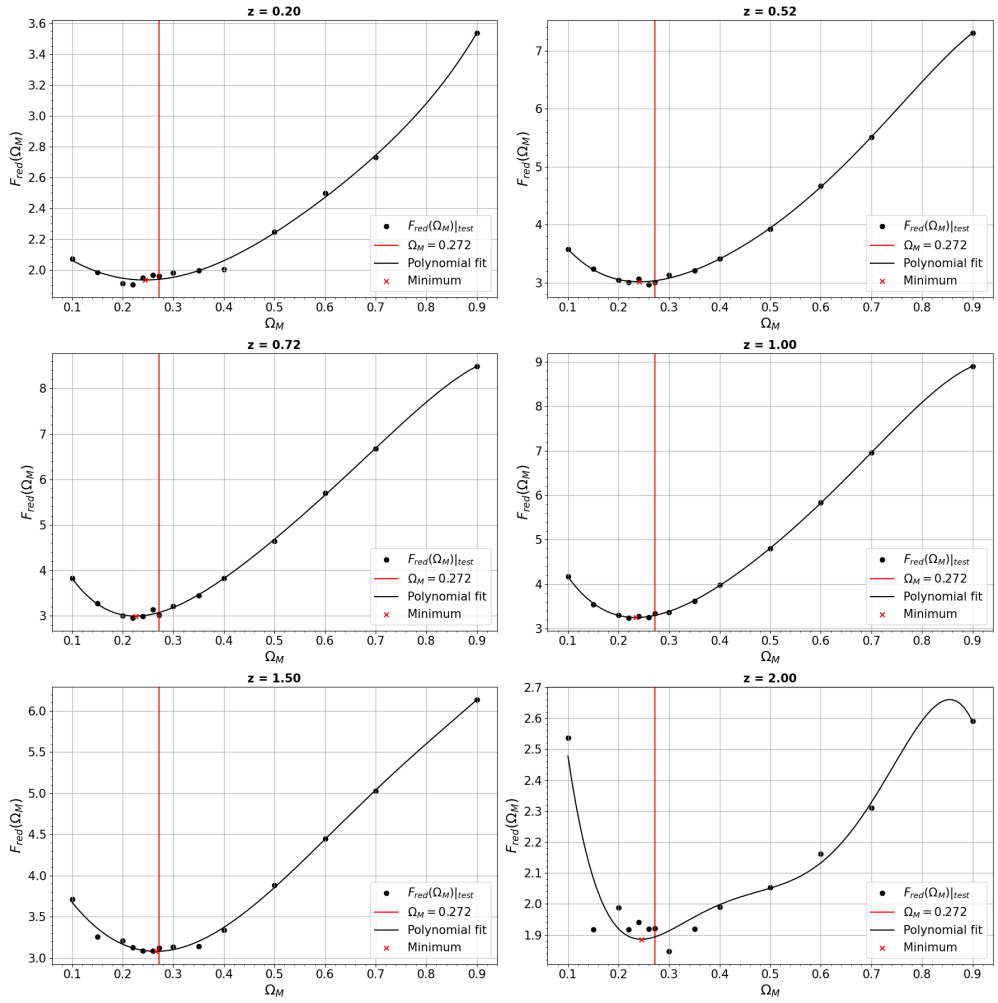

Figure 6.15: The function $F_{red}(\Omega_M)$, defined in Chapter 5, is shown as a function of Ω_M. The points represent the function evaluated at each test cosmology (i.e. at each test Ω_M), while the black line is derived from a polynomial fit of these points. The red vertical line indicates the true Ω_M of the *Magneticum*simulation. The red crosses mark the minimum of the polynomial fit. These values for different redshifts are reported in Table 6.2. Each subplot represents the same analysis but at different redshifts ($[0.20, 0.52, 0.72, 1.00, 1.50, 2.00]$)

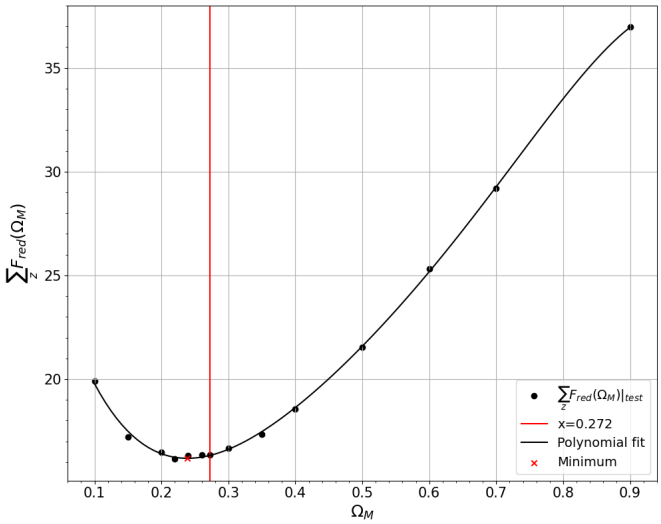

Figure 6.16: The total $F_{red}(\Omega_M)$ obtained by summing all of its values obtained from the cluster catalogues at different redshifts, for each test cosmology. The symbols of the plot are the same as in Fig. 6.15.

6.3 AGN catalogues

Finally, in this section, we present the results obtained through the application of the AP test on the AGN catalogues extracted from `BOX1` of the *Magneticum* simulation. Also in this case the analysis has been performed both in real space and redshift space. The total number of objects contained in each catalogues is reported in Tab. 3.2.

6.3.1 Real space

In Figures 6.17 and 6.18, we show the isocorrelation curves obtained from the measured 2PCF and the model at various redshifts in real space. We observe that the amplitude of the geometric distortions increases with redshift. However, the small number of objects in the catalogues, especially at high redshift, results in very noisy measurements. This noise negatively impacts the precision of the model. This effect is particularly pronounced at $z = 2$, where the number of available objects is ten times fewer than in the galaxy catalogue at the same redshift, this is visible in the lower panel of Figure 6.18.

Figure 6.19 displays the $F_{red}(\Omega_M)$ functions for the different cases. The values that introduce the least geometric distortions are reported in Table 6.3. Despite the smaller number of available objects, the identification of the true value of Ω_M remains unaffected (at least in real space), being underestimated only for $z > 1$.

Similar to the previous cases, the measurements at different redshifts have been combined to improve the identification of the true Ω_M. This approach also yields a value close to the true cosmology, as shown in Table 6.3 for real space. The results of these various combinations are presented in Figure 6.20.

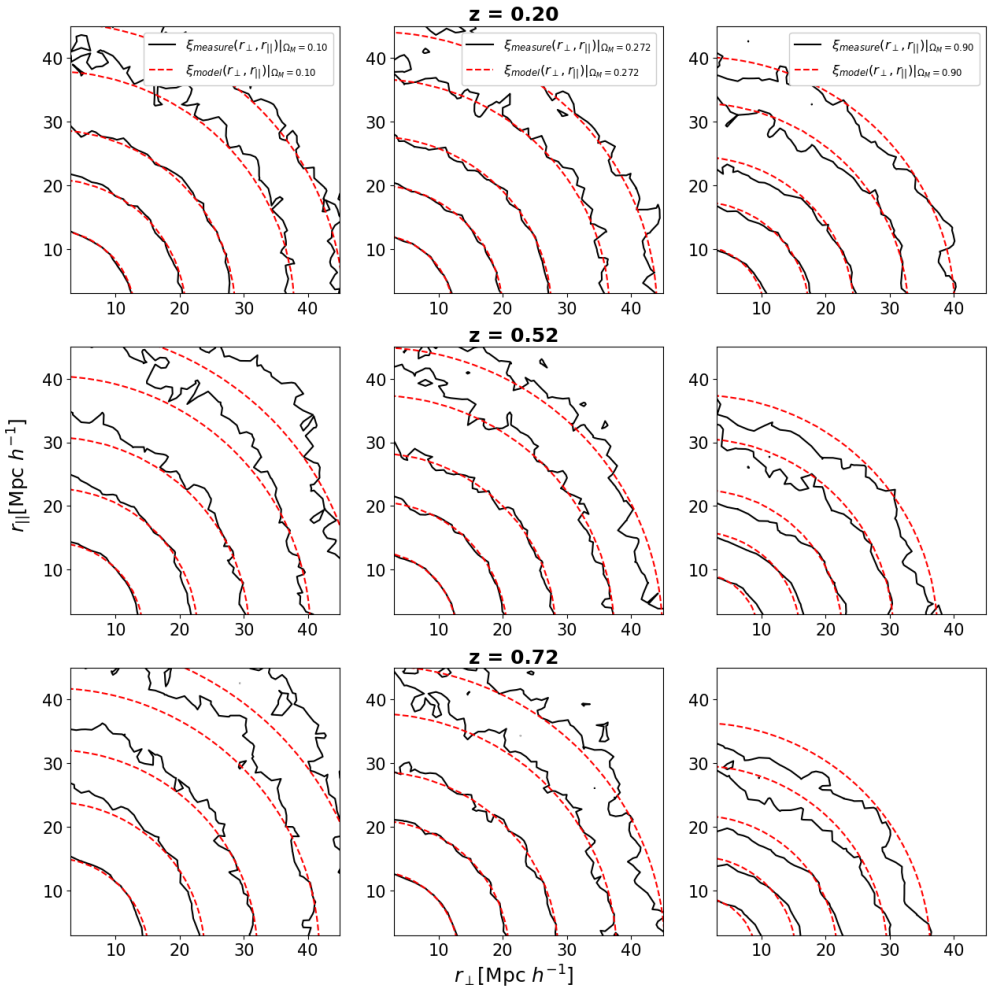

Figure 6.17: Isocorrelation contours at levels $\xi(r_\perp, r_{||}) = [0.03, 0.05, 0.1, 0.2, 0.5]$ for the AGNs catalogues in real space. The continuous black line represents the isocorrelation contours of the measured 2PCF at different test cosmologies: $\Omega_M = 0.10$ in the left column, $\Omega_M = 0.272$ in the central column, and $\Omega_M = 0.90$ in the right column. The dashed red line shows the isocorrelation contours of the 2PCF obtained from the models. The upper panels present the analysis for the AGN catalogue at $z = 0.20$, the central panels at $z = 0.52$, and the lower panels at $z = 0.72$.

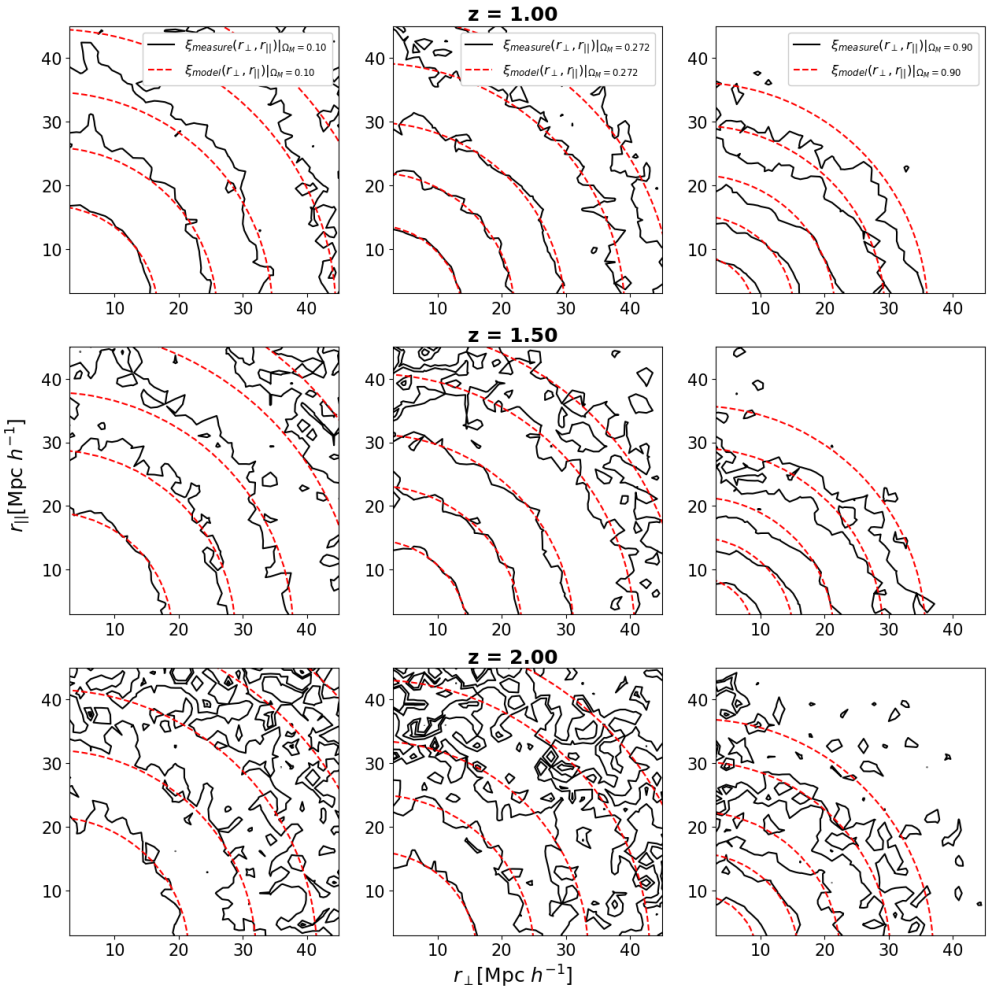

Figure 6.18: Isocorrelation contours at levels $\xi(r_\perp, r_{||}) = [0.03, 0.05, 0.1, 0.2, 0.5]$ for the AGN catalogues in real space. The continuous black line represents the isocorrelation contours of the measured 2PCF at different test cosmologies: $\Omega_M = 0.10$ in the left column, $\Omega_M = 0.272$ in the central column, and $\Omega_M = 0.90$ in the right column. The dashed red line shows the isocorrelation contours of the 2PCF obtained from the models. The upper panels present the analysis for the AGN catalogue at $z = 1.00$, the central panels at $z = 1.50$, and the lower panels at $z = 2.00$.

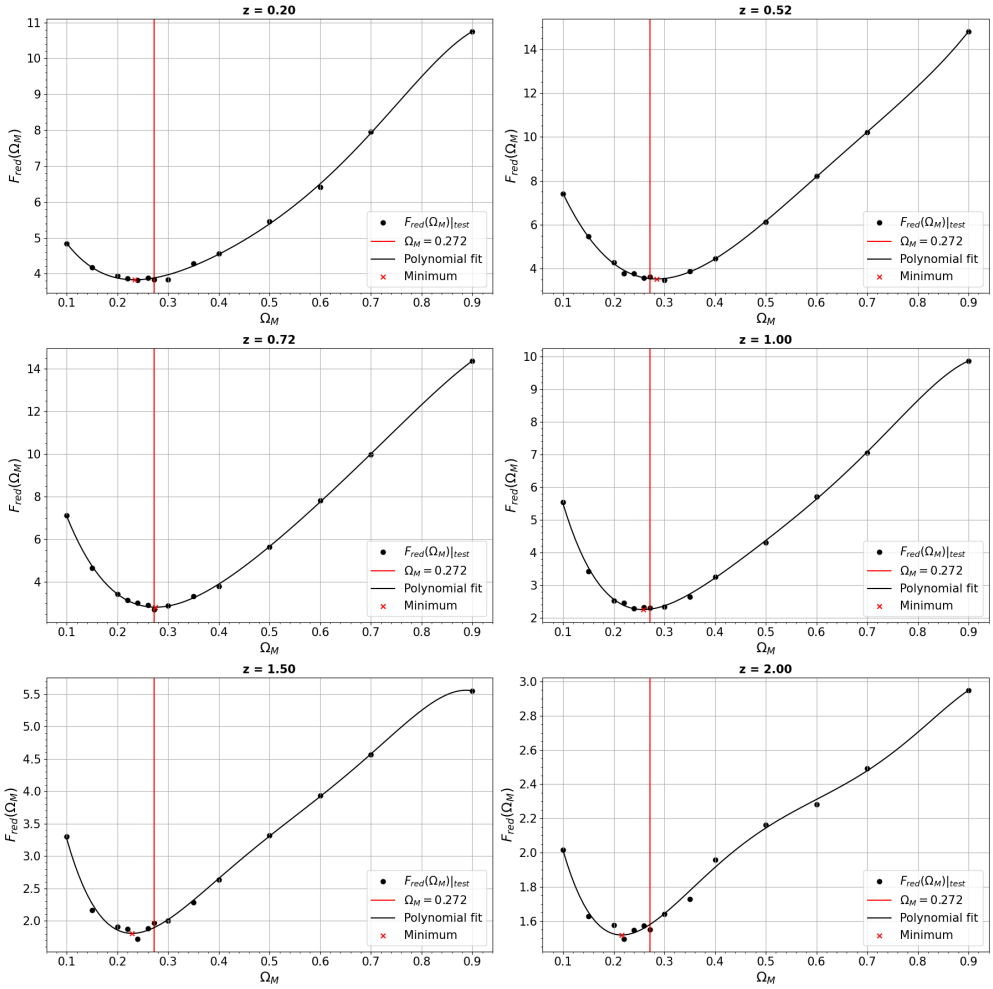

Figure 6.19: The function $F_{red}(\Omega_M)$, defined in Chapter 5, is shown as a function of Ω_M. The points represent the function evaluated at each test cosmology (i.e. at each test Ω_M), while the black line is derived from a polynomial fit of these points. The red vertical line indicates the true Ω_M of the *Magneticum*simulation. The red crosses mark the minimum of the polynomial fit. These values for different redshifts are reported in Table 6.3. Each subplot represents the same analysis but at different redshifts ($[0.20, 0.52, 0.72, 1.00, 1.50, 2.00]$)

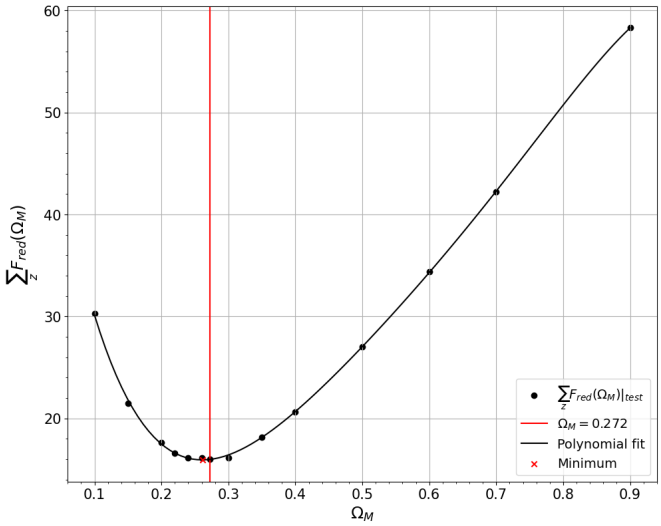

Figure 6.20: The total $F_{red}(\Omega_M)$ obtained by summing all of its values obtained from the galaxy catalogues at different redshifts, for each test cosmology. The symbols of the plot are the same as in Fig. 6.19.

6.3.2 Redshift space

As for the previous catalogues, in the redshift space we have to model also the dynamic distortions. The scale range for the measure is the same used for the galaxies. In Figures 6.21 and 6.22 we display the isocorrelation curves measured at different redshifts. As in the previous case the noise in the measure is given by the small number of objects, especially at high redshift.

Figure 6.23 shows the $F_{red}(\Omega_M)$ function for each redshift. At $z = 2$ we can see how difficult is to identify a clear minimum between the various test cosmology. At this redshift the distortions effects are dominated by the dynamical ones. Additionally, Figure 6.24 presents the combined $F_{red}(\Omega_M)$ functions across different redshifts in redshift space. The plot highlight how in this case the AP test slightly understimate the true cosmology.

In Table 6.3 we list the identified Ω_M values for both real space and redshift space, indicating which values introduce the least geometric distortions in the bidimensional 2PCF functions measured for the cluster catalogues. The column labeled $\sum_z$ shows the Ω_M measurement obtained by combining the $F_{red}(\Omega_M)$ functions across various redshifts.

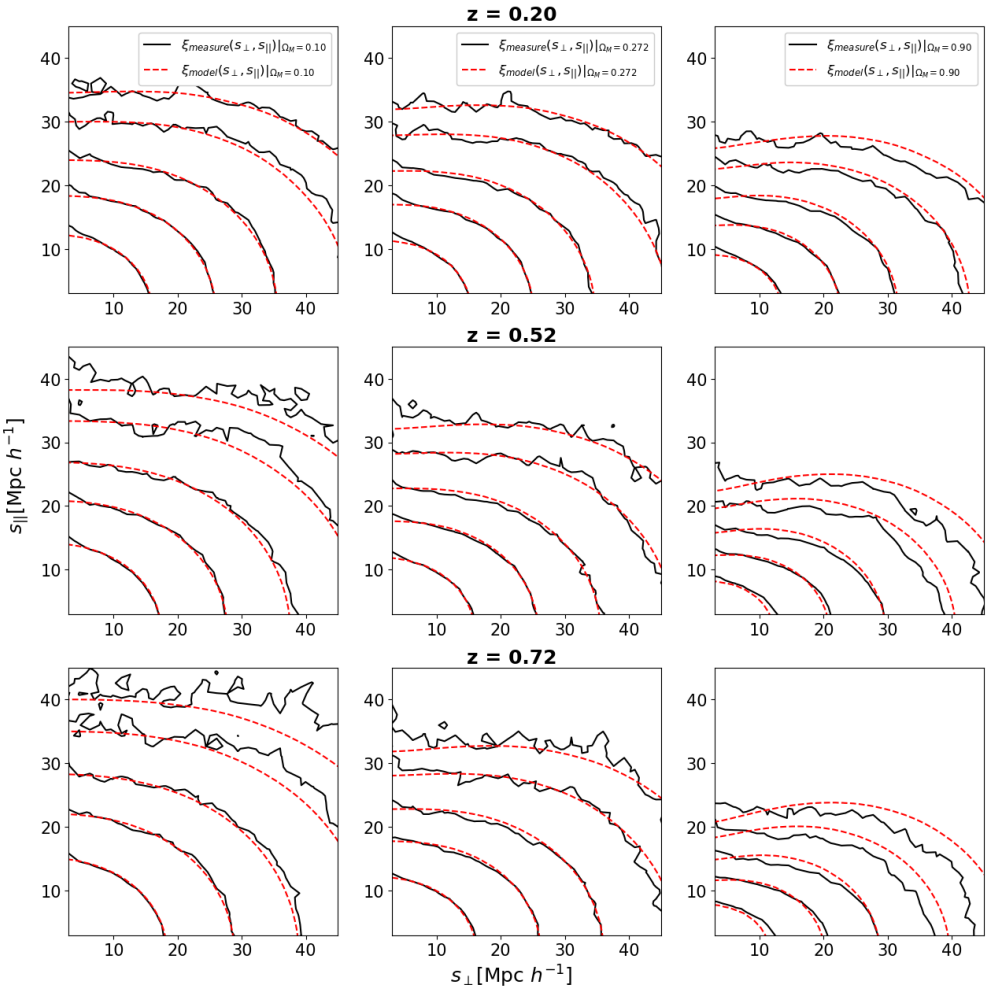

Figure 6.21: Isocorrelation contours at levels $\xi(s_\perp, s_{||}) = [0.03, 0.05, 0.1, 0.2, 0.5]$ for the AGN catalogues in redshift space. The continuous black line represents the isocorrelation contours of the measured 2PCF at different test cosmologies: $\Omega_M = 0.10$ in the left column, $\Omega_M = 0.272$ in the central column, and $\Omega_M = 0.90$ in the right column. The dashed red line shows the isocorrelation contours of the 2PCF obtained from the models. The upper panels present the analysis for the AGN catalogue at $z = 0.20$, the central panels at $z = 0.52$, and the lower panels at $z = 0.72$.

	z	0.20	0.52	0.72	1.00	1.50	2.00	$\sum_z$
Real space	Ω_M	0.234	0.285	0.275	0.258	0.229	0.216	0.261
Redshift space	Ω_M	0.202	0.209	0.211	0.214	0.193	0.179	0.208

Table 6.3: Values of Ω_M correspondent to the minimum of the polynomial fits of the different $F_{red}(\Omega_M)$ functions analyzed.

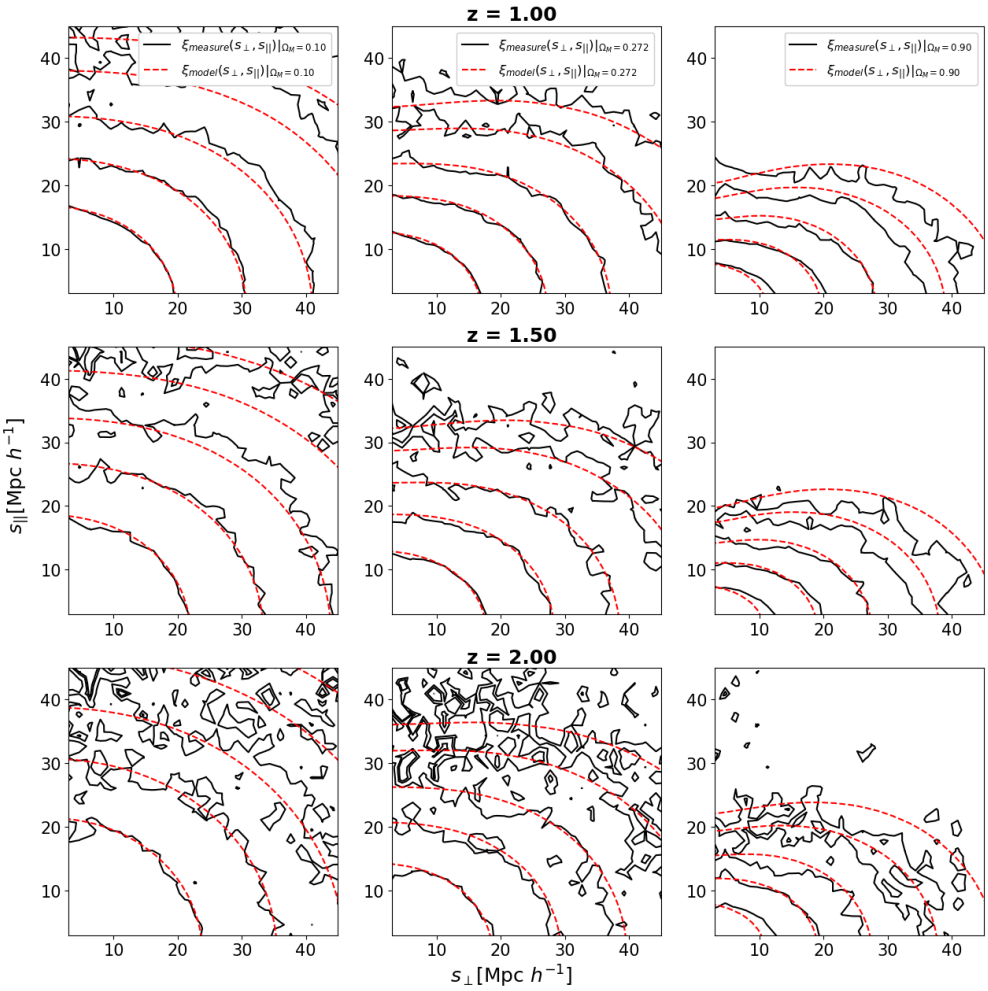

Figure 6.22: Isocorrelation contours at levels $\xi(s_\perp, s_{||}) = [0.03, 0.05, 0.1, 0.2, 0.5]$ for the AGN catalogues in redshift space. The continuous black line represents the isocorrelation contours of the measured 2PCF at different test cosmologies: $\Omega_M = 0.10$ in the left column, $\Omega_M = 0.272$ in the central column, and $\Omega_M = 0.90$ in the right column. The dashed red line shows the isocorrelation contours of the 2PCF obtained from the models. The upper panels present the analysis for the AGN catalogue at $z = 1.00$, the central panels at $z = 1.50$, and the lower panels at $z = 2.00$.

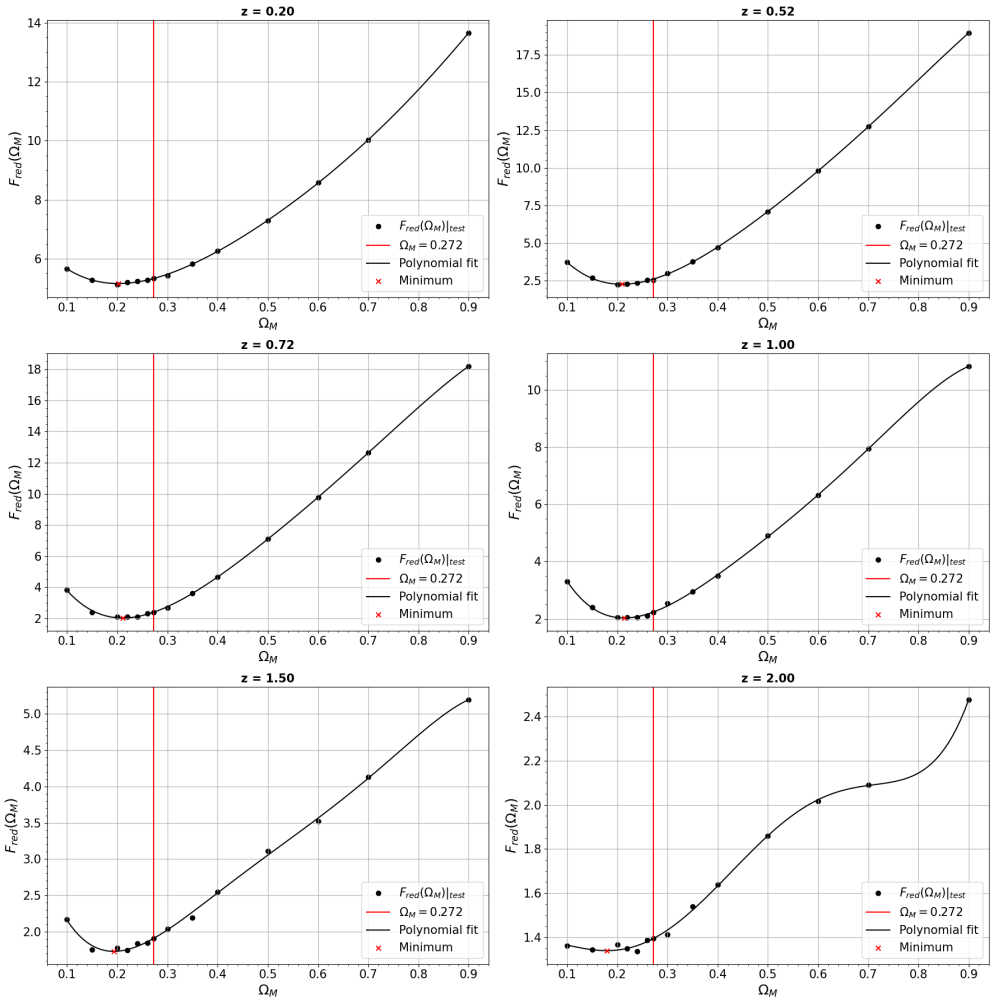

Figure 6.23: The function $F_{red}(\Omega_M)$, defined in Chapter 5, is shown as a function of Ω_M. The points represent the function evaluated at each test cosmology (i.e. at each test Ω_M), while the black line is derived from a polynomial fit of these points. The red vertical line indicates the true Ω_M of the *Magneticum*simulation. The red crosses mark the minimum of the polynomial fit. These values for different redshifts are reported in Table 6.3. Each subplot represents the same analysis but at different redshifts ($[0.20, 0.52, 0.72, 1.00, 1.50, 2.00]$)

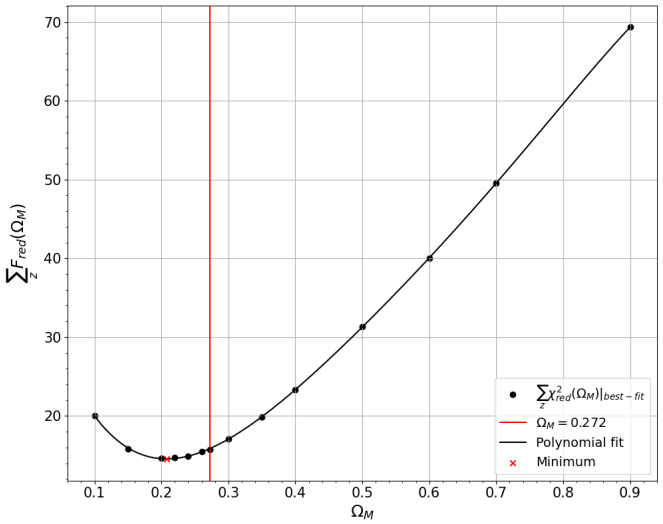

Figure 6.24: The total $F_{red}(\Omega_M)$ obtained by summing all of its values obtained from the galaxy catalogues at different redshifts, for each test cosmology. The symbols of the plot are the same as in Fig. 6.23.

Chapter 7

Conclusions and future perspectives

In this thesis, we investigated the effectiveness of the AP test to constrain the matter density parameter, Ω_M, using a specific implementation described in Chapter 5. The results, detailed in Chapter 6, were obtained for various types of simulated astrophysical tracers (galaxies, clusters of galaxies, and AGNs) at different redshifts. The primary objective was to develop a method on simulated catalogues that could also be applicable to real catalogues in the future. Consequently, we chose not to use the 2PCF measured in real space as the basis for the models used in the AP test. Instead, we used the 2PCF obtained through the Fourier transform of the dark matter 2PCF, a quantity provided by a Boltzmann solver.

The implemented AP test identifies the Ω_M parameter closer to the true one among many test Ω_M values. We validate the method on the *Magneticum* simulation finding accurate results in all of the cases analyzed (Tables 6.1, 6.2, 6.3). Determining the precision and the accuracy of the test is challenging because we could not yet assign an error to the values of Ω_M obtained. This is due to the fact that the function $F_{red}(\Omega_M)$ used in the exploited method does not follow a standard χ^2 distribution, because of the dependency on Ω_M of both the measured 2PCFs and the models.

The main results obtained in this thesis work are the following:

- We measured the bidimensional 2PCFs in both real space and redshift space for three types of tracers: galaxies, galaxy clusters, and AGNs. For each tracer, we utilized six catalogues at different redshifts (z = 0.20, 0.52, 0.72, 1, 1.50, 2). As discussed in Chapter 6, the results show that geometric distortions are appreciable in both real and redshift space.

- We have validated a particular implementation of the AP test on the previously discussed data set (Section 3.3). The test succeded in achieving the goal of constraining the value of the Ω_M parameter (Tables 6.1, 6.2 and 6.3).

- We have observed an increase in geometric distortions with redshift. The best Ω_M estimates were obtained at $z = 0.72$ and $z = 1$, as also reported in [11]. This redshift range is indeed the optimal one for exploiting geometric distortions because at $z < 0.72$, the effect is still small, while at $z > 1$ the effect is countered by the lower number of objects in the catalogues and the stronger dynamical distortions (in redshift space).

- We have compared the results obtained from different tracers. For both real space and redshift space, galaxies proved to be the best tracers to constrain Ω_M. Their $F_{red}(\Omega_M)$ functions, shown in Figures 6.3 and 6.7, are the narrowest around the minimum, indicating the best Ω_M constraints. This advantage is not due to an intrinsic characteristic of galaxies compared to other tracers, but rather the different number of objects used in the test. As we anticipated, a key factor in our analysis is the number density of objects in the catalogues (Tab. 3.2). Using a larger number of objects to measure the 2PCF improves its precision.

For what concern the future perspectives, we have summed them in the following points:

1. Firstly, the deprojection procedure, which is already implemented in the `CosmoBolognaLib`, should be systematically validated on different selected tracers and potential observational uncertainties, including statistical and systematic errors on the redshift.

2. The deprojected 2PCF (and also, for testing purposes, the true 2PCF measured in real space) has to be implemented in the dispersion model within the `CosmoBolognaLib`. This integration would allow us to perform a detailed test of the method we will use with real data (using the deprojected 2PCF) with the current results obtained in this thesis.

3. The method shall be tested also on other cosmological parameters, in particular with the parameters of the dark energy equation of state w_0 and w_a [16] [42] and on other cosmological frameworks beyond the ΛCDM model.

4. The method should also be tested with more realistic mock catalogues including all the possible observational effects. In particular, it will be important to investigate the impact of redshift uncertainties on the accuracy of cosmological parameter constraints.

5. Then the method should be applied to a sufficiently large number of different independent simulated catalogues to estimate the confidence regions on all the main cosmological parameters, for different selections in volume, tracer density, and redshift.

6. Finally, this AP test will be applied to real available catalogues (e.g. Baryon Oscillation Spectroscopic Survey, BOSS [3]) and relative mock catalogues to estimate the uncertainties on the derived cosmological constraints.

7. It will eventually be interesting to provide forecasts on ongoing future projects whose data are about to become available (e.g. Euclid [4], LSST [5] and DESI [6]).

Bibliography

[1] URL: https://gitlab.com/federicomarulli/CosmoBolognaLib.

[2] URL: https://camb.readthedocs.io/en/latest/.

[3] URL: https://www.sdss4.org/surveys/boss/.

[4] URL: https://www.esa.int/Science_Exploration/Space_Science/Euclid.

[5] URL: https://www.lsst.org/.

[6] URL: https://www.desi.lbl.gov/.

[7] Rémi Adam et al. "Planck 2015 results-I. Overview of products and scientific results". In: *Astronomy & Astrophysics* 594 (2016), A1.

[8] European Space Agency. URL: https://www.esa.int/ESA_Multimedia/Images/2013/03/Planck_CMB.

[9] Charles Alcock and Bohdan Paczyński. "An evolution free test for non-zero cosmological constant." In: *Nature* 281.5730 (1979).

[10] Jasjeet Singh Bagla. "Cosmological N-body simulation: Techniques, scope and status". In: *Current science* (2005), pp. 1088–1100.

[11] WE Ballinger, JA Peacock, and AF Heavens. "Measuring the cosmological constant with redshift surveys". In: *Monthly Notices of the Royal Astronomical Society* 282.3 (1996), pp. 877–888.

[12] Matthew R Bate and Andreas Burkert. "Resolution requirements for smoothed particle hydrodynamics calculations with self-gravity". In: *Monthly Notices of the Royal Astronomical Society* 288.4 (1997), pp. 1060–1072.

[13] Hermann Bondi and Fred Hoyle. "On the mechanism of accretion by stars". In: *Monthly Notices of the Royal Astronomical Society* 104.5 (1944), pp. 273–282.

[14] HJ1952MNRAS Bondi. "On spherically symmetrical accretion". In: *Monthly Notices of the Royal Astronomical Society* 112.2 (1952), pp. 195–204.

[15] Gilles Chabrier. "Galactic stellar and substellar initial mass function1". In: *Publications of the Astronomical Society of the Pacific* 115.809 (2003), p. 763.

[16] MICHEL CHEVALLIER and DAVID POLARSKI. "ACCELERATING UNIVERSES WITH SCALING DARK MATTER". In: *International Journal of Modern Physics D* 10.02 (Apr. 2001), pp. 213–223. ISSN: 1793-6594. DOI: 10.1142/s0218271801000822. URL: http://dx.doi.org/10.1142/S0218271801000822.

[17] Planck Collaboration et al. "Planck 2018 results". In: *A&a* 641 (2020), A12.

[18] Marc Davis and PJE Peebles. "A survey of galaxy redshifts. V-The two-point position and velocity correlations". In: *Astrophysical Journal, Part 1 (ISSN 0004-637X), vol. 267, April 15, 1983, p. 465-482.* 267 (1983), pp. 465–482.

[19] Eleonora Di Valentino et al. "In the realm of the Hubble tension—a review of solutions". In: *Classical and Quantum Gravity* 38.15 (2021), p. 153001.

[20] Scott Dodelson and Fabian Schmidt. *Modern cosmology*. Academic press, 2020.

[21] K Dolag et al. "Substructures in hydrodynamical cluster simulations". In: *Monthly Notices of the Royal Astronomical Society* 399.2 (2009), pp. 497–514.

[22] Klaus Dolag. "The magneticum simulations, from galaxies to galaxy clusters". In: *IAU General Assembly* 29 (2015), p. 2250156.

[23] JW Eastwood and RW Hockney. "Computer Simulation using particles". In: *New York: Mc GrawHill* (1981).

[24] A Einstein. "Kosmologische Betrachtungen zur allgemeinen Relativitätstheorie, 8 Feb 1917. Cosmological Considerations in the General Theory of Relativity, 8 Feb 1917". In: (1917). URL: https://cds.cern.ch/record/632340.

[25] Francesco Falo. "Nuova misura del parametro di densità della materia dalle distorsioni geometriche nel clustering delle galassie BOSS". PhD thesis. URL: http://amslaurea.unibo.it/15438/.

[26] GJ Ferland et al. "CLOUDY 90: numerical simulation of plasmas and their spectra". In: *Publications of the Astronomical Society of the Pacific* 110.749 (1998), p. 761.

[27] Matteo Gaspari. "Vincoli cosmologici dalle distorsioni geometriche della funzione di correlazione". PhD thesis. URL: http://amslaurea.unibo.it/9855/.

[28] Alan H Guth. "Inflationary universe: A possible solution to the horizon and flatness problems". In: *Physical Review D* 23.2 (1981), p. 347.

[29] Francesco Haardt and Piero Madau. "Modelling the UV/X-ray cosmic background with CUBA". In: *arXiv preprint astro-ph/0106018* (2001).

[30] Michaela Hirschmann et al. "Cosmological simulations of black hole growth: AGN luminosities and downsizing". In: *Monthly Notices of the Royal Astronomical Society* 442.3 (2014), pp. 2304–2324.

[31] RW Hockney. "Measurements of collision and heating times in a two-dimensional thermal computer plasma". In: *Journal of Computational Physics* 8.1 (1971), pp. 19–44.

[32] Fred Hoyle and Raymond A Lyttleton. "The effect of interstellar matter on climatic variation". In: *Mathematical proceedings of the Cambridge philosophical society*. Vol. 35. 3. Cambridge University Press. 1939, pp. 405–415.

[33] JP Huchra and MJs Geller. "Groups of galaxies. I-Nearby groups". In: *Astrophysical Journal, Part 1, vol. 257, June 15, 1982, p. 423-437. Research supported by Cambridge University.* 257 (1982), pp. 423–437.

[34] Nick Kaiser. "Clustering in real space and in redshift space". In: *Monthly Notices of the Royal Astronomical Society* 227.1 (1987), pp. 1–21.

[35] Martin Kerscher, Istvan Szapudi, and Alexander S Szalay. "A comparison of estimators for the two-point correlation function". In: *The astrophysical journal* 535.1 (2000), p. L13.

[36] E. Komatsu et al. "SEVEN-YEARWILKINSON MICROWAVE ANISOTROPY PROBE(WMAP) OBSERVATIONS: COSMOLOGICAL INTERPRETATION". In: *The Astrophysical Journal Supplement Series* 192.2 (Jan. 2011), p. 18. ISSN: 1538-4365. DOI: 10.1088/0067-0049/192/2/18. URL: http://dx.doi.org/10.1088/0067-0049/192/2/18.

[37] Eiichiro Komatsu et al. "Five-year wilkinson microwave anisotropy probe* observations: cosmological interpretation". In: *The Astrophysical Journal Supplement Series* 180.2 (2009), p. 330.

[38] Antoine Labatie et al. "Uncertainty in 2-point correlation function estimators and baryon acoustic oscillation detection in galaxy surveys". In: *Statistical Methodology* 9.1-2 (2012), pp. 85–100.

[39] Stephen D Landy and Alexander S Szalay. "Bias and variance of angular correlation functions". In: *Astrophysical Journal, Part 1 (ISSN 0004-637X), vol. 412, no. 1, p. 64-71.* 412 (1993), pp. 64–71.

[40] Georges Lemaıtre. "Un Univers homogène de masse constante et de rayon croissant rendant compte de la vitesse radiale des nébuleuses extra-galactiques". In: *Annales de la Société Scientifique de Bruxelles, A47, p. 49-59* 47 (1927), pp. 49–59.

[41] Xiao-Dong Li et al. "Cosmological constraints from the redshift dependence of the Alcock–Paczynski test and volume effect: galaxy two-point correlation function". In: *Monthly Notices of the Royal Astronomical Society* 450.1 (2015), pp. 807–814.

[42] Eric V. Linder. "Exploring the Expansion History of the Universe". In: *Physical Review Letters* 90.9 (Mar. 2003). ISSN: 1079-7114. DOI: 10.1103/physrevlett.90.091301. URL: http://dx.doi.org/10.1103/PhysRevLett.90.091301.

[43] F. Marulli, A. Veropalumbo, and M. Moresco. "CosmoBolognaLib: C++ libraries for cosmological calculations". In: *Astronomy and Computing* 14 (Jan. 2016), pp. 35–42. ISSN: 2213-1337. DOI: 10.1016/j.ascom.2016.01.005. URL: http://dx.doi.org/10.1016/j.ascom.2016.01.005.

[44] Federico Marulli et al. "Cosmology with clustering anisotropies: disentangling dynamic and geometric distortions in galaxy redshift surveys". In: *Monthly Notices of the Royal Astronomical Society* 426.3 (2012), pp. 2566–2580.

[45] Federico Marulli et al. "Redshift-space distortions of galaxies, clusters, and AGN: Testing how the accuracy of growth rate measurements depends on scales and sample selections". In: *Astronomy amp; Astrophysics* 599 (Mar. 2017), A106. ISSN: 1432-0746. DOI: 10.1051/0004-6361/201526885. URL: http://dx.doi.org/10.1051/0004-6361/201526885.

[46] Federico Marulli et al. "The VIMOS Public Extragalactic Redshift Survey (VIPERS)-Luminosity and stellar mass dependence of galaxy clustering at 0.5¡ z¡ 1.1". In: *Astronomy & Astrophysics* 557 (2013), A17.

[47] Colin McGill. "The redshift projection–I. Caustics and correlation functions". In: *Monthly Notices of the Royal Astronomical Society* 242.3 (1990), pp. 428–438.

[48] University of Oregon. URL: `https://pages.uoregon.edu/jimbrau/astr123/Notes/Chapter27.html`.

[49] PJE Peebles. "Statistical analysis of catalogs of extragalactic objects. iv. cross-correlation of the abell and shane-wirtanen catalogs". In: *Astrophysical Journal Supplement, vol. 28, p. 37 (1974)* 28 (1974), p. 37.

[50] William H Press and Marc Davis. "How to identify and weigh virialized clusters of galaxies in a complete redshift catalog". In: *Astrophysical Journal, Part 1, vol. 259, Aug. 15, 1982, p. 449-473.* 259 (1982), pp. 449–473.

[51] Adam G Riess et al. "Observational evidence from supernovae for an accelerating universe and a cosmological constant". In: *The astronomical journal* 116.3 (1998), p. 1009.

[52] Will Saunders, Michael Rowan-Robinson, and Andy Lawrence. "The spatial correlation function of IRAS galaxies on small and intermediate scales". In: *Monthly Notices of the Royal Astronomical Society* 258.1 (1992), pp. 134–146.

[53] Volker Springel. "The cosmological simulation code GADGET-2". In: *Monthly notices of the royal astronomical society* 364.4 (2005), pp. 1105–1134.

[54] Volker Springel and Lars Hernquist. "The history of star formation in a Λ cold dark matter universe". In: *Monthly Notices of the Royal Astronomical Society* 339.2 (2003), pp. 312–334.

[55] James M Stone, Dimitri Mihalas, and Michael L Norman. "ZEUS-2D: A radiation magnetohydrodynamics code for astrophysical flows in two space dimensions. III-The radiation hydrodynamic algorithms and tests". In: *Astrophysical Journal Supplement Series (ISSN 0067-0049), vol. 80, no. 2, June 1992, p. 819-845. Research supported by University of Illinois.* 80 (1992), pp. 819–845.

[56] MU SubbaRao et al. "Visualization of large scale structure from the sloan digital sky survey". In: *New Journal of Physics* 10.12 (2008), p. 125015.

[57] Licia Verde, Tommaso Treu, and Adam G Riess. "Tensions between the early and late Universe". In: *Nature Astronomy* 3.10 (2019), pp. 891–895.

[58] Steven Weinberg. *Gravitation and Cosmology: Principles and Applications of the General Theory of Relativity*. New York: John Wiley and Sons, 1972. ISBN: 978-0-471-92567-5, 978-0-471-92567-5.

[59] Robert PC Wiersma, Joop Schaye, and Britton D Smith. "The effect of photoionization on the cooling rates of enriched, astrophysical plasmas". In: *Monthly Notices of the Royal Astronomical Society* 393.1 (2009), pp. 99–107.